Coherence and Phase Synchrony Analysis of Electroencephalogram

Gleb V. Tcheslavski

Dissertation submitted to the faculty of the Virginia Polytechnic Institute and State University in partial fulfillment of the requirements for the degree of

Doctor of Philosophy
In
Electrical Engineering

Dr. A. A. (Louis) Beex (Chairman)
Dr. Robert J. Adams
Dr. Christopher A. Beattie
Dr. Amy E. Bell
Dr. Ioannis M. Besieris
Dr. Gary S. Brown

December 12, 2005
Blacksburg, Virginia

Keywords: Coherence, Phase Synchrony, EEG, Statistical DSP, LS Modified Yule-Walker, Degraded Signal

Coherence and Phase Synchrony Analysis of Electroencephalogram

Gleb V. Tcheslavski

ABSTRACT

Phase Synchrony (PS) and coherence analyses of stochastic time series – tools to discover brain tissue pathways traveled by electrical signals – are considered for the specific purpose of processing of the electroencephalogram (EEG).

We propose the Phase Synchrony Processor (PSP), as a tool for implementing phase synchrony analysis, and examine its properties on the basis of known signals. Long observation times and wide filter bandwidths can decrease bias in PS estimates. The value of PS is affected by the difference in frequency of the sequences being analyzed and can be related to that frequency difference by the periodic sinc function.

PS analysis of the EEG shows that the average PS is higher – for a number of electrode pairs – for non-ADHD than for ADHD participants. The difference is more pronounced in the δ rhythm (0-3 Hz) and in the γ rhythm (30-50 Hz) PS. The Euclidean classifier with electrode masking yields 66 % correct classification on average for ADHD and non-ADHD subjects using the δ and γ_1 rhythms.

We observed that the average γ_1 rhythm PS is higher for the eyes closed condition than for the eyes open condition. The latter may potentially be used for vigilance monitoring. The Euclidean discriminator with electrode masking shows an average percentage of correct classification of 78 % between the eyes open and eyes closed subject conditions.

We develop a model for a pair of EEG electrodes and a model-based MS coherence estimator aimed at processing short (i.e. 20 samples) EEG frames. We verify that EEG sequences can be modeled as AR(3) processes degraded by additive white noise with an average SNR of approximately 11-12 dB.

Application of the MS coherence estimator to the EEG suggests that MS coherence is generally higher for non-ADHD individuals than for ADHD participants when evaluated for the θ rhythm of EEG. Also, MS coherence is consistently higher for ADHD subjects than for the majority of non-ADHD individuals when computed for the low end of the δ rhythm (i.e. below 1 Hz).

ADHD produces more measurable effects in the frontal lobe EEG and for participants performing attention intensive tasks.

Acknowledgements

I would like to thank and express my most sincere gratitude to Dr. A. A. (Louis) Beex for his guidance, advice, and support during this research. This work would have been impossible without his help and suggestions. Working in the DSP Research Lab under his guidance improved my technical skills and extended my understanding of DSP algorithms.

I would like to specially thank Dr. Helen J. Crawford from the Psychology Department for the time and patience she devoted to me during many consultations, for the support that I was always experiencing, for the EEG data she provided for this work, and for always being a brilliant and courageous person.

I also would like to specifically thank my former advisor Dr. Gary S. Brown and Dr. Robert J. Adams for all the help and support they granted me during my first year at Virginia Tech.

I would like to extend my gratitude to Dr. Christopher A. Beattie, Dr. Amy E. Bell, and Dr. Ioannis M. Besieris, who kindly agreed to serve as Members of my Graduate Committee.

I would like to thank all the people from the Department of Physics, whom I was working with - and Christa Thomas in particular - for their great attitude, financial support, and the invaluable opportunity to obtain extensive teaching experience during the last three and a half years.

I would like to thank Li Wan for the EEG data she shared with me, her consultations, and for being a good friend. Also, I would like to thank my lab mates Takeshi (Kesh) Ikuma and Andres Moctezuma for their help and support.

Finally, my special thanks to my family, my friends in Russia and in Blacksburg – Ksenia Tcheslavskaia, Vladimir Gantovnik, Julie Uan-Zo-li, Vladislava Ratishna, Alex Uan-Zo-li, Alex Onifriev, Alex Pronin, Ksenia Pronina, and many others – for all their help, support, and considerations.

Gleb V. Tcheslavski

Table of Contents

List of Figures

List of abbreviations

ACF	Auto-Correlation Function
ADA	Absolute Difference Average
ADD, ADD/ADHD	Attention Deficit (Hyperactivity) Disorder
ADDA	Attention Deficit Disorder Association
AR	Auto-Regressive
ARE	Average Relative Error
ARMA	Auto-Regressive Moving Average
BCI	Brain-Computer Interface
BwM	Bi-Weight Midcovariance
DFT	Discrete Fourier Transform
DSM-IV	Diagnostic and Statistical Manual of Mental Disorders, Fourth Edition
DSP	Digital Signal Processing
EEG	Electro-encephalogram
EOG	Electro-oculogram
ERP	Event Related Potentials
FIR	Finite Impulse Response
HiS	High Schizotypy
IPP	Instantaneous Phase Processor
LoS	Low Schizotypy
LPF	Low Pass Filter
LSMYWE	Least Squares Modified Yule-Walker Equation
MA	Moving Average
MAE	Mean Absolute Error
MDL	Minimum Description Length
MS	Magnitude Squared
PDF	Probability Density Function
POUS	Probability of Unstable Solution
PS	Phase Synchrony

PSD	Power Spectral Density
PSP	Phase Synchrony Processor
RM	Relative Magnitude
RV	Random Variable
SNR	Signal to Noise Ratio
SPQ	Schizotypal Personality Questionnaire

Chapter 1

Background and literature review

The electroencephalogram (EEG) is a weak (generally, less than 300 μV) electrical signal obtained from electrodes mounted on or under the surface of a human (or non-human) head.

1.1 History of the Electroencephalogram (EEG)

The discovery of the electroencephalogram phenomenon is traditionally associated with the name of Austrian psychiatrist Hans Berger, who performed the first EEG recording from a human brain in 1924 using metal strips pasted to the scalp. However - almost 50 years before Berger, in 1875 - Richard Caton, a Liverpool physician and medical school lecturer, published his observations of spontaneous electrical activity in the brain of laboratory animals [1]. In his study, Caton used a reflecting galvanometer invented in 1858 by Lord Kelvin, which - according to Bronzino [2] - does not provide sufficient amplification. Perhaps that was one of the reasons why the work of Caton received little attention and is questioned nowadays. Nevertheless, in 1876 Russian scientist Vasili Danilevsky had made similar experiments on dogs and published the results in his doctoral thesis one year later. Similar observations were reported by Fleischel von Marxow in 1883 and Adolph Beck from Poland in 1890. In 1913, Vladimir Pravdich-Neminsky published photographic recordings of dogs' brain waves using an invasive method [3].

In the early 1920s, Dr. Hans Berger had begun his study of brain electricity, which he later named the *Elektroenkephalogramm*. He had obtained the first records from the subject, who had a skull with a gap under the skin. Later, Dr. Berger's fifteen-year-old son Klaus became the subject of his study. Hans Berger was able to measure the irregular, relatively small electrical potentials (i.e., 50 to 100 μV) coming from the brain.

Berger had observed the cyclic nature of the EEG, discovered and studied Alfa (8-12 Hz) and Beta (18-30 Hz) waves recorded from normal and epileptic patients, laying the foundation for the application of this technique to clinical practice. Later, in his publication in 1929, Berger writes [4], [5], [6]: "The electroencephalogram represents a continuous curve with continuous oscillations in which ... one can distinguish larger first order waves with an average duration of 90 milliseconds and smaller second order waves of an average duration of 35 milliseconds. The larger deflections measure at most 150 to 200 microvolts..." A photograph of Hans Berger and the system for EEG recording, which he developed in 1926, are seen in Figure 1.1.

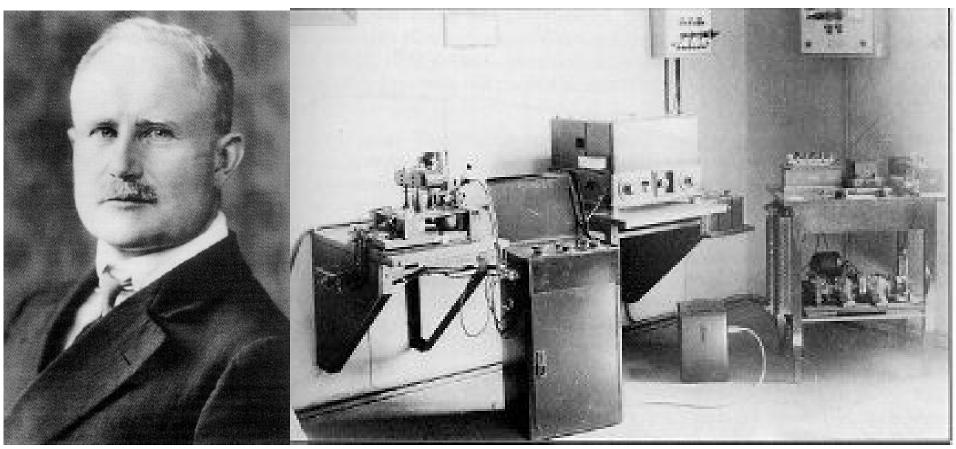

Figure 1.1: Hans Berger and his 1926 system for recording EEG.

Figure 1.2 depicts the first EEG record obtained by Hans Berger in 1928. Figures 1.1 and 1.2 have been downloaded from the Internet site: http://chem.ch.huji.ac.il/~eugeniik/history/berger.html.

Figure 1.2: The first EEG recorded by Hans Berger, 1928; the lower signal is a 10 Hz reference sinusoid.

Berger suggested that the activity of the brain changes in a consistent and recognizable fashion when the state of the subject changes, as in going from relaxation to alertness. He also concluded that brain waves could be greatly affected by certain pathologic conditions after noting a marked increase in the amplitude of brain waves recorded during convulsive seizures.

Surprisingly, the Berger studies did not attract interest until 1934, when Adrian and Matthews published their papers [7], [8] verifying the findings of Hans Berger. One of the major contributions of Adrian and Matthews was their classification of certain rhythms e.g., regular oscillations in the EEG.

In 1949 Moruzzi and Magoun [9] demonstrated the existence of pathways widely distributed through the central reticular core of the brainstem that were capable of exerting a diffuse activating influence on the cerebral cortex. This study established the physiological basis for the previously discovered rhythms. More on the history of EEG can be found elsewhere [10]. Nowadays more advanced methods of weak electrical activity registration and signal processing are available and the EEG has become a powerful tool in psychological and physiological research of the human brain.

1.2 Instruments and standards for EEG studies; some interesting applications of the EEG

While more sensitive tools for registering electrical signals were becoming available, EEG research moved from invasive to non-invasive methods for obtaining records. Nowadays, non-invasive methods dominate as EEG signals are generally acquired with a system of skin-mounted electrodes. The International Federation of Electroencephalography and Clinical Neurophysiology has adopted the 10–20 electrode placement system shown in Figure 1.3. In addition to the standard 10–20 scalp array, electrodes to monitor eye movement, ECG, and muscle activity are essential for discrimination of different vigilance or behavioral states. Additional electrode placement systems involving more electrodes are also available.

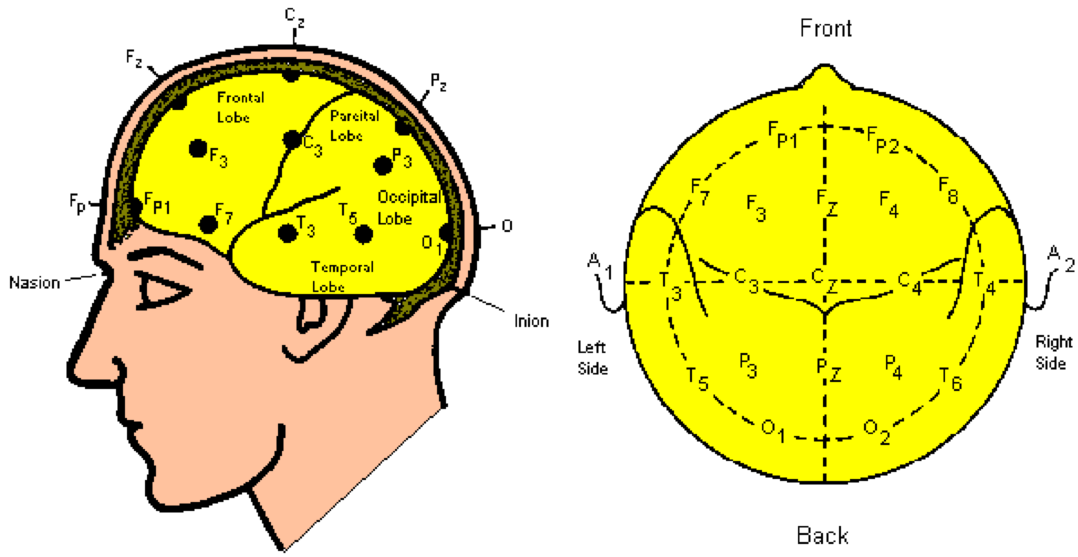

Figure 1.3: Standardized electrode placement using the "10-20 International system."

Any EEG system consists of electrodes, amplifiers (with or without appropriate filters), and a recording device. Commonly used scalp electrodes consist of Ag-AgCl disks, 1 to 3 mm in diameter, with long flexible leads that can be plugged into an amplifier [2]. Conductive electrode paste helps obtain low impedance and keep the electrodes in place. EEG signals of amplitude up to 10 μV can be obtained from the electrodes and require amplification to gain a sufficient level for a recording device. Many different recording instruments are available. A pen or chart recorder (usually multi-channel) is one of the most commonly used; the other type of registering device is an analog tape recorder. At the present time, EEG recording is often performed by computer based signal acquisition, digitization, and storage systems.

Many commercial systems for registering EEG signals are available. Among them are Comet® Portable EEG, Aurora® and Aurora® Deluxe manufactured by Grass Telefactor; SynAmps®, ESI®, and MagLink® by Neuroscan. Numerous software products for EEG processing, such as STIM and ToolBox 2003 by Neuroscan or TWin® Clinical Software by Grass Telefactor, can be found on the market as well.

Figure 1.4 illustrates an EEG signal recorded from the F_{p1} electrode by the Neuroscan-24 system (NRS-24) sampled at 256 Hz.

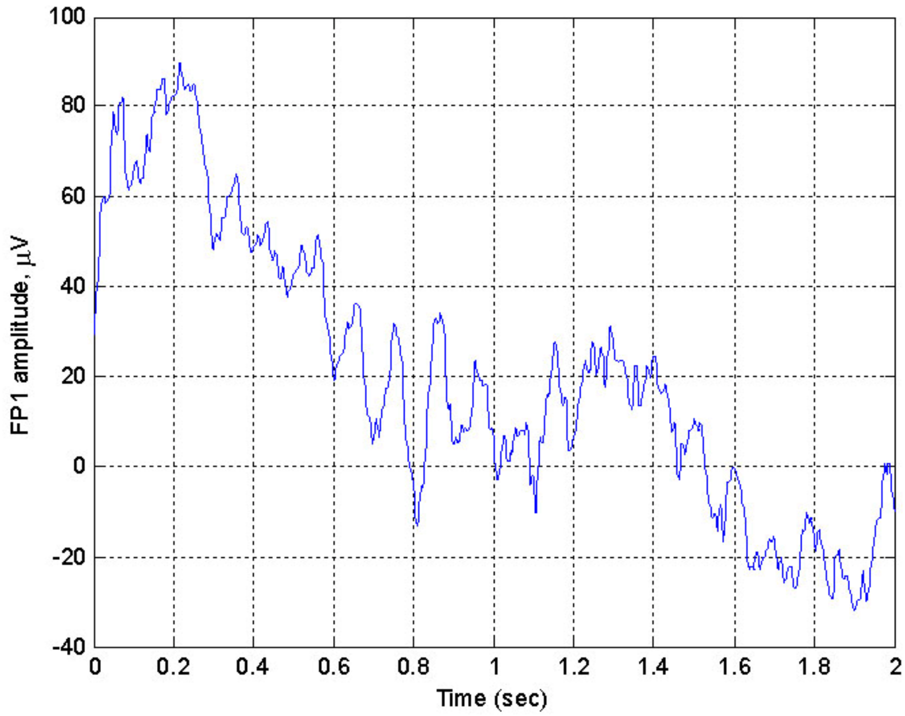

Figure 1.4: Amplitude of EEG signal acquired from F_{p1} electrode; f_s = 256 Hz.

It is also worth noting that the most employed algorithm for processing of EEG signals, the Fourier transform and its modifications, has been used since 1932 when Fourier analysis was applied to the EEG record by Dietch [11].

The focus of the present study is the processing of EEG records for psychological needs. However, the electroencephalogram and its processing find multiple applications, not only in medicine and psychological research. A new growing area based on real-time analysis of the EEG is brain-computer interface (BCI) research and its applications. The primary goal of BCI is to give its users channels of communication and control that are not associated with any normal output channels of the human brain but utilize the electrical activity of the brain as a carrier. This topic mostly arises from the needs of people with severe motor disabilities. All existing BCI can be subdivided into communication and control systems. The common communication rate of successful systems is less than 10 letters per minute [12]. McKay and Provost report BCI-based remote control of a toy car with an achieved accuracy of up to 40% [13]. The authors utilized modulations of the α rhythm measured from the visual cortex. Examples of BCI exploring the possibility of controlling a wheelchair or prostheses can be found in the literature [14]. Interested readers are pointed to the work of Wolpaw and colleagues [14], who are among the pioneers in BCI research.

1.3 Attention Deficit (Hyperactivity) Disorder (ADD/ADHD) and its treatment

Attention is the information management process in which intensiveness, sustainability, selectiveness, and controllability combine and interact. One of the most common attention disorders is ADD/ADHD. According to epidemiological data http://www.emedicine.com/med/topic3103.htm, approximately 3 to 7 % of the U.S. population has ADHD.

According to information available on the web site of the Attention Deficit Disorder Association (ADDA) http://www.add.org/: ADHD is a diagnosis applied to children and adults who consistently display certain characteristic behaviors over a period of time. The most common core features include:

- distractibility (poor sustained attention to tasks)
- impulsivity (impaired impulse control and delay of gratification)
- hyperactivity (excessive activity and physical restlessness)

In order to meet diagnostic criteria, these behaviors must be excessive, long-term, and pervasive.

According to the DSM-IV (the Diagnostic and Statistical Manual of Mental Disorders, Fourth Edition) "some common symptoms of ADHD include: often fails to give close attention to details or makes careless mistakes; often has difficulty sustaining attention to tasks; often does not seem to listen when spoken to directly; often fails to follow instructions carefully and completely; losing or forgetting important things; feeling restless, often fidgeting with hands or feet, or squirming; running or climbing excessively; often talks excessively; often blurts out answers before hearing the whole question; often has difficulty awaiting turn."

From the popular Concerta® brochure:

ADHD is a condition that:

- is biological
- has its origin in brain function
- has a genetic component
- is real and diagnosable on solid criteria
- may continue into adulthood
- is treatable but not curable at this time
- may be accompanied by associated conditions

ADHD is NOT caused by:

- bad parenting
- too much TV
- food allergies
- excess sugar
- a head injury
- bad schooling

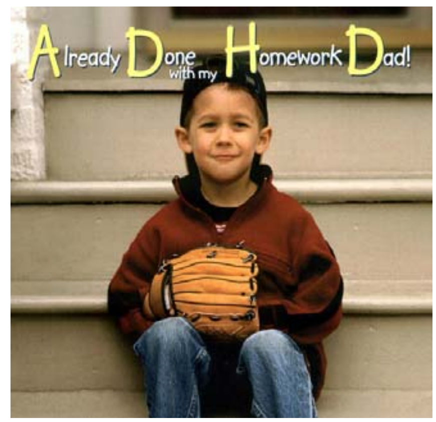

ADHD was formerly associated with childhood only and its symptoms were thought to disappear completely with puberty. This point of view has been debated and completely disproved in the 80's [15], [16], [17]. Approximately 70 % of kids diagnosed with ADHD show all symptoms of this disorder in adulthood [16]. It has also been shown that, undiagnosed in childhood, ADHD may be successfully treated in adulthood [17].

Treatment of ADHD traditionally follows one of two approaches, namely, the medical and psychological models. The medical treatment is mainly based on methylphenidate (Ritalin®) taken internally. This approach is effective on motor functions but does almost not affect symptoms related to attention deficits. The other model primarily employs behavior modification as a source of self-control for the patient. However, both approaches show limited effects on information processing, impulsivity, destructibility, and emotional liability [18], [19]. In past decades, progress in personal computers has made possible the development of computer-based cognitive training systems usually associated with the term *"Biofeedback."* The growing body of evidence reported in the literature proves that significant improvement in information processing can be achieved, and other aspects practically unaffected by medication treatment in

ADHD patients can be treated by, using biofeedback training systems. Linden, Habib, and Radojevic reported encouraging results of the application of a biofeedback learning system to a group of eighteen children [21]; Kotwal, Burns, and Montgomery described positive results of the application of two different biofeedback protocols to a single subject [18]; Tensey and Bruner have achieved impressive results applying biofeedback training to a ten-year old ADHD patient [19], [20]; Barabasz and Barabasz proposed the usage of hypnosis during biofeedback training to achieve quicker results of treatment [22]. Moreover, based on his study results, Arbarbanel suggested that neurofeedback results are more permanent than the results of medical therapy [23]. Linden reported results of the successive application of a biofeedback system based on the processing of event related potentials (ERP) [24].

The series of experiments considering biofeedback have been based on the findings, that originated from the experiments of Lubar and colleagues [25], [26], that patients diagnosed with ADHD produce excessive activity in θ and show deficit in the β range as compared to non-ADHD subjects. The same results were confirmed later by Janzen et al. [27] and Barabasz, Crawford, and Barabasz pointed out that this effect is more pronounced when the patient performs more difficult cognitive tasks [28]. Moreover, Matsuura and colleagues have observed the same effect in EEG of patients in Japan, Korea, and China [29].

Another interesting observation is the more desynchronized θ wave noticed in ADHD patients compared to non-ADHD subjects, according to Barabasz, Crawford, and Barabasz [28], especially in the EEG acquired from the frontal lobe. These results are in agreement with a growing body of evidence of frontal lobe dysfunction in ADD/ADHD patients [30], [31], [32]. More recently, research has also focused on the role of pathways between brain structures as a possible model for the neurological basis of ADD/ADHD [31].

1.4 Concepts of coherence and phase synchrony

The coherence function is a frequency domain based measure of the linear association between two wide sense stationary time series. According to the definition of the coherence function, it is the normalized cross-spectrum [33], [34], as follows

$$\Gamma_{xy}(e^{j\omega}) = \frac{S_{XY}(e^{j\omega})}{\sqrt{S_{XX}(e^{j\omega}) \cdot S_{YY}(e^{j\omega})}} \tag{1.1}$$

where $S_{XY}(e^{j\omega})$, $S_{XX}(e^{j\omega})$, and $S_{YY}(e^{j\omega})$ are cross- and auto-spectra respectively.

It is seen that this function is complex and can be denoted as follows:

$$\Gamma_{xy}(e^{j\omega}) = \left|\Gamma_{xy}(e^{j\omega})\right| e^{j\lambda(e^{j\omega})} \tag{1.2}$$

where $\left|\Gamma_{xy}(e^{j\omega})\right|$ is referred to as the magnitude (squared) coherence and $\lambda(e^{j\omega})$ is called the phase coherence.

The magnitude squared (MS) coherence function "measures the degree to which one process can be represented as the output of a linear filter operating on the other process" [34] and varies from 0 - for two statistically independent processes - to 1, when one process is the result of linear filtering performed on the other. The phase coherence is usually interpreted as a phase lead of one signal over the other.

Another useful measure of linear dependence between two stochastic signals, phase synchrony analysis, has been independently proposed by Lachaux et al. [35] and Mormann et al. [36] and applied later by Allefeld and Kurths [37], [38]. This approach is based on the concept of phase synchronization of chaotic oscillators studied by Rosenblum et al. [39]. This method was developed to detect stability of phase across different trials but can be successively applied to a single trial within a time window [40]. The phase synchrony (coefficient), also called the phase locking value, r_{lm}, of two oscillators l and m, over an N_w sample long time window, is specified as follows [35], [36], [37], and [38]:

$$r_{lm,n} = \left| \frac{1}{N_w} \sum_{k=n-N_w+1}^{n} e^{-j(\varphi_{lk} - \varphi_{mk})} \right| \tag{1.3}$$

where φ_{lk} and φ_{mk} denote instantaneous phase sequences for oscillators l and m respectively and n represents the time instant at which the analysis ends. To obtain the sequence of instantaneous phases, Lachaux convolved the signal with the Gabor wavelet function, Allefeld used the Morlet wavelet, and Mormann applied an analytic signal generator via the Hilbert transform. It is important from our point of view to note that a wavelet function can be viewed as a band-pass filter. Hence, the phase sequences generated via wavelets are frequency specific, i.e. observed over a narrow frequency range. However, a Hilbert transformer-based analytic signal generator is not generally intended to extract frequency specific content. Thus, to study phase synchrony in the frequency band of interest, band-pass filtering is needed. Mormann does not implement such filtering [36].

The phase synchrony (coefficient) takes on values between 0, for two signals at different frequencies, and 1, for signals that exhibit a constant difference in instantaneous phase (representing the situation where a signal and its time-shifted version are observed). This measure requires prefiltering at a frequency of interest. The interesting properties of the phase synchrony coefficient are its independence of the signal amplitudes and that no assumptions about the nature of the signals are made.

Both coherence and phase synchrony have found intensive usage in the study of brain signals, particularly the EEG. Studies report enormously high synchronization in EEG signals during epileptic seizures [41], Spencer and colleagues have confirmed the hypothesis that gamma band synchronization is abnormal in schizophrenia [42], Tallon-Baudry et al. were studying β-range synchrony between extra-striate areas of the brain during maintaining visual short-term memory [43].

In conclusion, it is also necessary to emphasize that although phase coherence and phase synchrony are quite similar and often are mixed up, they are two principally different measures. Phase coherence can be interpreted as phase shifts and amplitude changes over frequency between two correlated sequences, while phase synchrony indicates whether the phase shift is close to a constant over the specified time interval. This interpretation justifies narrow-band filtering in the case of phase synchrony. The concept of a phase shift (either lead or lag) between two signals is only applicable when both signals are at the same frequency. Coherence and phase synchrony will be examined and discussed in detail in the following chapters.

1.5 Limitations of the classical coherence function and possible solutions to overcome these limitations

The classical methods of spectral estimation are based on the Fourier transform and rely entirely on the following two definitions of power spectral density (PSD) [44]:

$$P(\omega) = \sum_{n=-\infty}^{\infty} r_n \cdot e^{-j\omega n} \tag{1.4}$$

$$P(\omega) = \lim_{N \to \infty} E\left\{ \frac{1}{N} \left| \sum_{n=1}^{N} x_n \cdot e^{-j\omega n} \right|^2 \right\} \tag{1.5}$$

where r_n denotes the auto- or cross-correlation for lag n, N is the length of the analyzed record x_n, and $E\{\}$ represents expectation.

The problem of estimating the PSD from a finitely (length N) observed sequence x_n is ill-posed from a statistical standpoint, unless appropriate assumptions about the PSD are made [44]. Strictly speaking, without making any assumptions, PSD estimation requires an infinite number of independent values of $P(\omega)$ to be obtained based on a finite number of signal observations. This problem can be mitigated either by parameterization of $P(\omega)$ via a model of finite dimensions, or by smoothing $P(\omega)$ based on the assumption that the PSD is nearly constant over a narrow frequency band [44]. Dobie et al. proposed an algorithm to smooth the coherence estimates [50]. According to the authors, such smoothing can increase reliability of the estimate.

The other important limitation is that the concepts of spectra, PSD, correlation sequences, and coherence function are only applicable to stationary or, at least, wide sense stationary processes [44], [45], and [46]. EEG signals are known to exhibit a highly non-stationary and often non-linear nature [46], [47], and [48] and can be interpreted as a collection of non-stationary stochastic processes [49]. A stochastic process is called locally stationary if it behaves like a stationary process over short intervals of time [49].

According to the review presented by Schack and Krause [46], fragments of EEG of length up to 40 – 290 ms can be treated as stationary. Another source [47] suggests that the maximum length of locally stationary EEG segments does not exceed 80 ms. Assuming the duration of the stationary fragments to be 100 ms and the sampling frequency to be 256 Hz, the maximum length of a signal record to be analyzed is 25 samples.

The classical spectral estimators are not capable of providing reliable estimates for such short sequences. As a consequence, parametric methods of spectral analysis must be employed.

One possible approach to solving this problem is to parameterize measurements of synchronization between two oscillators. Cadzow and Solomon have developed an algorithm to estimate a rational MS coherence function based on the autoregressive moving average (ARMA) linear model [51]. Franaszczuk and Bergey proposed a method to estimate synchronization of multivariable EEG records [41]. The essence of the method is to establish a p^{th} order m–channel autoregressive (AR) model for the m–channel EEG signal and use the residuals of the model as a measure of synchronization. The smaller the residuals, the better the model fits the data, and the lower the entropy of the system. Low entropy means a high level of synchrony in the data. Florian and Pfurtscheller suggest dividing EEG records into locally stationary fragments to establish an autoregressive (AR) model for each fragment [49]. Moreover, considering the EEG records of event-related potentials as a set of realizations of the same stochastic process, the authors propose to average over the estimated AR parameters. Schack and Krause have fitted an iterative bi-variate ARMA model to EEG records and estimated the coherence function parametrically [46]. This work was extended to the multivariate case by Ding et al. [48].

1.6 References

[1] R. Caton, “The electric currents of the brain,” *British Medical Journal*, vol. 2, 1875, p. 278.

[2] J. D. Bronzino, *Principles of Electroencephalography. The Biomedical Engineering Handbook*, 2nd Edition, Ed. J. D. Bronzino Boca Raton: CRC Press LLC, 2000.

[3] W. Neminski, “Ein Versuch der Registrierung der elektrischen Gehirnerscheinungen,” *Zentralblatt für Physiologie*, vol. 27, 1913, pp. 951-960.

[4] H. Berger, “Ueber das Elektroenkephalogramm des Menschen,“ *Archiv für Psychiatrie und Nervenkrankheiten*, vol. 87, 1929, Berlin, pp. 527-570.

[5] H. Berger, *On the electroencephalogram of man. The fourteen original reports on the human electroencephalogram.* Translated from the original German and edited by Pierre Gloor. Amsterdam, Elsevier, 1969.

[6] “EEG - ElectroEncephaloGraph,” *Biocybernaut Institute*, [Online publication], 2000, [cited 25 July 2003].

[7] E. Adrian and B. Matthews, “The interpretation of potential waves in the cortex,” *Journal of Physiology*, Cambridge, vol. 81, 1934, pp. 440-471.

[8] E. Adrian and B. Mathews, “The Berger Rhythm: Potential changes from occipital lobes in man,” *Brain*, Oxford, vol. 57, 1934, pp. 355-385.

[9] G. Moruzzi and H. Magoun, “Brain stem reticular formation and activation of the EEG,” *Electroencephalographically Clinical Neurophysiology*, 1949, #1 pp. 455-473.

[10] M. Brazier, *The electrical activity of the nervous system. A textbook for students*, Second edition. New York, the Macmillan Company, 1960.

[11] K. J. Blinowska and P. J. Durka, “Unbiased high resolution method of EEG analysis in time-frequency,” *Acta Neurobiology*, vol. 61, 2001, pp. 157-174.

[12] E. Donchin, K. M. Spencer, and R. Wijesinghe, “The mental prosthesis: assessing the speed of a P300-based brain-computer interface,” *IEEE Transactions on rehabilitation engineering*, vol. 8, # 2, June 2000, pp. 174-179.

[13] J. L. McKay and S. Provost, "A real-time EEG Based Remote Control of a Radio–Shack Car," *LEMS Technical Report*, 2002.

[14] J. R. Wolpaw, N. Birbaumer, W. J. Heetderks, D. J. McFarland, P. H. Peckham, G. Schalk, E. Donchin, L. A. Quatrano, C. J. Robinson, and T. M. Vaughan, "Brain-computer interface technology: a review of the first international meeting," *IEEE transactions on rehabilitation engineering*, vol. 8, #2, June 2000, pp. 164-173.

[15] S. H. Klee, B. D. Garfunkel, and H. Beauchesne, "Attention deficit in adults," *Psychiatric annals*, vol. 16, #1, January 1986, pp. 52-56.

[16] L. Hechtman, "Attention-deficit hyperactivity disorder in adolescence and adulthood: an updated follow-up," *Psychiatric annals*, vol. 19, #11, November 1989, pp. 597-603.

[17] J. A. Bourgeois, "Three cases of adult attention-deficit hyperactivity disorder," *Military medicine*, vol. 160, #9, 1995, pp. 473-476.

[18] D. B. Kotwal, W. J. Burns, and D. D. Montgomery, "Computer-assisted cognitive training for ADHD. A case study," *Behavior modification*, vol. 20, #1, January 1996, pp. 85-96.

[19] M. A. Tansey and R. L. Bruner, "EMG and EEG biofeedback training in the treatment of a 10-year old hyperactive boy with a developmental reading disorder," *Biofeedback and self-regulation*, vol. 8, #1, 1983, pp. 25-37.

[20] M. A. Tansey, "Ten-year stability of EEG biofeedback results for a hyperactive boy who failed fourth grade perceptually impaired class," *Biofeedback and self-regulation*, vol. 18, #1, 1993, pp. 33-44.

[21] M. Linden, T. Habib, and V. Radojevic, "A controlled study of the effects of EEG biofeedback on cognition and behavior of children with attention deficit disorder and learning disabilities," *Biofeedback and self-regulation*, vol. 21, #1, 1996, pp. 35-49.

[22] A. Barabasz and M. Barabasz, *Neurotherapy and alert hypnosis in the treatment of attention deficit hyperactivity disorder. Casebook of clinical hypnosis*. American Psychological Association, 1996.

[23] A. Abarbanel, “Gates, states, rhythms, and resonances: the scientific basis of neurofeedback training,” *Journal of Neurotherapy*, fall 1995, pp. 15-38.

[24] M. Linden, “Event related potentials of subgroups of attention deficit disorder children and implications for EEG biofeedback,” *California Biofeedback,* vol. 7, #1, 1991, pp. 7-12.

[25] J. F. Lubar, “Discourse on the development of EEG diagnostics and biofeedback for attention-deficit/hyperactivity disorders,” *Biofeedback and self-regulation*, vol. 12, #3, 1991, pp. 201-225.

[26] J. F. Lubar, M. O. Swartwood, J. N. Swartwood, and P. H. O’Donnell, “Evaluation of the effectiveness of EEG neurofeedback training for ADHD in a clinical setting as measured by changes in T.O.V.A. scores, behavioral rating, and WISC-R performance,” *Biofeedback and self-regulation*, vol. 20, #1, 1995, pp. 83-99.

[27] T. Janzen, K. Graap, S. Stephanson, W. Marshall, and G. Fitzsimmons, “Differences in baseline EEG measures for ADD and normally achieving preadolescent males,” *Biofeedback and self-regulation*, vol. 20, #1, 1995, pp. 65-82.

[28] A. Barabasz, H. Crawford, and M. Barabasz, “EEG topographic map differences in attention deficit disordered and normal children: Moderating effects from focused active alert instructions during reading, math and listening tasks,” *Presented at the 33rd Annual Meeting of the Society for Psychophysiological Research*, Rottach-Egem, Germany, October, 27-31, 1993.

[29] M. Matsuura, Y. Okubo, M. Toru, T. Kojima, Y. He, Y. Hou, Y. Shen, and C.K. Lee, “A cross-national EEG study of children with emotional and behavioral problems: a WHO collaborative study in the western pacific region,” *Biological Psychiatry*, vol. 34, 1993, pp. 59-65.

[30] R. A. Barkley, G. Grodzinsky, and G. J. DuPaul, “Frontal lobe functions in attention deficit disorder with and without hyperactivity: a review and research report,” *Journal of abnormal child psychology*, vol. 20, #2, 1992, pp. 163-188.

[31] C. A. Riccio, G. W. Hynd, M. J. Cohen, and J. J. Gonzalez, "Neurological basis of attention deficit hyperactivity disorder," *Exceptional children*, vol. 60, #2, 1993, pp. 118-124.

[32] J. N. Giedd, F. Xavier Castellanos, B. J. Cassey, P. Kozuch, A. C. King, S. D. Hamburger, and J. L. Rapoport, "Quantitative morphology of the corpus callosum in attention deficit hyperactivity disorder," *American Journal of Psychiatry*, vol. 151, #5, 1994, pp. 665-669.

[33] W. A. Gardner, *Introduction to random processes: with applications to signals and systems.* Second edition, McGraw-hill Publishing Company, 1989.

[34] L. H. Koopmans, "The spectral analysis of time series," vol. 22 in *Probability and mathematical statistics.* Academic Press, 1995.

[35] J.-P. Lachaux, E. Rodrigues, J. Martinerie, and F. J. Varela, "Measuring phase synchrony in brain signals," *Human Brain Mapping* #8, 1999, pp. 194-208.

[36] F. Mormann, K. Lehnertz, P. David, C. E. Elger, "Mean phase coherence as a measure for phase synchronization and its application to the EEG of epilepsy patients," *Physica D*, #144, 2000, pp. 358-369.

[37] C. Allefeld and J. Kurths, "Multivariate phase synchronization analysis of EEG data," *IEICE Transactions Fundamentals*, vol. E86-A, #9 September, 2003, pp. 2218-2221.

[38] C. Allefeld and J. Kurths, "An approach to multivariate phase synchronization analysis and its application to event-related potentials," *International Journal of Bifurcation and Chaos*, vol. 14, #2, 2004, pp. 417-426.

[39] M. G. Rosenblum, A. S. Pikovsky, and J. Kurths, "Phase synchronization of chaotic oscillators," *Physical Review Letters*, vol. 76, #11, March 1996, pp. 1804-1807.

[40] M. L. Van Quyen, J. Foucher, J.-P. Lachaux, E. Rodriguez, A. Lutz, J. Martinerie, and F. Varela, "Comparison of Hilbert transform and wavelet methods for the analysis of neuronal synchrony," *Journal of Neuroscience Methods*, vol. 111, 2001, pp. 83-98.

[41] P. J. Franaszczuk and G. K. Bergey, "An autoregressive method for the measurement of synchronization of interictal and ictal EEG signals," *Biological Cybernetics*, vol. 81, 1999, pp. 3-9.

[42] K. M. Spencer, P. G. Nestor, M. A. Niznikiewicz, D. F. Salisbury, M. E. Shenton, and R. W. McCarley, "Abnormal neural synchrony in schizophrenia," *The Journal of Neuroscience*, vol. 23 (19), August 13, 2003, pp. 7404-7411.

[43] C. Tallon-Baudry, O. Bertrand, and C. Fischer, "Oscillatory synchrony between human extrastriate areas during visual short-term memory maintenance," *The Journal of Neuroscience*, vol. 21 (20), RC177, 2001, pp. 1-5.

[44] P. Stoica and R. Moses, *Introduction to spectral analysis.* Prentice-Hall, 1997.

[45] G. M. Jenkins and D. G. Watts, *Spectral analysis and its applications.* Holden-Day, 1968.

[46] B. Schack and W. Krause, "Dynamic power and coherence analysis of ultra short-term cognitive processes – a methodical study," *Brain topography*, vol. 8, #2, 1995, pp. 127-136.

[47] P. B. Colditz, C. J. Burke, and P. Celka, "Digital processing of EEG signals," *IEEE Engineering in Medicine and Biology*, September/October 2001, pp. 21-22.

[48] M. Ding, S. L. Bressler, W. Yang, H. Liang, "Short-window spectral analysis of cortical event-related potentials by adaptive multivariate autoregressive modeling: data preprocessing, model validation, and variability assessment," *Biological Cybernetics*, vol. 83, 2000, pp. 35-45.

[49] G. Florian and G. Pfurtscheller, "Dynamic spectral analysis of event-related EEG data," *Electroencephalography and clinical neurology*, vol. 95, 1995, pp. 393-396.

[50] R. A. Dobie and M. J. Wilson, "Optimal smoothing of coherence estimates," *Electroencephalography and clinical neurophysiology*, vol. 30, 1991, pp. 194-200.

[51] J. A. Cadzow and O. M. Solomon, Jr., "Linear modeling and the coherence function," *IEEE Transactions on Acoustics, Speech, and Signal Processing*, vol. ASSP-35, #1, January 1987, pp. 19-28.

Chapter 2

The Coherence function and its existing estimators

As mentioned in Section 1.4, the coherence function is a measure based upon the auto- and cross-spectral properties of the processes being analyzed. As defined in (1.4), the (mean square) coherence is

$$\Gamma_{xy}(e^{j\omega}) = \frac{S_{XY}(e^{j\omega})}{\sqrt{S_{XX}(e^{j\omega}) \cdot S_{YY}(e^{j\omega})}} \tag{2.1}$$

where $S_{XY}(e^{j\omega})$, $S_{XX}(e^{j\omega})$, and $S_{YY}(e^{j\omega})$ are cross- and auto-spectra respectively.

Since the cross-spectrum $S_{XY}(e^{j\omega})$ is generally complex, the coherence is a complex function and can be viewed as follows:

$$\Gamma_{xy}(e^{j\omega}) = \left|\Gamma_{xy}(e^{j\omega})\right| e^{j\lambda(e^{j\omega})} \tag{2.2}$$

where $\left|\Gamma_{xy}(e^{j\omega})\right|$ is the magnitude coherence and $\lambda(e^{j\omega})$ is the phase coherence.

2.1 Nonparametric estimates of the coherence function

Perhaps, the most employed algorithm to estimate the auto- and cross-spectra is Welch's averaged periodogram method, as implemented in the function "*cohere*" in Matlab. The popularity of this procedure can be explained by its relatively high computational efficiency. The N – sample long time series x_n and y_n being analyzed are divided to form K successive L – sample long frames each. These frames overlap with offset D (i.e., the overlap is L-D samples). The data window w_l is applied to each frame producing a set of modified periodograms that are then averaged.

The spectral estimates are defined as follows [1]:

$$\hat{S}_{XX}(e^{j\omega}) = \frac{1}{KLU} \sum_{i=0}^{K-1} \left| \sum_{l=0}^{L-1} w_l \cdot x_{l+iD} \cdot e^{-jl\omega} \right|^2 \tag{2.3}$$

$$\hat{S}_{YY}(e^{j\omega}) = \frac{1}{KLU}\sum_{i=0}^{K-1}\left|\sum_{l=0}^{L-1} w_l \cdot y_{l+iD} \cdot e^{-jl\omega}\right|^2 \tag{2.4}$$

$$\hat{S}_{XY}(e^{j\omega}) = \frac{1}{KLU}\sum_{i=0}^{K-1}\left(\left[\sum_{l=0}^{L-1} w_l \cdot x_{l+iD} \cdot e^{-jl\omega}\right]\cdot\left[\sum_{l=0}^{L-1} w_l \cdot y_{l+iD} \cdot e^{-jl\omega}\right]^*\right) \tag{2.5}$$

Where superscript * denotes complex conjugate, and $U = \frac{1}{L}\sum_{l=0}^{L-1} w_l$.

An estimate of the coherence function is formed based on the spectral estimates according to (2.1).

The importance of averaging while estimating coherence can be illustrated by the following consideration [2]. If no averaging over different time windows is performed, the squared coherence function is

$$\left|\Gamma_{xy}(e^{j\omega})\right|^2 = \frac{\left|X \cdot Y^*\right|^2}{\left(X \cdot X^*\right)\left(Y \cdot Y^*\right)} = \frac{\left(X \cdot X^*\right)\left(Y \cdot Y^*\right)}{\left(X \cdot X^*\right)\left(Y \cdot Y^*\right)} \equiv 1 \text{ for all frequencies,}$$

where X and Y represent the Fourier transforms of x_n and y_n respectively.

Some properties of the periodogram-based coherence estimate, as evaluated by Monte Carlo methods, are illustrated below.

The coherence was estimated for two normally distributed random sequences of length 1000 (generated by the Matlab command *randn*) as shown in Figure 2.1. The 4096-point DFT was used in the periodograms. The length of the analysis frames was varied from 100 to 1000 samples. The analysis frames were overlapping by 50%.

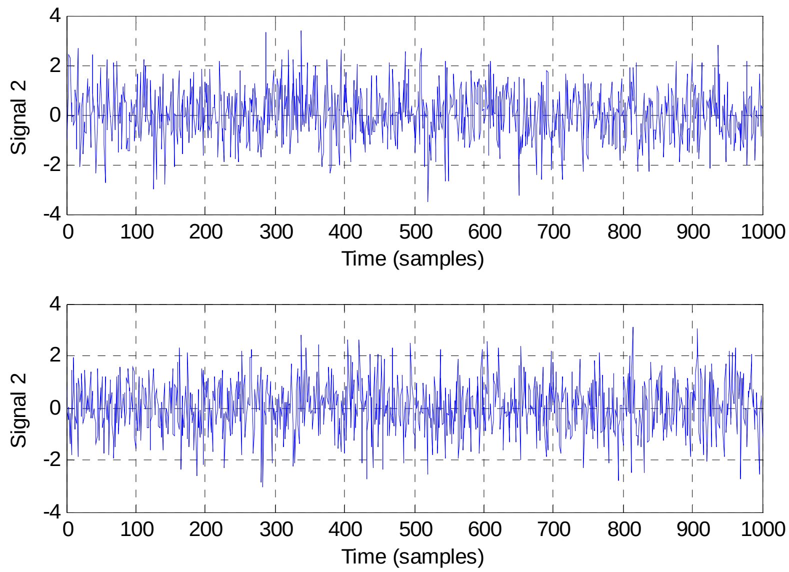

Figure 2.1: An example of analyzed sequences.

Because of the stochastic nature of the analyzed signals, coherence estimates for each length of analysis frame were averaged over 100 trials performed for the statistically independent data sets. Finally, these averaged over 100 trials estimates were also averaged over the entire frequency range. The result is presented in Figure 2.2.

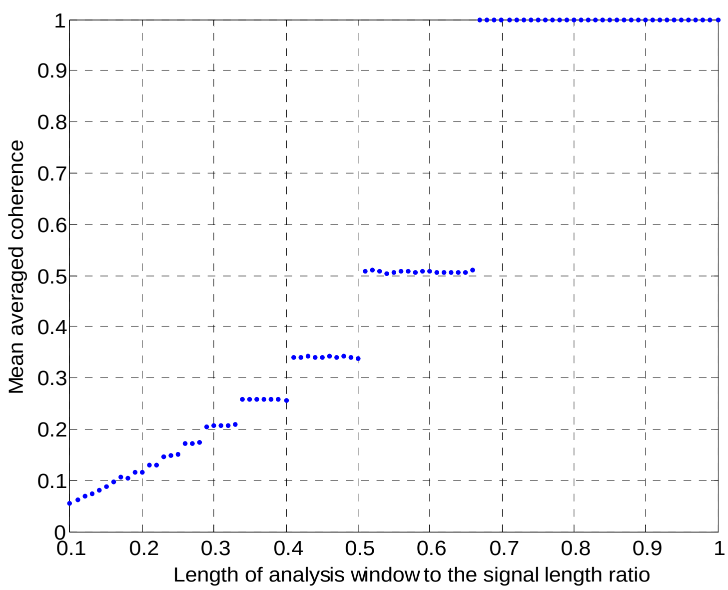

Figure 2.2: Mean average coherence estimates for different ratios of the length of the analysis frame to the signal record length; signal record length is 1000 samples, 50 % overlap for frames.

According to the definition, the coherence between two statistically independent sequences must be zero. Based on this property, we conclude, observing Figure 2.2, that low results (i.e. coherence less than 0.1, for instance) can be expected when the length of the analysis frame is less than 0.2 of the length of the signal record. On the other hand, the analysis frame must be long enough because the Welch's averaged periodogram method tends to generate biased spectral estimates when processing short frames that are not from white noise. These considerations suggest that the Welch-based coherence estimator is not desirable for processing of short records and frames.

Another nonparametric approach to estimating the coherence function has been proposed by Thomson [3]. This method is based on Thomson's spectral estimation procedure, also referred to as the multiple – taper method [4], [5], and [6], which is known to produce less biased spectral estimates in comparison with the periodogram method. This method was proposed for signals with complicated spectral densities. The appropriate procedure is briefly described next.

Assuming two N – sample long time records x_n and y_n, both with zero mean, the raw eigen-coefficients [5], [6] are specified as a discrete Fourier transform of the input signals

$$\tilde{x}_k(e^{j\omega}) = \sum_{n=0}^{N-1} x_n \cdot v_n^{(k)}(N,W) \cdot e^{-j\omega n} \tag{2.6}$$

where $v_n^{(k)}(N,W)$ is the discrete prolate spheroidal sequence, which is a Fourier transform of the discrete prolate spheroidal wave function $U_k(N,W;f)$ also called the Slepian function [7], [8], and [9]. These sequences are orthonormal providing spectral windows with well-concentrated energy, over which the data is observed. More on properties of Slepian functions can be found elsewhere [4], [5], [6], [7], [8], and [9]. W denotes the bandwidth: $0 < W < 0.5$.

The raw eigen-coefficients usually are weighted by $\sqrt{\lambda_k(N,W)}$ to form estimates of idealized eigen-coefficients

$$\hat{x}_k(e^{j\omega}) = \sqrt{\lambda_k(N,W)} \cdot \tilde{x}_k(e^{j\omega}) \tag{2.7}$$

Here $\lambda_k(N,W)$ are the eigenvalues of the N x N matrix $\rho(N,W)_{mn} = \dfrac{\sin 2\pi W(m-n)}{\pi(m-n)}$;

$m, n = 0,1,\ldots N-1$.

Similarly, the idealized eigen-coefficients are estimated for the record y_n. Finally, the estimates of auto- and cross-spectra are obtained as follows [1], [3]:

$$\hat{S}_{XX}(e^{j\omega}) = \frac{1}{2NW} \sum_{k=0}^{2NW-1} \left| \hat{x}_k(e^{j\omega}) \right|^2 \tag{2.8}$$

$$\hat{S}_{YY}(e^{j\omega}) = \frac{1}{2NW} \sum_{k=0}^{2NW-1} \left| \hat{y}_k(e^{j\omega}) \right|^2 \tag{2.9}$$

$$\hat{S}_{XY}(e^{j\omega}) = \frac{1}{2NW} \sum_{k=0}^{2NW-1} \hat{x}_k(e^{j\omega}) \cdot \hat{y}_k^{\,*}(e^{j\omega}) \tag{2.10}$$

where superscript * denotes complex conjugate. The coherence estimate is formed according to (2.1).

An example of a coherence estimate according to (2.8) – (2.10) is shown in Figure 2.3 for two normally distributed random records of length 1000 (generated by the Matlab function *randn*) illustrated in Figure 2.1. The length of the FFT was specified as 512 to reduce computational complexity, while the time-bandwidth product *NW* for the discrete prolate spheroidal sequences was chosen to be 4 in a compromise between keeping the spectrum approximately constant within the window and decreasing the possibility of unstable estimates [4].

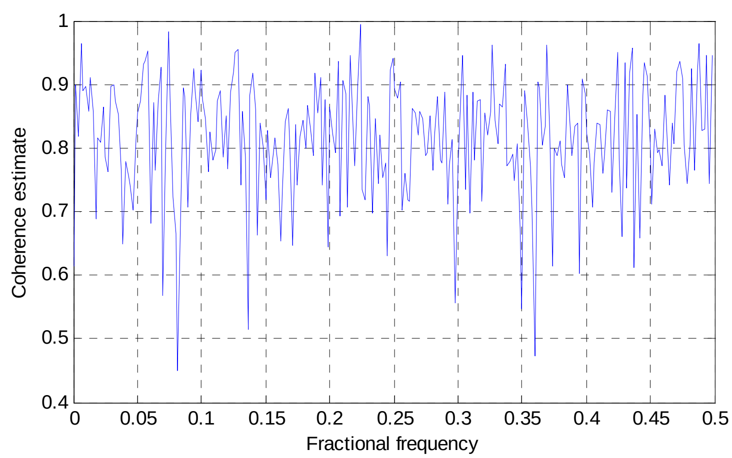

Figure 2.3: An example of the coherence estimate for two random sequences via Thomson's spectra.

The coherence estimate seen in Figure 2.3 does not correspond to the expected low value for all frequencies. Additionally, we can conclude that since the presented method is nonparametric, it may exhibit a fundamentally limited applicability for the processing of short records and frames.

2.2 Magnitude squared coherence function via linear modeling

The study presented next is based on the method proposed by Cadzow and Solomon [10], [11] and presents the results of a statistical analysis of the rational Magnitude Squared (MS) coherence function, as specified by (2.2), and obtained via parametric modeling [10], [11]. This MS coherence estimate has been derived for sequences, whose cross-spectrum and auto-spectra are rational. The MS coherence in this case can be expressed as a ratio of auxiliary polynomials $A(e^{j\omega})$ and $B(e^{j\omega})$ as follows:

$$\Gamma(e^{j\omega}) = \frac{S_{xy}(e^{j\omega}) \cdot S_{yx}(e^{j\omega})}{S_{xx}(e^{j\omega}) \cdot S_{yy}(e^{j\omega})} = \frac{A(e^{j\omega})}{B(e^{j\omega})} \tag{2.11}$$

or as

$$\Gamma_{xy}(e^{j\omega}) = \frac{F_{2q}(e^{j\omega})}{G_{2p}(e^{j\omega})} \tag{2.12}$$

where the polynomials $F_{2q}(e^{j\omega})$ and $G_{2p}(e^{j\omega})$ are symmetric based on the symmetry property of the MS coherence function $\Gamma_{xy}(e^{j\omega}) = \Gamma_{yx}(e^{-j\omega})$ [10], [11].

The essence of the procedure to estimate the MS coherence function, as proposed by Cadzow and Solomon [10], which they titled the near null space approach, consists of the following steps:

1) estimate the cross- and auto-correlation sequences r_{ij} for the records being analyzed;
2) estimate the convolution sums $\hat{a}(n)$ and $\hat{b}(n)$, which are estimates of inverse Fourier transforms of polynomials specified in (2.11), as follows:

$$\begin{aligned} \hat{a}(n) &= \sum_{k=-L}^{L} r_{xy}(k) \cdot r_{yx}(m-k) \\ \hat{b}(n) &= \sum_{k=-L}^{L} r_{xx}(k) \cdot r_{yy}(m-k) \end{aligned} \tag{2.13}$$

where r_{xy} represent correlation estimates between the signals x_n and y_n, for the lags $-L$ to L;

3) choose the model orders p, and q, and the parameter M, and form $\hat{C}_{p,q} = [\hat{A}_p \hat{B}_q]$, such that

$$\begin{array}{ll} \hat{A}_p(m,n) = \hat{a}(m-n) + \hat{a}(m+n-2); & 1 \le n \le p+1; \\ \hat{B}_q(m,n) = -(\hat{b}(m-n) + \hat{b}(m+n-2)); & 1 \le n \le q+1; \end{array} \quad 1 \le m \le M \tag{2.14}$$

4) compute the eigen-decomposition of $\hat{C}^H_{p,q}\hat{C}_{p,q}$;

5) select the s smallest eigenvalues and construct the minimum norm solution as follows:

$$\hat{\theta} = \left(\sum_{k=1}^{s} \hat{v}_k{}^2(1) \right)^{-1} \cdot \sum_{k=1}^{s} \hat{v}_k(1) \cdot \hat{v}_k \tag{2.15}$$

where $\hat{v}_k$ is the k^{th} eigenvector of the $\hat{C}^T_{p,q} \cdot \hat{C}_{p,q}$ matrix and $\hat{C} \cdot \hat{\theta} = 0$.

6) form the rational MS coherence function according to the following expression:

$$\Gamma_{xy}(e^{j\omega}) = \frac{f_q \cdot e^{jq\omega} + \ldots + f_1 \cdot e^{j\omega} + 2 f_0 + f_1 \cdot e^{-j\omega} + \ldots + f_q \cdot e^{-jq\omega}}{g_p \cdot e^{jp\omega} + \ldots + g_1 \cdot e^{j\omega} + 2 + g_1 \cdot e^{-j\omega} + \ldots + g_p \cdot e^{-jp\omega}} \tag{2.16}$$

where $\boldsymbol{f}$ and $\boldsymbol{g}$ are partitions of the minimum norm solution vector as follows:

$$\hat{\theta} = [1, g_1, \ldots, g_p, f_0, \ldots, f_q] \tag{2.17}$$

Cadzow and Solomon show that steps 3 – 5 lead to the solution of the following time domain recursive system of equations [10]:

$$\sum_{n=0}^{p} g_n \left[a(m-n) + a(m+n) \right] - \sum_{n=0}^{q} f_n \left[b(m-n) + b(m+n) \right] = 0 \quad \forall m \tag{2.18}$$

It can be shown [10], [11] that to fully determine the system in (2.18), a total of $M = p + q + 2$ equations is required. If $M > p + q + 2$, the system in (2.18) is called over-determined.

To test the method described above, the numerical example proposed by the authors [10], [11], was examined. We consider two time series generated in accordance with Figure 2.4. The MS coherence function between the white Gaussian noise x_n and the output y_n is estimated. It is seen in Figure 2.4, that the output y_n is a sum of two ARMA processes. We note that without adding the colored noise v_n, the coherence between x_n and y_n would be one for all frequencies.

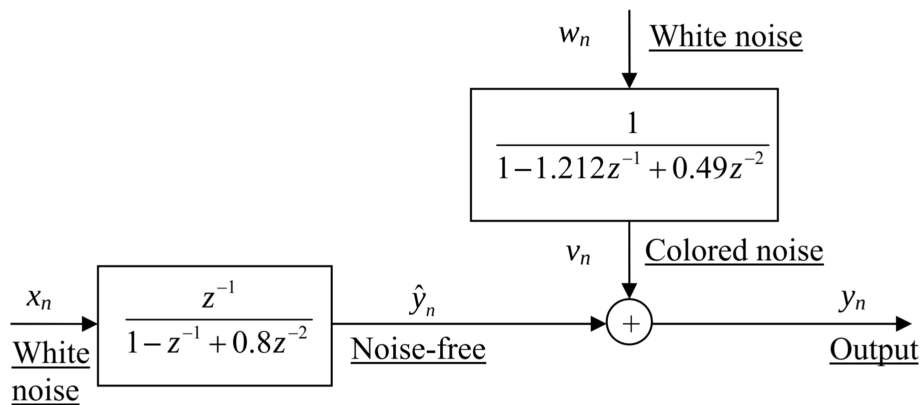

Figure 2.4: Signal generation for the MS coherence Example.

The white noise sequences x_n and w_n are zero-mean, unit-variance. Studying the block diagram in Figure 2.4, we can compute the noise-free response as

$$\hat{y}_n = \hat{y}_{n-1} - 0.8 \cdot \hat{y}_{n-2} + x_{n-1} \tag{2.19}$$

the colored noise as

$$v_n = 1.212 \cdot v_{n-1} - 0.49 \cdot v_{n-2} + w_n \tag{2.20}$$

and the output as

$$y_n = \hat{y}_n + v_n \tag{2.21}$$

The input signals x_n and w_n were generated as 2500 sample-long random Gaussian records. The MS coherence function was estimated according to (2.13) - (2.18) and compared to the theoretical result derived for the known ARMA parameters of the signal generator in Figure 2.4, which is given by the following expression [10], [11]:

$$\Gamma_{theor}(e^{j\omega}) = \frac{0.5066 - 0.6754 \cdot \cos(\omega) + 0.1832 \cdot \cos(2\omega)}{1.0 - 1.3482 \cdot \cos(\omega) + 0.4811 \cdot \cos(2\omega)} \tag{2.22}$$

The auto- and cross-correlation sequences were estimated by the Matlab function *xcorr*, which implements the nonparametric Direct method [14].

The model parameters were chosen as follows: p = 2, q = 2, M = 10, s = 1, which corresponds to the true orders of the numerator and denominator p and q of the MS coherence and over-determination of the estimator by 4. The correlation functions were estimated only for 30 lags to reduce computational complexity. The influence of the number of lags on the accuracy of the estimator will be discussed later. The estimate of MS coherence between *x(n)* and *y(n)*, averaged over 100 independent trials, is shown in Figure 2.5. The true MS coherence evaluated in accordance to (2.22) is presented as well.

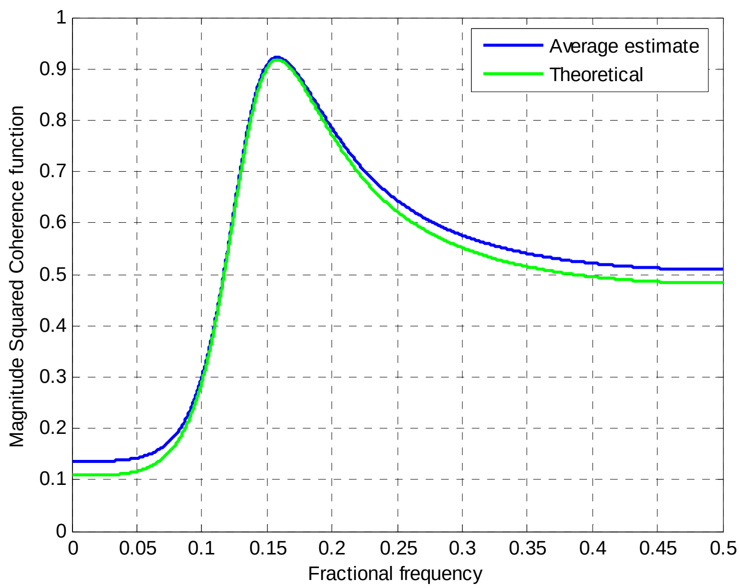

Figure 2.5: True MS coherence and its estimate for $p = 2$, $q = 2$, $M = 10$, $s = 1$.

We see in Figure 2.5 that the mean of the estimate and the theoretical curve are quite close to each other.

To evaluate the statistical properties of the Cadzow/Solomon MS coherence estimator, error graphs for different combinations of estimator parameters were generated. As a measure of the performance, the average relative error (ARE) was computed as follows:

$$\bar{\varepsilon} = \left| \frac{\sum_{\omega} \left(\sum_{n=1}^{Nr} \Gamma_{xy,n}(e^{j\omega}) \Big/ Nr - \Gamma_{theor}(e^{j\omega}) \right)}{\sum_{\omega} \Gamma_{theor}(e^{j\omega})} \right| \tag{2.23}$$

where $\Gamma_{xy}(e^{j\omega})$ and $\Gamma_{theor}(e^{j\omega})$ represent estimated and true coherence functions, respectively.

The MS coherence function was computed for $N_r = 1{,}000$ pairs of signals x_n and y_n with independent noise from trial to trial. The theoretical curve was subtracted from the average of the MS coherence estimate, computed over N_r trials. The result was summed over all frequencies and divided by the sum over all frequencies of the theoretical values.

Additionally, some estimates were unstable, as indicated by spikes at arbitrary fractional frequencies. These solutions were ignored but their number was counted to provide another measure of performance, called the probability of unstable solution (POUS).

Figures 2.6 and 2.7 represent the results of statistical experiments investigating the influence of the model parameters on the ARE and POUS of the MS coherence estimate. All presented graphs are averages over 1,000 independent trials unless specified. Figure 2.6 shows the dependence of ARE and POUS on the value of M, the number of equations used to compute the minimum norm solution. The graphs were plotted for different orders p and q and different numbers s of eigenvalues.

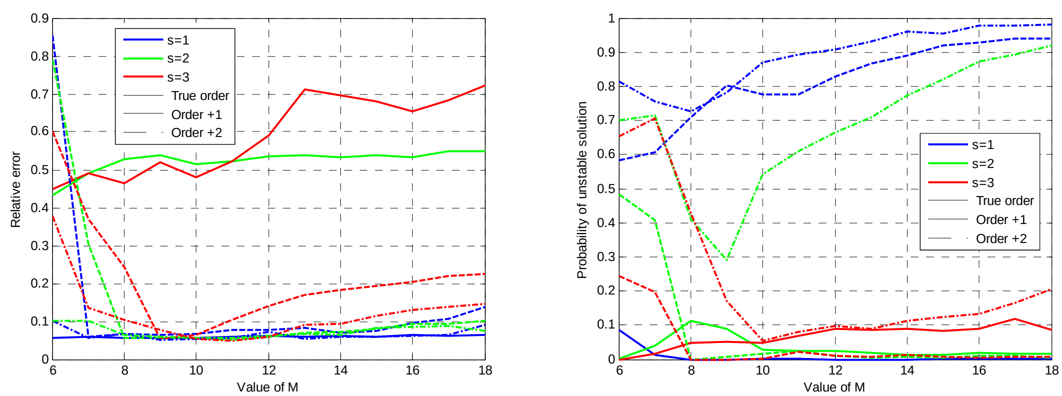

(a) (b)

Figure 2.6: ARE (a) and POUS (b) of the estimator for different M.

The simulations show a high sensitivity of the Cadzom/Solomon coherence estimator to parameter choice. Namely, for the true orders, the average relative error is observed to be unacceptably high when more than one eigenvector is used to form the solution. Such dependence was not observed when the model order was over-estimated. For the range of orders and number of eigenvalues studied, the estimator tends to produce the lowest ARE when M is between 8 and 10. Figure 2.6 suggests that to obtain the lowest ARE and POUS the following must hold true: $s = p - 1$ and $M = p + q + 2$.

Figure 2.7 illustrates the influence on the accuracy of the estimator of the number of lags over which the correlation sequence is estimated. The experiment was performed on 2500 sample-long records for the following sets of parameters: 1) $p = 2, q = 2, s = 1, M = 8$, 2) $p = 3, q = 3, s = 2, M = 8$, and 3) $p = 4, q = 4, s = 2, M = 8$.

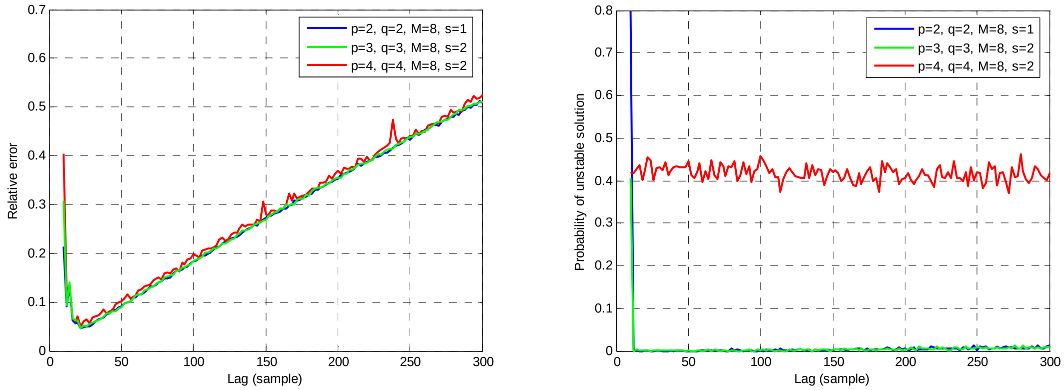

(a) (b)

Figure 2.7: ARE (a) and POUS (b) of the estimator for different lags of correlation estimate.

Figure 2.7 suggests that ARE increases when the correlation sequences are estimated for more and more lags. The lowest error is observed when correlations are estimated for 22 lags. On the other hand, the probability of unstable solution does not depend on the number of correlation estimate lags.

We conclude that the performance of the Cadzow/Solomon coherence method is greatly influenced by the number of lags used to obtain the correlation sequence estimates.

2.3 Comparison of different correlation estimates for the magnitude squared coherence estimator

In this section several correlation estimators are implemented and their performance evaluated in the context of the Magnitude Squared Coherence estimator proposed by Cadzow and Solomon [10], [11].

The first correlation estimator analyzed implements the Direct correlation estimator (D) as follows [14]:

$$\hat{r}_{D,k} \equiv \frac{\sum_{i=0}^{N-1}\left(x_i \cdot y_{i+k}\right)}{\sqrt{\sum_{i=0}^{N-1} x_i{}^2 \cdot \sum_{i=0}^{N-1} y_{i+k}{}^2}} \qquad (2.24)$$

where $\hat{r}_{D,k}$ is an estimate of the cross-correlation coefficient between records x_n and y_n for the lag index k. The auto-correlation for the record x_n can be obtained by replacing y by x. The records x_n and y_n analyzed must have the same length N. The subscript d indicates the Direct method of correlation estimation is implemented.

The second correlation estimation algorithm executes the *Double Absolute Difference Average* estimator (Double ADA) [14], [15]:

$$\hat{r}_{DADA,k} \equiv \frac{\left(\sum_{i=0}^{N-1}\left|x_i + y_{i+k}\right|\right)^2 - \left(\sum_{i=0}^{N-1}\left|x_i - y_{i+k}\right|\right)^2}{\left(\sum_{i=0}^{N-1}\left(\left|x_i\right| + \left|y_{i+k}\right|\right)\right)^2} \qquad (2.25)$$

The third - *Relative Magnitude* estimator (RM) - is expressed as [15]

$$\hat{r}_{RM,k} \equiv \frac{\left(\sum_{i=0}^{N-1}\left|x_i + y_{i+k}\right|\right)^2 - \left(\sum_{i=0}^{N-1}\left|x_i - y_{i+k}\right|\right)^2}{\left(\sum_{i=0}^{N-1}\left|x_i + y_{i+k}\right|\right)^2 + \left(\sum_{i=0}^{N-1}\left|x_i - y_{i+k}\right|\right)^2} \qquad (2.26)$$

Finally, the *robust* correlation estimator via *Bi-weight Midcovariance* (BwM) was implemented as follows [16]:

$$\hat{r}_{B,k} \equiv \frac{s_{b,xy,k}}{\sqrt{s_{b,xx,k} \cdot s_{b,yy,k}}} \qquad (2.27)$$

where $s_{b,xy,k}$ is a biweight mid-covariance between records x_n and y_n, specified as

$$s_{b,xy,k} = \frac{N\sum_{i=0}^{N-1} a_i (x_i - M_x)(1 - U_i{}^2)^2 b_{i+k}(y_{i+k} - M_y)(1 - V_{i+k}{}^2)^2}{\left(\sum_{i=0}^{N-1} a_i (1 - U_i{}^2)(1 - 5U_i{}^2)\right) \cdot \left(\sum_{i=0}^{N-1} b_{i+k}(1 - V_{i+k}{}^2)(1 - 5V_{i+k}{}^2)\right)} \qquad (2.28)$$

Here M_x is the median of x_n, and U_i is computed as follows:

$$U_i = \frac{x_i - M_x}{9 \cdot MAD_x} \qquad (2.29)$$

where MAD_x is the median absolute deviation

$$MAD_x = Median\{|x_1 - M_x|,\ldots,|x_N - M_x|\} \tag{2.30}$$

The coefficient a_i is specified as follows:

$$a_i = \begin{cases} 1 & |U_i| \le 1 \\ 0 & otherwise \end{cases} \tag{2.31}$$

The corresponding coefficients and function associated with the y_n record are defined analogously.

To study the performance of the Cadzow/Solomon algorithms when using these various correlation estimators, two normally distributed real random signals of length 100 with zero mean and unit variance were generated, with an example seen in Figure 2.1.

Autocorrelation estimates for the Direct, Double ADA, and RM methods are shown in Figure 2.8. Similarly, cross-correlation estimates are shown in Figure 2.9.

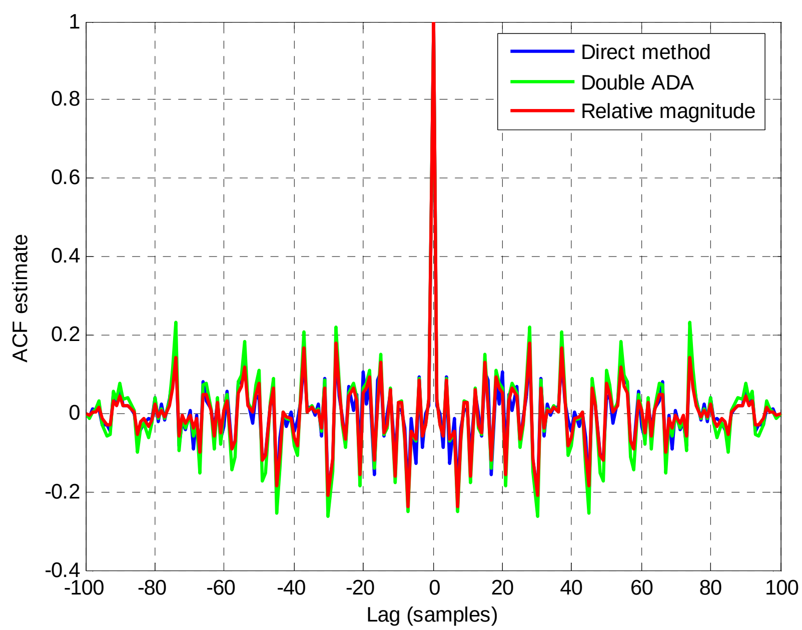

Figure 2.8: Autocorrelation sequences estimated by different methods.

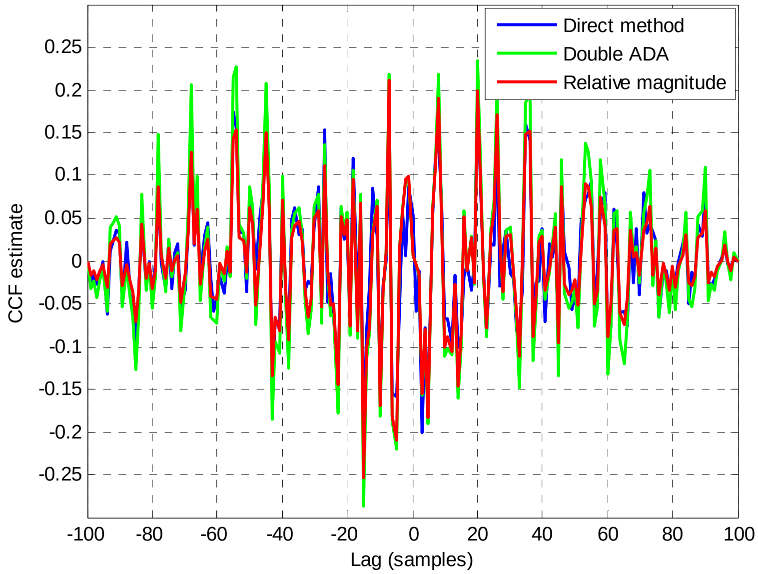

Figure 2.9: Cross-correlation sequences estimated by different methods.

We observe in Figures 2.8 and 2.9 that all three estimates are close to each other for small lags.

The autocorrelation estimate obtained by the Direct method was compared to the autocorrelation sequence estimated for the same random signal by the Matlab function *xcorr*. The difference (absolute error) between these two sequences is seen in Figure 2.10.

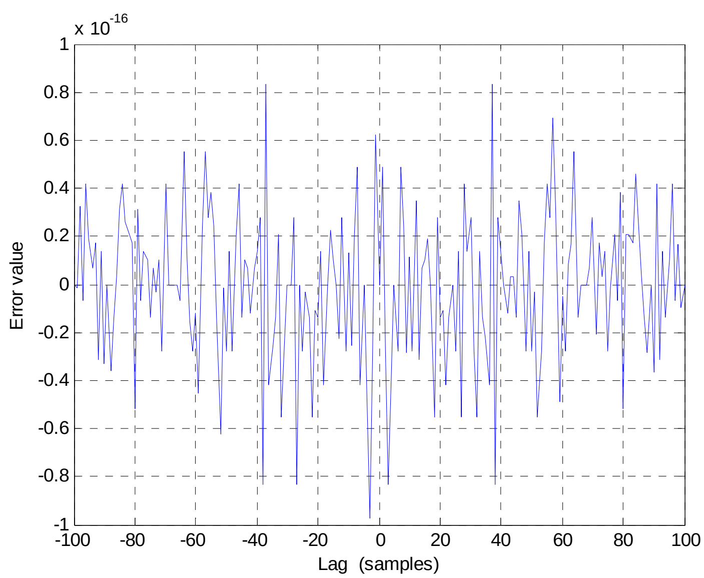

Figure 2.10: Absolute error between the Matlab ACF estimate and the ACF estimate obtained via the Direct method.

We see in Figure 2.10 that the difference does not exceed the magnitude of the value of Matlab ε. Based on this observation, we may conclude that Matlab implements the Direct method and the performance resulting from using the Matlab function *xcorr* and the performance of the Direct method is expected to be approximately the same.

Figures 2.11 and 2.12 present a comparison between auto- and cross-correlation estimates obtained by the Direct and robust methods. The same random sequences were used.

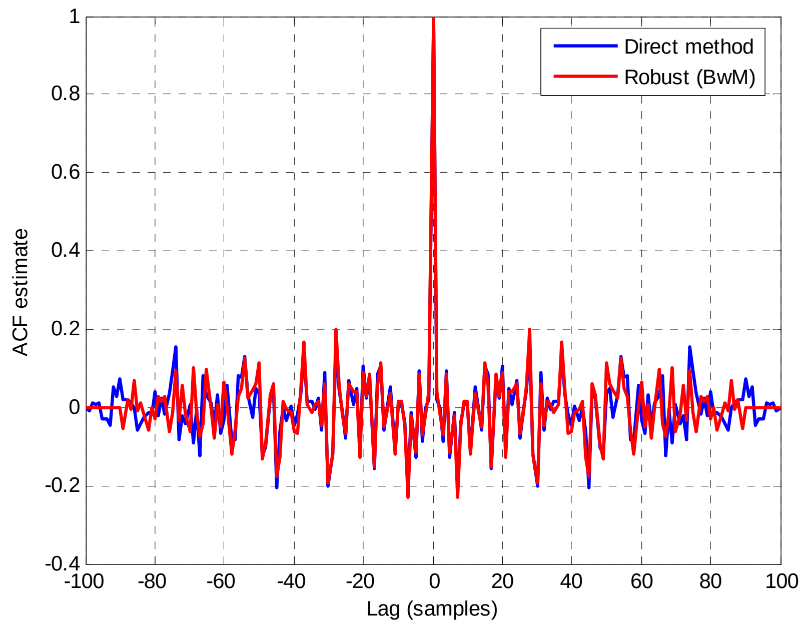

Figure 2.11: Autocorrelation sequences estimated by the Direct method and the BwM robust method.

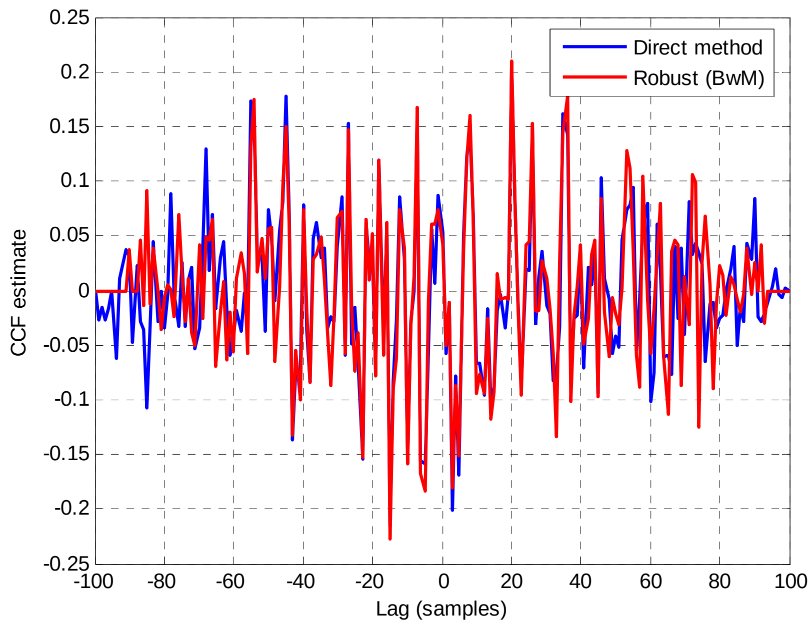

Figure 2.12: Cross-correlation sequences estimated by the Direct method and the BwM robust method.

Visual inspection of Figures 2.11 and 2.12 shows that the results obtained by the Direct method and the BwM robust estimator are relatively close for small lags (up to lag = 25).

Next, all the correlation estimators considered here were used in combination with the MS coherence estimator described in Section 2.2. Each graph in Figures 2.13 to 2.17 was generated by averaging over 1,000 trials with independent noise. The length of the record was 2,500 samples, and the correlation sequences were estimated for 30 lags since this number is close to the suboptimal number of lags causing the lowest ARE as shown in Figure 2.7. The MS coherence estimates were obtained for the following parameters: $p = 2$, $q = 2$, $M = 10$, $s = 1$. The corresponding ARE is presented in the legends as well.

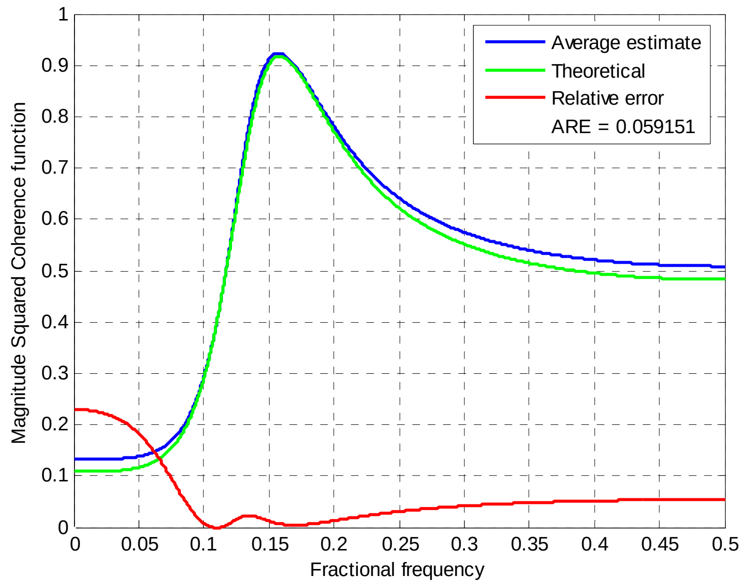

Figure 2.13: True MS coherence and its estimate for the Section 2.2 Example; Direct method, POUS = 0.007.

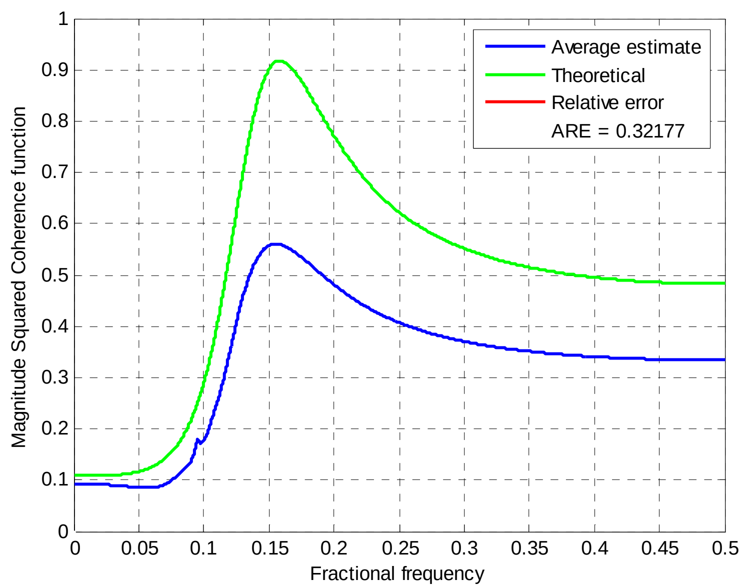

Figure 2.14: True MS coherence and its estimate for the Section 2.2 Example; double ADA method, POUS = 0.405.

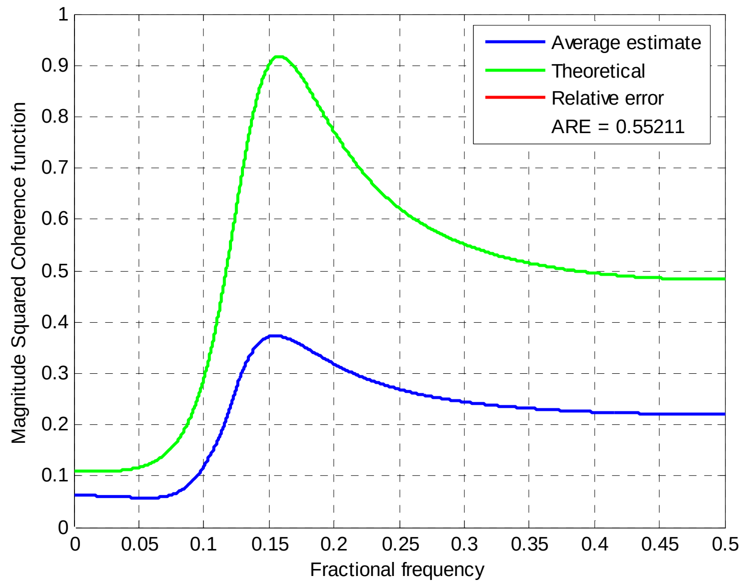

Figure 2.15: True MS coherence and its estimate for the Section 2.2 Example; relative magnitude method, POUS = 0.366.

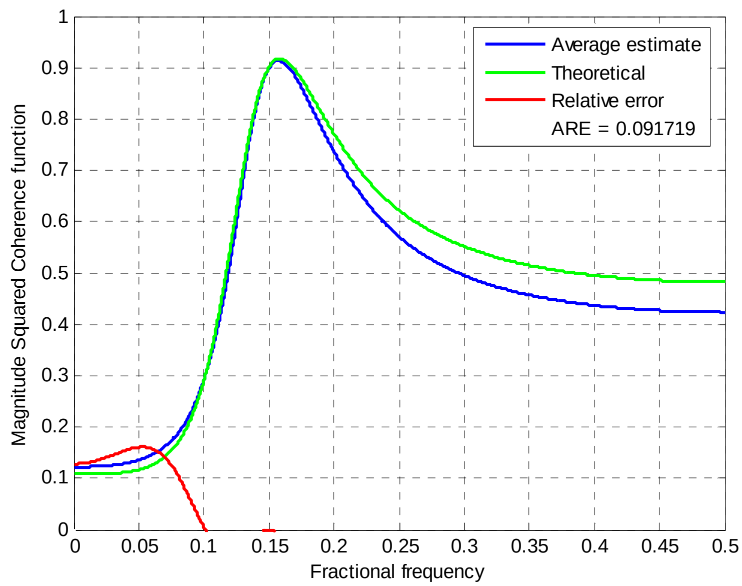

Figure 2.16: True MS coherence and its estimate for the Section 2.2 Example; BwM robust method, POUS = 0.003.

Figures 2.13 – 2.16 show that the double ADA and relative magnitude estimators tend to produce coherence estimates with large ARE (ARE is out of the range depicted in Figure 2.14 and 2.15, therefore, not shown) and a large probability of unstable solution.

The BwM robust estimator yields a lower probability of unstable solution, compared to the Direct method, however, the corresponding relative error is slightly higher.

Figure 2.17 illustrates the influence of a different number of correlation lags on the accuracy of the coherence estimate obtained for 2500 sample-long records. The processing has been performed for the following parameters: $p = 2$, $q = 2$, $M = 10$, $s = 1$. The average over 100 trials with independent noise is presented.

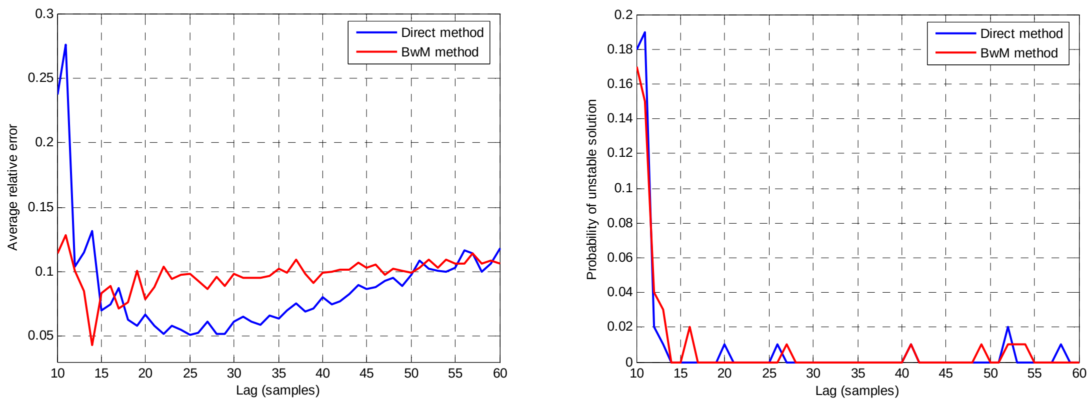

(a) (b)

Figure 2.17: ARE (a) and POUS (b) of coherence estimates using the Direct and robust methods for correlation estimation.

We observe in Figure 2.17 that the coherence estimator, whether using the Direct or the robust method of correlation estimation, exhibits sensitivity to the number of lags of correlation estimates used in their computation. The smallest ARE was observed when correlation was estimated by the Direct method for 19-24 lags. The robust estimator causes higher ARE but more stable solutions as seen in the right part of Figure 2.17.

Next, the influence of the length of the analyzed frames on the accuracy of the coherence estimate using different correlation estimators was examined. The true order coherence with $p = 2$, $q = 2$, $M = 10$, $s = 1$ was estimated and averaged over 100 experiments with independent noise. The ARE and POUS are shown in Figure 2.18. The zoomed versions of the plots are presented in Figure 2.18 as well.

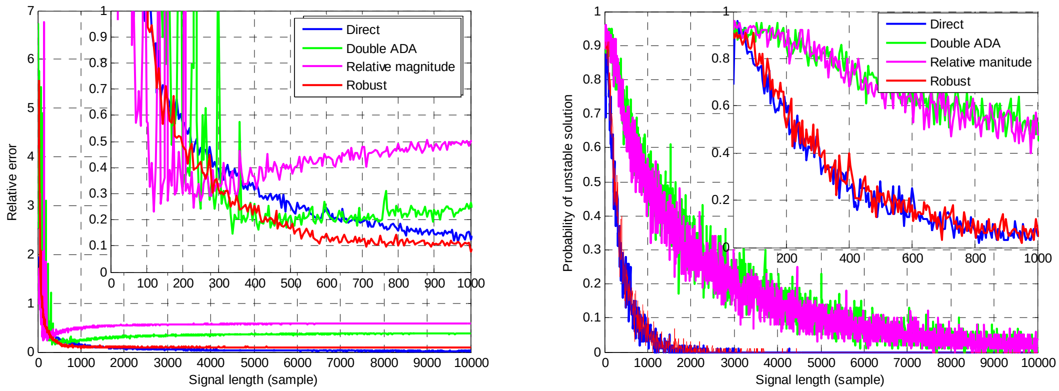

(a) (b)

Figure 2.18: ARE (a) and POUS (b) of coherence estimates using different correlation estimators.

We observe in Figure 2.18 that the double ADA and relative magnitude correlation estimators perform considerably worse than the Direct and Robust methods. The BwM robust estimator exhibits a smaller relative error than the Direct method when the signal frame is varied from approximately 150 to approximately 1100 samples. However, when record length exceeds approximately 1800, the Direct estimator outperforms the BwM robust estimator. Another important observation is the unacceptably high probability of unstable solution when processing frames shorter than 1,000 samples, for any of the correlation estimators evaluated here. This implies that the coherence estimator exhibits very limited capability of processing short sequences, regardless of the correlation estimator it uses. This limitation is fundamental and may well originate from the fact that the above correlation estimators are all non-parametric.

2.4 References

[1] M. H. Hayes, *Statistical digital signal processing and modeling.* John Wiley and sons, 1996.

[2] E. M. Glaser and D. S. Ruchkin, *Principles of neurobiological signal analysis.* Academic Press, 1976.

[3] D. J. Thomson, "Estimation of coherence between complicated processes," *Spectrum estimation and modeling*, 1990, 5th ASSP workshop on, 10-12 Oct. 1990, pp. 256-260.

[4] D. J. Thomson, "Jackknifing multiple-window spectra," *Acoustics, Speech, and Signal Processing*, 1994. ICASSP – 94, 1994 IEEE International Conference on, vol. VI, 19 – 22 April 1994, pp. VI73-VI76.

[5] D. J. Thomson, "Spectrum estimation and harmonic analysis," *Proceedings of the IEEE*, vol. 70, #9, September 1982, pp. 1055-1096.

[6] R. D. Martin and D. J. Thomson, "Robust-resistant spectrum estimation," *Proceedings of the IEEE*, vol. 70, #9, September 1982, pp. 1097-1115.

[7] D. Slepian and H. O. Pollak, "Prolate spheroidal wave functions, Fourier analysis and uncertainty, I," *Bell System Technical Journal*, vol. 40, #1, January, 1961, pp. 43-63.

[8] D. Slepian and H. O. Pollak, "Prolate spheroidal wave functions, Fourier analysis and uncertainty, II," *Bell System Technical Journal*, vol. 40, #1, January, 1961, pp. 65-84.

[9] D. Slepian and H. O. Pollak, "Prolate spheroidal wave functions, Fourier analysis and uncertainty, V: the discrete case," *Bell System Technical Journal*, vol. 57, #5, May – June, 1978, pp. 1371-1430.

[10] J. A. Cadzow and O. M. Solomon, Jr., "Linear modeling and the coherence function," *IEEE Transactions on Acoustics, Speech, and Signal Processing*, vol. ASSP-35, #1, January 1987, pp. 19-28.

[11] O. M. Solomon, Jr., *Linear modeling and the coherence function: an algebraic approach*, *PhD Dissertation*, Univ. New Mexico, Albuquerque, Dec. 1985.

[12] W. A. Gardner, *Introduction to random processes: with applications to signals and systems.* - Second edition. McGraw-hill Publishing Company, 1989.

[13] L. H. Koopmans, "The spectral analysis of time series," vol. 22 in *Probability and mathematical statistics.* Academic Press, 1995.

[14] G. Jacovitti and R. Cusani, "An efficient technique for high correlation estimation," *IEEE Transactions on Acoustics, Speech, and Signal Processing*, vol. ASSP-35, #5, May 1987, pp. 654-660.

[15] G. Guinta, "A note on the computational complexity of high correlation estimators," *IEEE Transactions on Signal Processing*, vol. 39, #2, February 1991, pp. 485-486.

[16] R. Wilcox, *Introduction to Robust Estimation and Hypothesis Testing*. Academic Press, New York, 1997.

Chapter 3

Phase Synchrony

Phase Synchrony (PS) is the frequency-specific quantity $r_{lm,n}$ specified for two oscillators l and m, over an N_w sample long time window as follows [1], [2], [3], and [4]:

$$r_{lm,n} = \left| \frac{1}{N_w} \sum_{k=n-N_w+1}^{n} e^{-j(\varphi_{lk} - \varphi_{mk})} \right| \tag{3.1}$$

where φ_{lk} and φ_{mk} denote instantaneous phase sequences for oscillators l and m respectively and n represents the last time instant included in its evaluation.

We will adopt the following interpretation of phase synchrony:

1) PS is expected to be close to one when two sequences at the same frequency are processed;

2) PS is expected to be close to zero, when two sequences at different frequencies are analyzed.

Next, we investigate the properties of phase synchrony.

3.1 Fundamental properties of phase synchrony

The properties of phase synchrony were studied on two signal pairs, generated based on the presented interpretation of PS, as sinusoids of a particular frequency contaminated by white noise with SNR = 10 dB. We studied two types of signal pairs. In the high synchrony pair both signals contain noisy sinusoidal sequences of a particular frequency, i.e. the analyzed signals were noisy sinusoids of the same frequency with a constant phase shift between them (Figure 3.1 (a)). In the low synchrony pair one of the signals was normally distributed white noise (Figure 3.1 (b)).

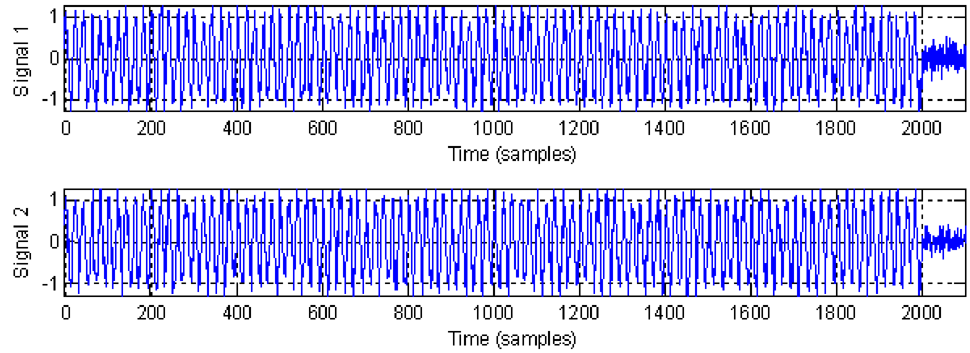

(a)

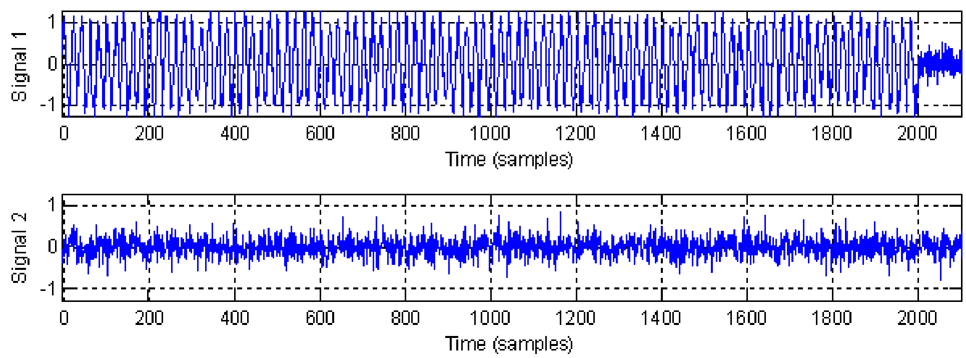

(b)

Figure 3.1: Signal pairs with (a) high and (b) low synchrony; $f_0 = 0.05$, SNR = 10 dB.

We see that when two input signals are at the same frequency, the phase difference $\Delta\varphi_k = \varphi_{lk} - \varphi_{mk}$ between them is constant and the PS is

$$
\begin{aligned}
r_{lm,n} &= \left| \frac{1}{N_w} \sum_{k=n-N_w+1}^{n} e^{-j\Delta\varphi_k} \right| = \\
&\frac{1}{N_w} \left| N_w \cdot e^{-j\Delta\varphi_k} \right| = \\
&\frac{1}{N_w} \cdot N_w \left| \cos(\Delta\varphi_k) - j\sin(\Delta\varphi_k) \right| = \\
&1 \cdot \sqrt{\cos^2(\Delta\varphi_k) + \sin^2(\Delta\varphi_k)} \equiv 1
\end{aligned}
\tag{3.2}
$$

Evaluation of the expected value of PS for two sequences not at the same frequency is more challenging. We will estimate the expected value of PS for a low synchrony case. Assuming for simplicity that $n = N_w$, i.e. the summation is performed from 1 to N_w, phase synchrony can be rewritten as follows:

$$
\begin{aligned}
r_{lm,n} &= \left| \frac{1}{N_w} \sum_{k=1}^{N_w} e^{-j\Delta\varphi_k} \right| \\
&= \frac{1}{N_w} \left| \sum_{k=1}^{N_w} \left(\cos\Delta\varphi_k - j\sin\Delta\varphi_k \right) \right| \\
&= \frac{1}{N_w} \left| \sum_{k=1}^{N_w} \cos\Delta\varphi_k - j\sum_{k=1}^{N_w} \sin\Delta\varphi_k \right| \\
&= \frac{1}{N_w} \sqrt{ \left(\sum_{k=1}^{N_w} \cos\Delta\varphi_k \right)^2 + \left(\sum_{k=1}^{N_w} \sin\Delta\varphi_k \right)^2 } \\
&= \frac{1}{N_w} \sqrt{ N_w + 2\sum_{i=1}^{N_w-1} \sum_{k=i+1}^{N_w} (\cos\Delta\varphi_i \cos\Delta\varphi_k + \sin\Delta\varphi_i \sin\Delta\varphi_k) }
\end{aligned}
\tag{3.3}
$$

Since $\cos\Delta\varphi_i \cos\Delta\varphi_k + \sin\Delta\varphi_i \sin\Delta\varphi_k = \cos(\Delta\varphi_i - \Delta\varphi_k)$ [5], phase synchrony is

$$
r_{lm,n} = \frac{1}{N_w} \sqrt{ N_w + 2\sum_{i=1}^{N_w-1} \sum_{k=i+1}^{N_w} \cos(\Delta\varphi_i - \Delta\varphi_k) } \tag{3.4}
$$

When a low synchrony signal pair is processed, the phase difference $\Delta\varphi_k$ between two signals can be modeled as a uniformly distributed random variable (RV) over [-π π], since it is a sum of a constant and a uniformly distributed RV. A sum of two independent identically distributed RVs is another RV, whose probability density function (PDF) is a convolution of the initial PDFs [6]. Namely, if two initial RVs are uniformly distributed, their sum (or difference) will have a triangular distribution. We can make the substitution $\tilde{\varphi}_{ik} = \Delta\varphi_i - \Delta\varphi_k$, where the PDF of $\tilde{\varphi}_{ik}$ is

$$
f_{\tilde{\varphi}}(\tilde{\varphi}) = \begin{cases} \dfrac{2\pi + \tilde{\varphi}}{4\pi^2} & when \ -2\pi \le \tilde{\varphi} \le 0 \\ \dfrac{2\pi - \tilde{\varphi}}{4\pi^2} & when \quad 0 < \tilde{\varphi} \le 2\pi \\ 0 & otherwise \end{cases} \tag{3.5}
$$

The theoretical PDFs and their experimental approximations for the initial random variable $\Delta\varphi_k$ and triangularly distributed $\tilde{\varphi}_{ik}$ are illustrated in Figure 3.2. The experimental histograms have been plotted for 100,000 uniformly distributed random numbers over [-π π] (Figure 3.2 (a)) and for 100,000 differences of two such identically and uniformly distributed random numbers (Figure 3.2 (b)).

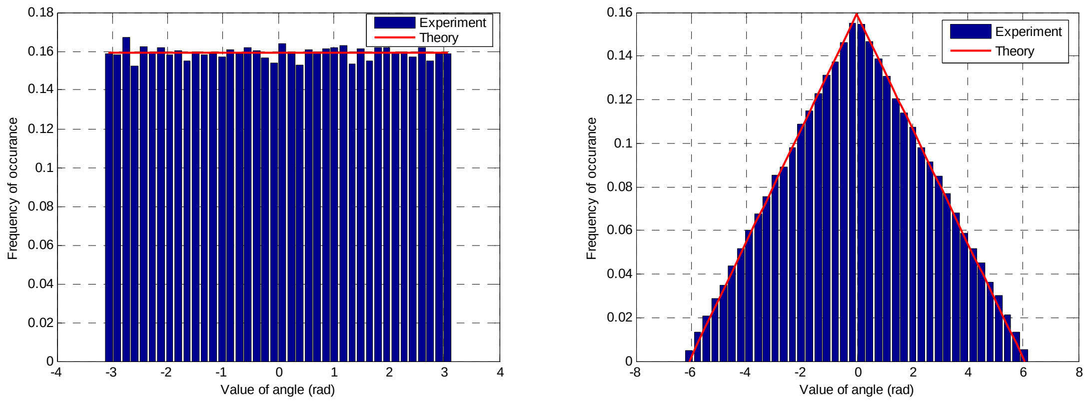

(a) (b)

Figure 3.2: Theoretical PDFs for (a) uniformly and (b) triangularly distributed RVs and their experimental approximations.

Substituting $\tilde{\varphi}_{ik} = \Delta\varphi_i - \Delta\varphi_k$, phase synchrony can be simplified as follows:

$$r_{lm,n} = \frac{1}{N_w}\sqrt{N_w + 2\sum_{i=1}^{N_w-1}\sum_{k=i+1}^{N_w}\cos\tilde{\varphi}_{ik}} \tag{3.6}$$

and, by another substitution $\psi_{ik} = \cos\tilde{\varphi}_{ik}$, we find (3.7)

$$r_{lm,n} = \frac{1}{N_w}\sqrt{N_w + 2\sum_{i=1}^{N_w-1}\sum_{k=i+1}^{N_w}\psi_{ik}} \tag{3.8}$$

The distribution of ψ_{ik} can be evaluated using the Fundamental Theorem of statistics [6] that specifies the PDF of a function of random variable with known distribution. Before these derivations, the following remarks must be made. The cosine is a periodic function with period of 2π. Because of the symmetry around π, $\cos(\pi+\theta) = \cos(\pi-\theta)$, which transforms the triangular PDF of $\tilde{\varphi}$, shown on the right part of Figure 3.2, to a distribution uniform over [-π π], as Figure 3.3 illustrates.

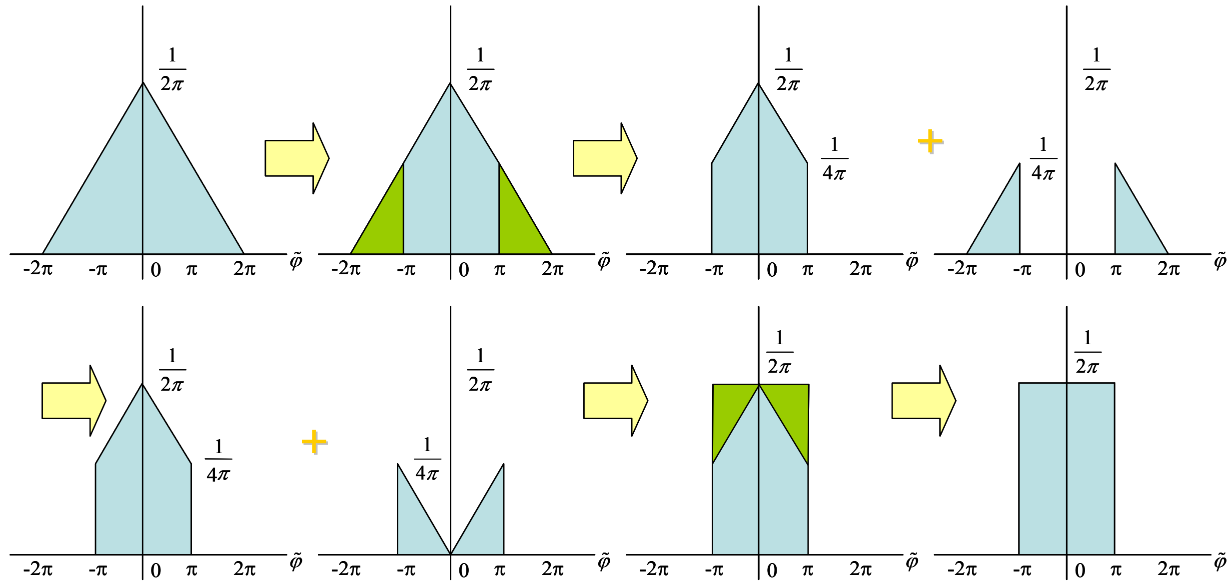

Figure 3.3: Diagram of PDF transformation.

Applying the Fundamental Theorem [6], we can find the PDF of ψ specified in (3.7) via the following steps:

Two solutions of (3.7) exist for $\tilde{\varphi}$ in [-π π] for given ψ, namely:

$\tilde{\varphi}_1 = \cos^{-1}(\psi)$ and $\tilde{\varphi}_2 = -\cos^{-1}(\psi)$.

Differentiation of (3.7) leads to $\frac{d}{d\tilde{\varphi}}\left(\cos\tilde{\varphi}\right) = -\sin\tilde{\varphi}$. Finally, the resulting PDF can be expressed according to the Fundamental Theorem of statistics as follows:

$$\begin{aligned} f_\psi(\psi) &= \frac{1/2\pi}{\left|-\sin(\cos^{-1}\psi)\right|} + \frac{1/2\pi}{\left|-\sin(-\cos^{-1}\psi)\right|} \\ &= \frac{1}{\pi\sin(\cos^{-1}\psi)} \qquad \text{for } -1 \le \psi \le 1 \end{aligned} \tag{3.9}$$

A plot of the theoretical PDF corresponding to (3.9), and its experimental approximation obtained for 100,000 independent RV generated in accordance to (3.7) and the previous discussion, is shown in Figure 3.4.

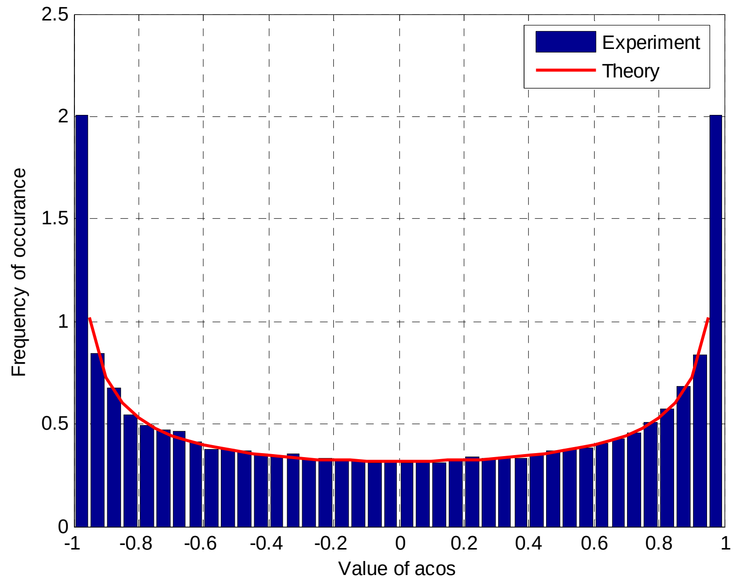

Figure 3.4: Theoretical PDF for RV distributed corresponding to (3.7) and its experimental approximation.

The histogram in Figure 3.4 closely matches the theoretical curve. The expected value (mean) of distribution (3.7) can be found as

$$\begin{aligned} E\{\psi\} &= \int_{-1}^{1} f_{\psi}(\psi)\psi d\psi = \\ &= \frac{1}{\pi}\int_{-1}^{1} \frac{\psi}{\sin(\cos^{-1}(\psi))} d\psi = 0 \end{aligned} \tag{3.10}$$

The second moment is estimated as

$$\begin{aligned} E\{\psi^2\} &= \int_{-1}^{1} f_{\psi}(\psi)\psi^2 d\psi = \\ &= \frac{1}{\pi}\int_{-1}^{1} \frac{\psi^2}{\sin(\cos^{-1}(\psi))} d\psi = 0.5 \end{aligned} \tag{3.11}$$

To further simplify the expression for phase synchrony in (3.8), we apply the substitution:

$$\xi_n = \frac{1}{N_w{}^2} \sum_{i=1}^{N_w-1} \sum_{k=1}^{N_w-i} \psi_{ki} \tag{3.12}$$

which transforms the expression for phase synchrony into

$$r_{lm,n} = \frac{1}{N_w}\sqrt{N_w + 2\sum_{i=1}^{N_w-1}\sum_{k=1}^{N_w-i}\psi_{ki}} = \\ = \sqrt{\frac{1}{N_w} + \frac{2}{N_w{}^2}\sum_{i=1}^{N_w-1}\sum_{k=1}^{N_w-i}\psi_{ki}} \tag{3.13}$$

Finally, we therefore have the following

$$\boxed{r_{lm,n} = \sqrt{\frac{1}{N_w} + 2\xi_n}} \tag{3.14}$$

The RV ξ_n in (3.12) can be approximated as a shifted exponential random process with the PDF expressed as follows:

$$f_\xi(\xi) = \lambda e^{-\lambda\left(\xi + \frac{1}{2\lambda}\right)} \tag{3.15}$$

where $\lambda = N_w$. (3.16)

Or, finally:
$$f_\xi(\xi) = N_w e^{-N_w\left(\xi + \frac{1}{2N_w}\right)} \tag{3.17}$$

A plot of the theoretical PDF corresponding to (3.17) and its experimental approximation obtained for 100,000 independent RV generated in accordance to (3.12) and the previous discussion, is shown in Figure 3.5.

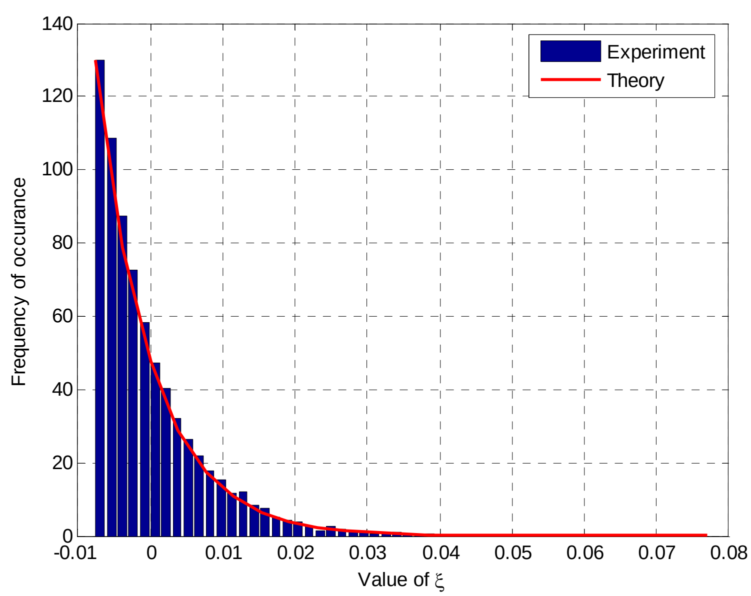

Figure 3.5: Theoretical PDF for RV distributed corresponding to (3.17) and its experimental approximation for $N = 130$.

The histogram in Figure 3.5 closely matches the theoretical curve.

Finally, the expected value of phase synchrony as expressed in (3.14) can be evaluated as follows [6]:

$$
\begin{aligned}
E\{r\} &= \int_{-\infty}^{\infty} f_r(r) \cdot r \cdot dr = \\
&= \int_0^1 r \cdot f_\xi(\xi) \cdot d\xi = \\
&= N_w \int_0^1 \sqrt{\frac{1}{N_w} + 2\xi} \cdot e^{-N_w\left(\xi + \frac{1}{2N_w}\right)} d\xi
\end{aligned}
\tag{3.18}
$$

The resulting integral can be evaluated numerically. The result of this evaluation (the theoretical expected value of phase synchrony) and the experimental average of phase synchrony specified in (3.1) over 1,000 trials with independent noise are shown in Figure 3.6.

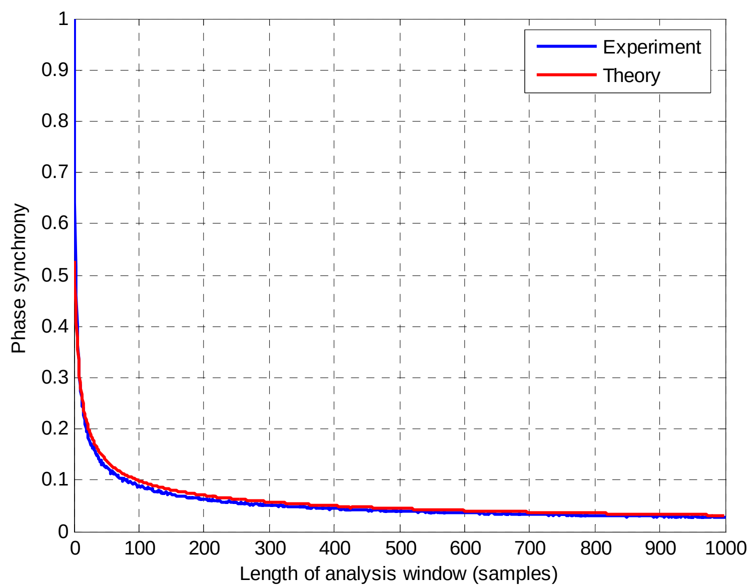

Figure 3.6: Averaged value of phase synchrony and its theoretical estimate for different lengths of the analysis window.

We observe from Figure 3.6 that the theoretical and experimental results are close. Based on these graphs, we can conclude that the expected value for phase synchrony for a low synchrony signal pair is not zero and principally depends on the length of the analysis window.

Analyzing the graphs shown in Figure 3.6, we can conclude that the expected value of phase synchrony in the low synchrony case is governed by the following equation:

$$E\{r\} \approx \frac{1}{\sqrt{N_w}} \tag{3.19}$$

The expected value of phase synchrony, when processing two random sequences, can be evaluated using the approach described above. In this case, the initial phase difference is triangularly distributed. As a result, the PDF of $\tilde{\varphi}$ is a convolution of two triangles. Since each triangle is defined over the [-2π 2π] interval, the resulting convolution will be defined over the [-4π 4π] interval. However – due to the symmetry around π of the cosine – this distribution will be transformed to being uniform over the [-4π 4π] range, similar to the illustration in Figure 3.5. The rest of the derivation remains unchanged. Consequently, the expected value of phase synchrony in the case of two random input sequences can be found by the expression in (3.18).

3.2 Design of - and parameter selection for - the Phase Synchrony Processor

To apply phase synchrony analysis (3.1) to the generated pairs of signals shown in Figure 3.1, we need to extract the frequency specific instantaneous phase sequences. To accomplish this, we first generate the analytic sequence corresponding to the given signal and then extract the frequency specific content for the frequency band (or EEG rhythm) of interest. These goals can be attained by the Instantaneous Phase Processor (IPP) depicted in Figure 3.7 [7]. The advantage of the IPP, compared to wavelet filtering, is better parameter flexibility as the analysis time, the center frequency, and the bandwidth of the processor can be adjusted independently.

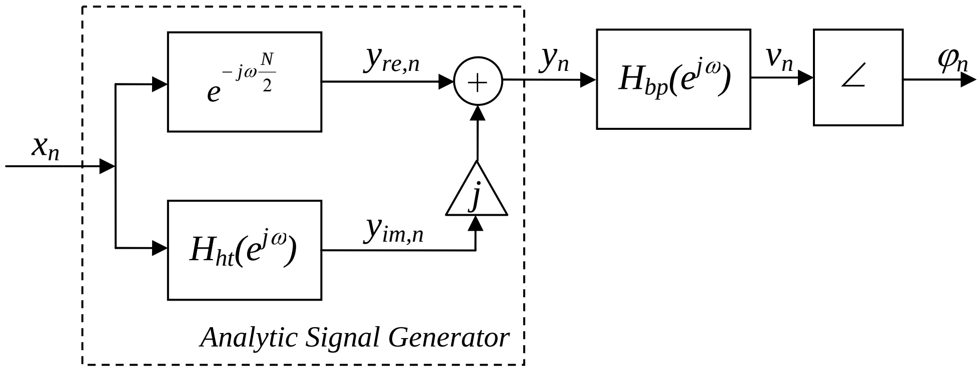

Figure 3.7: Frequency specific Instantaneous Phase Processor (IPP).

The filter $H_{ht}(e^{j\omega})$ is a Kaiser-window based linear-phase FIR approximation of the ideal Hilbert transformer evaluated as follows [8]:

$$h_{ht,FIR}[n] = \begin{cases} \dfrac{I_0\{\beta\sqrt{1-[(n-n_d)/n_d]^2}}{I_0(\beta)} \cdot \dfrac{2}{\pi} \cdot \dfrac{\sin^2\{\pi(n-n_d)/2\}}{n-n_d}, & 0 < n < N \\ 0, & otherwise \end{cases} \tag{3.20}$$

where N+1 is the specified length of the Hilbert transformer FIR approximation (N+1 = 19 was used in this study), $n_d = N/2$, β is a parameter that controls the smoothness of spectral transition. To achieve a peak approximation error of about -35 dB, the design parameter β was chosen as 2.629 [9].

The real part of the analytic signal y_n is the real input signal delayed by $N/2$ samples (9 in our case). The band-pass filter $H_{bp}(e^{j\omega})$ was implemented as an equiripple FIR filter with adjustable center frequency f_c and adjustable bandwidth B. The length of the filter was estimated for the pass-band and stop-band ripples chosen as 0.01 and the given B.

To process a pair of signals according to (3.1), the Phase Synchrony Processor (PSP), depicted in Figure 3.8, is employed.

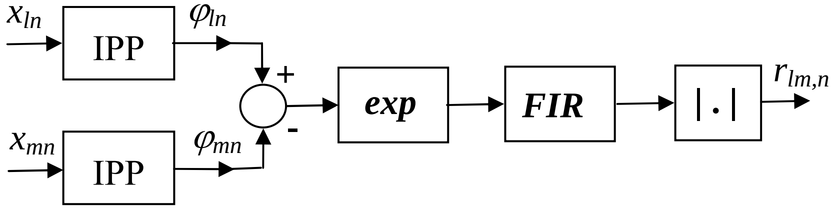

Figure 3.8: Phase Synchrony Processor.

The instantaneous phase sequences associated with the two input signals x_{ln} and x_{mn} are generated by two identical IPPs, subtracted, and their difference used to produce the corresponding unit magnitude phasor. The resulting sequence of phasors is filtered by the FIR filter performing time averaging over an N_w sample-long rectangular window. Finally, the absolute value of the result of this filtering is $r_{lm,n}$, a sequence of phase synchrony coefficients.

The phase synchrony processor (Figure 3.8) was implemented in Matlab and numerical experiments with the artificially generated signals, described earlier and shown in Figure 3.1, were performed.

The inputs of the PSP were either the high synchrony pair (Figure 3.1 (a)) or the low synchrony pair (Figure 3.1 (b)). In both cases, the sinusoidal signals were contaminated by white Gaussian noise, generated by the command “randn.” The SNR was 10 dB. For the channel containing the sinusoidal signal, Figure 3.9 depicts the instantaneous phase sequences of the signals y_n and v_n (Figure 3.7), that is, before and after narrow-band filtering (bandwidth was 0.005; the band-pass filter length was 489 samples).

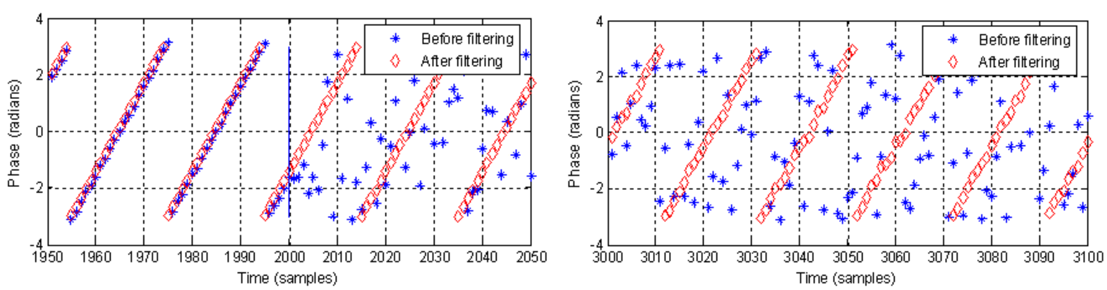

(a) (b)

Figure 3.9: Instantaneous phase sequences before and after narrow-band (B = 0.005) filtering for different time intervals: samples 1950-2050 (a) and samples 3000-3100 (b).

We observe that the filtering operation has little effect on the phase of the sinusoidal signal (to the left of the vertical line in Figure 3.9 (a)) since the center frequency of the filter and the frequency of the sinusoidal signal are the same. On the other hand, the phase of the filtered noise remains nearly linear (Figure 3.9 (a)). Even after a considerable time, the phase sequence of the filtered noise exhibits approximately linear behavior (Figure 3.8 (b)).

This effect leads to a nearly constant phase difference between two filtered random sequences (Figure 3.10 (a)). Phase relations are more complicated when processing actual time series, such as an EEG, but the general influence of the parameters is seen to be the same (Figure 3.10 (b)). Both results were obtained for a bandwidth of 0.005 and exhibit little variation in the phase differences. The latter indicates high synchrony coefficients, which for the case of Figure 3.10 (a) is known to be incorrect.

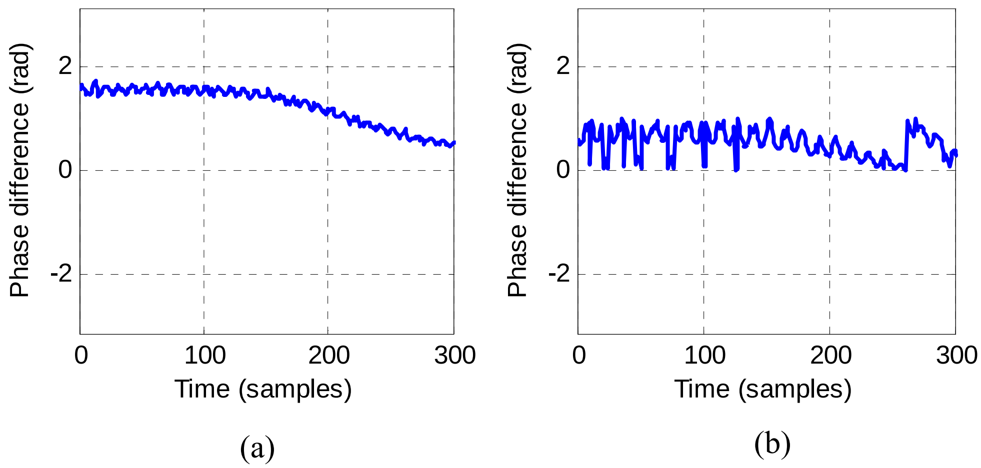

Figure 3.10: Instantaneous phase differences (a) for the low synchrony (synthetic signals) pair and (b) for the real EEG.

Considering the low synchrony signal pair (Figure 3.1 (b)), the correct value of phase synchrony is expected to be close to zero. The result of a Monte Carlo experiment [7] conducted on such pairs for varying bandwidths and lengths of analysis window is shown in Figure 3.11. Each value was obtained by averaging the results for 100 repetitions of signal pairs and statistically independent noise. The results in Figure 3.11 were obtained for the low synchrony channel pair with SNR = 10 dB. The fractional center frequency of the band-pass filter was chosen as 0.05. The length of the sinusoidal signal exceeded the length of the analysis window. The phase synchrony coefficients are represented by different colors as indicated on the color-bar.

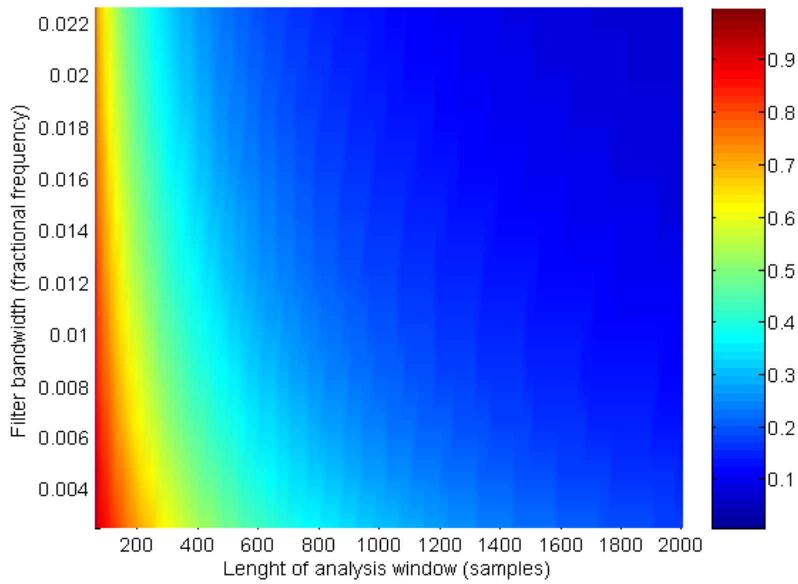

Figure 3.11: Phase synchrony for different bandwidth and different length of the analysis window; low synchrony pair.

We observe in Figure 3.11 that the bandwidth of the filter has a major effect on phase synchrony. Namely, the narrower the bandwidth, the higher the phase synchrony coefficient, and thus the higher the likelihood of phase synchrony error for the low synchrony pair. Another factor, influencing the value of phase synchrony, is the length of the analysis time window, denoted as N_w in (3.1). We observe that the shorter the analysis length, the higher the phase synchrony, and therefore the higher the likelihood of phase synchrony error for the low synchrony pair. This observation agrees with the previous theoretical derivations, presented in Section 3.1.

The corresponding results for high synchrony pairs showed a minimal dependence on bandwidth and analysis window length. All values of phase synchrony exceeded 0.99 for the entire range of filter parameters depicted in Figure 3.11.

Figure 3.12 depicts a distribution of values of phase synchrony for low and high synchrony pairs processed with 600 sample-long analysis windows, and a filter bandwidth of 0.02. Figure 3.12 was obtained for 10,000 runs with independent noise realizations with SNR = 10 dB. Only a part of the bin representing the high synchrony pair is shown in Figure 3.12 for better data representation.

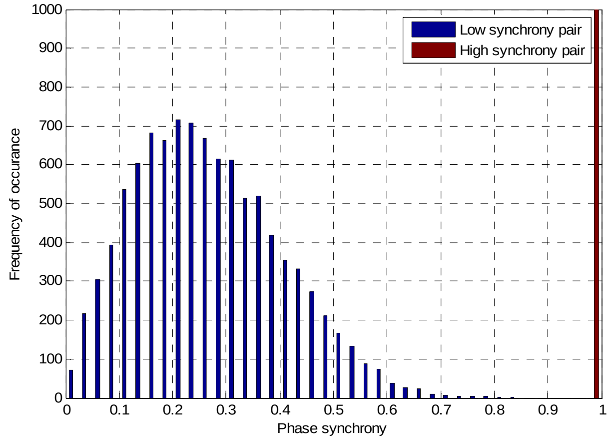

Figure 3.12: Histogram of phase synchrony for low synchrony and high synchrony signal pairs; length of analysis window is 600 samples, filter bandwidth is 0.02.

All 10,000 results corresponding to the high synchrony pair are represented by a single bin. We see in Figure 3.12 that low and high synchrony pairs can be easily discriminated by comparing a synchrony coefficient with a certain threshold chosen for a particular probability of false high synchrony detection. The distribution of PS for the low synchrony case looks like a Rayleigh distribution, whose tail is truncated at 1.

The influence of pass-band and stop-band ripples on the average value of phase synchrony was studied next. The Parks-McClellan optimal equiripple FIR was used as the pass-band filter. Stop-band and pass-band ripples were equal to 0.01. Figure 3.13 presents instantaneous phase sequences of white noise before and after narrow-band filtering with different specified pass-band and stop-band ripples. The filter bandwidth was 0.005 in fractional frequency.

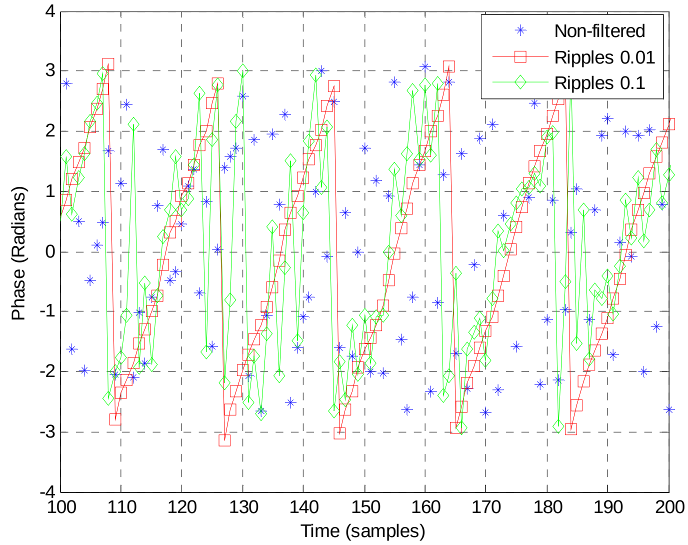

Figure 3.13: Instantaneous phase sequences of random noise, non-filtered and narrow-band filtered with different ripples; Parks-McClellan optimal equiripple FIR, $f_0 = 0.05$, pass-band is 0.005.

We see in Figure 3.13 that a filter with bigger ripples produces more variation in the instantaneous phase sequence of the filtered signal, which is desired for a random input sequence. We conclude based on the last observation that bigger ripples should produce lower values of phase synchrony for the low synchrony signal pairs. The following experiments were designed to evaluate this hypothesis.

Figure 3.14 shows the value of phase synchrony - averaged over 300 trials - for the low synchrony signal pair, seen in Figure 3.1 (b), for an analysis window length of 600 samples, different bandwidths of the filter, and various pass-band and stop-band ripples. Parks-McClellan FIR filters with the center frequency of 0.05, bandwidths from 0.0025 to 0.02, and various ripples have been used.

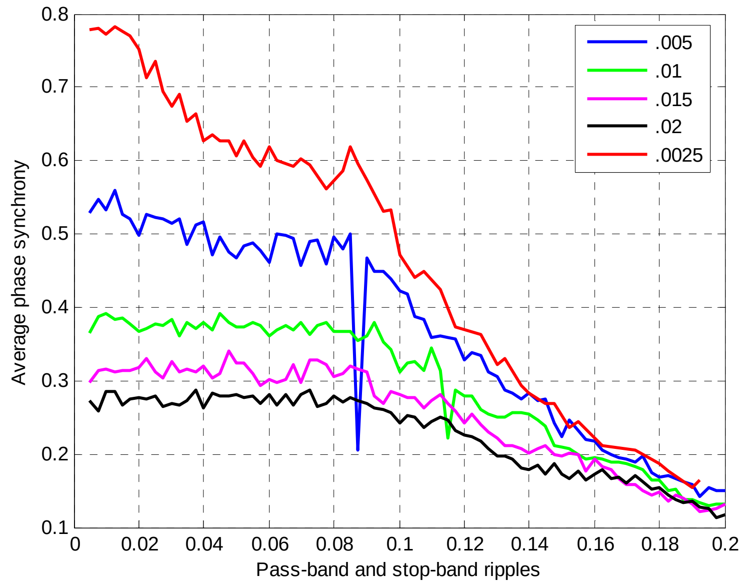

Figure 3.14: Average phase synchrony for different pass-band ripples; Parks-McClellan FIR, analysis window length of 600 samples, $f_0 = 0.05$; bandwidths are indicated in the legend.

We observe in Figure 3.14 that bigger ripples lead to lower values of phase synchrony, which is known to be correct for low synchrony pairs. This influence is more pronounced when narrow-band filters are applied. The most interesting observation is that curves for filters with different bandwidths converge to low values of phase synchrony when the ripples are around 0.2. The result for a high synchrony pair does not exhibit any dependency on the choice for pass-band and stop-band ripples. The latter observations suggest that narrowband filters can be successfully applied even when relatively big ripples are allowed.

3.3 Properties of Phase Synchrony Processor

We now describe properties of the Phase Synchrony Processor developed in Section 3.2.

An incorrectly low result for a high synchrony signal pair can be observed when processing two sinusoids of the same frequency with one of them containing a 180^0 phase shift. The corresponding result is shown in Figure 3.15, which was generated for the analysis window length of 600 samples and a bandwidth of 0.02.

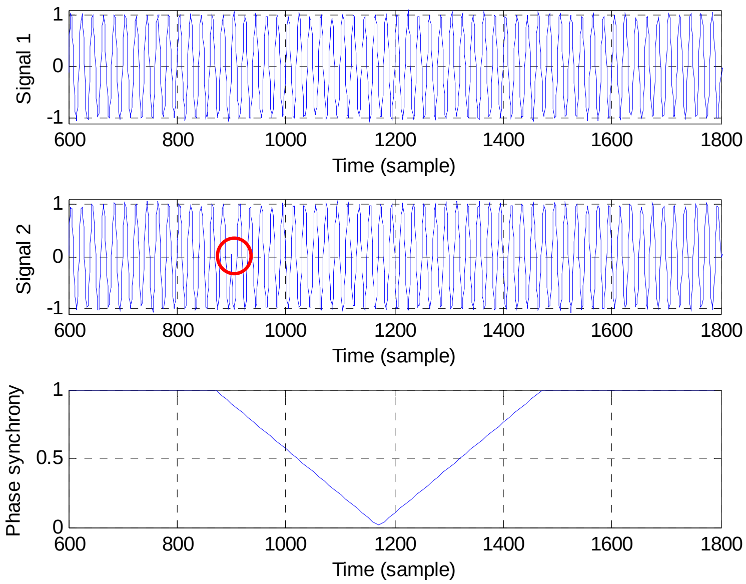

Figure 3.15: Input signals and corresponding phase synchrony computed over the sliding time window of length 600 samples, filter bandwidth of 0.02; the 180^0 phase shift is emphasized by the red circle.

Signal 1 is a plane sinusoid, while signal 2 has a phase shift of 180^0 at the 900^{th} sample. We see in the lower part of Figure 3.15 that, when the processed sinusoidal segments of different phases are equal in length, the phase synchrony is close to zero, which is known as incorrect. The described effect may be caused in the EEG, perhaps, by temporal failure of one electrode.

The next experiment was designed to discover the influence of SNR on the value of phase synchrony. The phase synchrony was estimated for the high and low synchrony signal pairs (Figure 3.1 (a) and 3.1 (b)). The length of the analysis window was 600 samples and the bandwidth of the band-pass filter was 0.02. The average over 100 trials is presented in Figure 3.16.

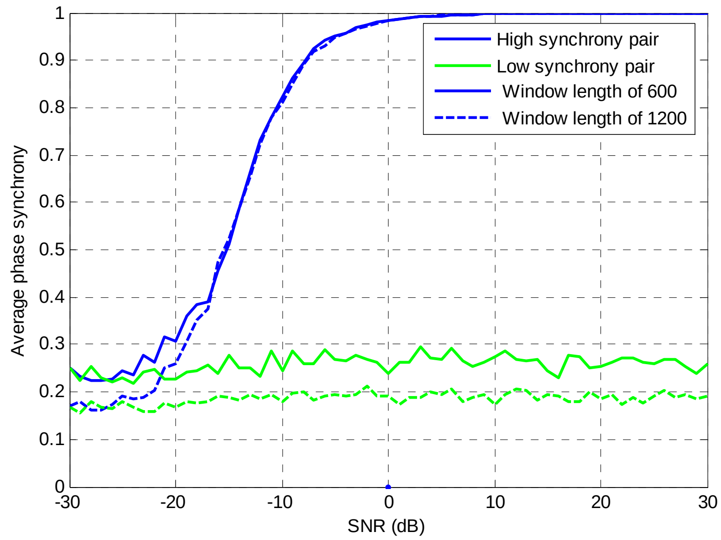

Figure 3.16: Average phase synchrony for different SNR; analysis window length is 600 samples, f_0 = 0.05, bandwidth is 0.02, ripples are 0.01.

Analysis of Figure 3.16 shows no significant changes in the value for the low synchrony signal pair. Considering the high synchrony pair, we conclude that the phase synchrony shows little dependence on the SNR when it exceeds 0 dB. High and low synchrony pairs can be successfully discriminated – on average – when SNR is bigger than -10 dB. SNR less than -20 dB leads to the same average phase synchrony as for the low synchrony case.

The other remarkable property of phase synchrony is its frequency discrimination. For a constant frequency shift $\Delta\omega = \omega_1 - \omega_2$, over the analysis time interval of N_w samples, the instantaneous phase difference can be evaluated as follows:

$$\begin{aligned} \Delta\varphi_{lm,k} &= \varphi_{l,k} - \varphi_{m,k} = \\ &= \varphi_{0l} + k\omega_l - \varphi_{0m} - k\omega_m = \\ &= \varphi_0 + k\Delta\omega \end{aligned} \tag{3.21}$$

where φ_0 is some constant initial phase difference and $\Delta\omega$ is a constant frequency difference of two signals. We will treat k as a discrete time index. Then (3.1) can be rewritten as follows:

$$r_{lm,n} = \left| \frac{1}{N_w} \sum_{k=n-N_w+1}^{n} e^{-j\varphi_0} \cdot e^{-jk\Delta\omega} \right|$$
$$= 1 \cdot \left| \frac{1}{N_w} \sum_{k=n-N_w+1}^{n} e^{-jk\Delta\omega} \right| \tag{3.22}$$

Let $n = N_w$-1, then

$$r_{lm,n} = \left| \frac{1}{N_w} \sum_{k=0}^{N_w-1} e^{-jk\Delta\omega} \right|$$
$$= \left| \frac{1}{N_w} \frac{1-e^{-jN_w\Delta\omega}}{1-e^{-j\Delta\omega}} \right|$$
$$= \left| \frac{1}{N_w} \frac{e^{-j\frac{N_w}{2}\Delta\omega}\left(e^{j\frac{N_w}{2}\Delta\omega} - e^{-j\frac{N_w}{2}\Delta\omega}\right)}{e^{-j\frac{1}{2}\Delta\omega}\left(e^{j\frac{1}{2}\Delta\omega} - e^{-j\frac{1}{2}\Delta\omega}\right)} \right| \tag{3.23}$$
$$= \left| e^{-j\frac{(N_w-1)}{2}\Delta\omega} \right| \cdot \left| \frac{1}{N_w} \frac{\sin\left(\frac{N_w}{2}\Delta\omega\right)}{\sin\left(\frac{\Delta\omega}{2}\right)} \right|$$

Since $\left| e^{-j\frac{(N_w-1)}{2}\Delta\omega} \right| = 1$,

$$r_{lm,n} = \left| \frac{1}{N_w} \frac{\sin\left(\frac{N_w}{2}\Delta\omega\right)}{\sin\left(\frac{\Delta\omega}{2}\right)} \right| = \left|\mathrm{psinc}(\Delta\omega, N_w)\right| \tag{3.24}$$

where *psinc* refers to the periodic or Dirichlet sinc function. For the sampling frequency f_s

$$\Delta\omega = \frac{2\pi\left(f_1 - f_2\right)}{f_s} \tag{3.25}$$

where f_1 and f_2 are the frequencies of the two sinusoidal signals. Note that phase synchrony equals one when $f_1 = f_2$.

Figure 3.17 presents phase synchrony between two sinusoids of different frequencies. The frequency f_1 of the first signal was fixed at 0.05, which was the center frequency of the band-pass filter. The frequency f_2 of the second signal was varying from approximately 0.035 to approximately 0.0659 Hz, which is ± 30 % of f_1. The sampling frequency was 256 Hz. The graphs were plotted for different lengths of the analysis window and filter bandwidths.

The graphs in Figure 3.17 (b) show the theoretical results, computed according to (3.24), as well as the corresponding estimates produced by the PSP.

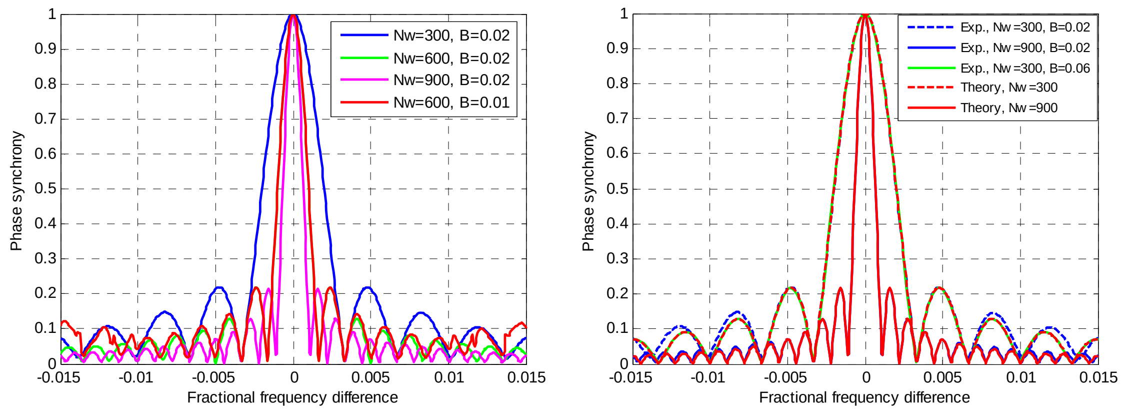

(a) (b)

Figure 3.17: Phase synchrony for a noiseless signal pair vs. frequency difference for different bandwidths and analysis window lengths; $f_1 = 0.05$: (a) experimental results and (b) comparison with theoretical results.

Figure 3.17 (a) suggests that the PSP exhibits frequency discrimination. Phase synchrony decays more rapidly when analysis is conducted with a long analysis window. The shape of this graph is not affected by the other filter parameters, such as bandwidth (Figure 3.17 (a)). Also, the phase synchrony graph corresponding to narrow-band filtering (B = 0.01) becomes less well defined when the frequency difference exceeds approximately 0.01. In the latter situation, the frequency difference is larger than the filter bandwidth (pass and transition bands); and thus the second sinusoid is attenuated. Analyzing Figure 3.17 (b), we see that the experimental data matches perfectly with the theoretical results when the frequency difference is smaller than approximately 0.005. The discrepancy between theoretical and experimental results for frequency differences exceeding 0.01 can be explained by the influence of band-pass filtering, which was not accounted for when (3.24) was derived. This discrepancy becomes less pronounced when a band-pass filter with wider bandwidth is used as illustrated by the green graph in Figure 3.17 (b) corresponding to a wider pass band of the filter (i.e. B = 0.06). Also, as seen in Figure 3.17 (b), longer analysis windows lead to better agreement between experimental and theoretical results.

Practical signals are generally contaminated by noise. We are therefore interested in determining how noise affects the frequency discrimination properties of the PSP. For this next experiment, the sinusoidal input signals were contaminated by Gaussian noise for SNR = 10 dB. The phase synchrony coefficient averaged over 100 trials is shown in Figure 3.18 (a). The frequency f_1 was fixed at 0.05; f_2 was varied over ± 30% of the f_1 range. Figure 3.18 (b) illustrates averaged PS coefficient vs. frequency difference for 300 and 900 sample-long windows for SNR = 10 dB and for the noise-free case.

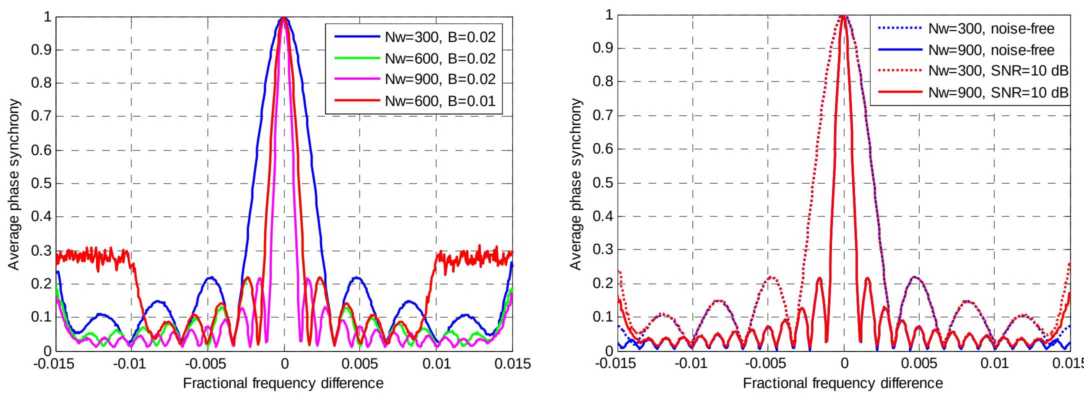

(a) (b)

Figure 3.18: Average phase synchrony for a signal pair vs. frequency difference for different bandwidths and analysis window lengths; f_1 = 0.05, SNR = 10 dB (a) and comparison with the noise-free case (b).

We see in Figure 3.18 (b) that noise contamination produces a minor influence on the average phase synchrony (i.e. minima of phase synchrony are less pronounced than in the noise-free case) when the frequency difference is small and does not exceed one half of the filter bandwidth. Considering the graph in Figure 3.18 (a) for B = 0.01, we conclude that PS is consistent with the noiseless case as illustrated in Figure 3.17 (a), when the frequency difference is smaller than approximately 0.01. PS corresponds to the average value of 0.28 for the low synchrony case when the frequency difference exceeds the filter bandwidth: pass band (± 0.005) and transition band (0.005), namely, 0.01.

Figure 3.19 illustrates average phase synchrony for the three different SNR of 10 dB, 0 dB, and -10 dB. All graphs were plotted for filter bandwidth B = 0.02 and analysis window length N_w = 300. The red graph represents average phase synchrony when only one sinusoid, namely the one at the variable frequency f_2, was contaminated by Gaussian noise. The black curve illustrates the situation when sinusoids were degraded by α-stable noise generated by a program developed by John P. Nolan [12] with the following parameters: stability α = 1, skewness β = .25, scale γ = 1, location δ = 0. Since the variance is undefined for α-stable random process, the concept of SNR is not applicable to the case of α-stable noise contamination. However, it is known [12] that, when stability α equals 2, the random process reduces to the Gaussian case with the variance $\sigma^2 = 2\gamma^2$. Therefore, SNR would be -3 dB.

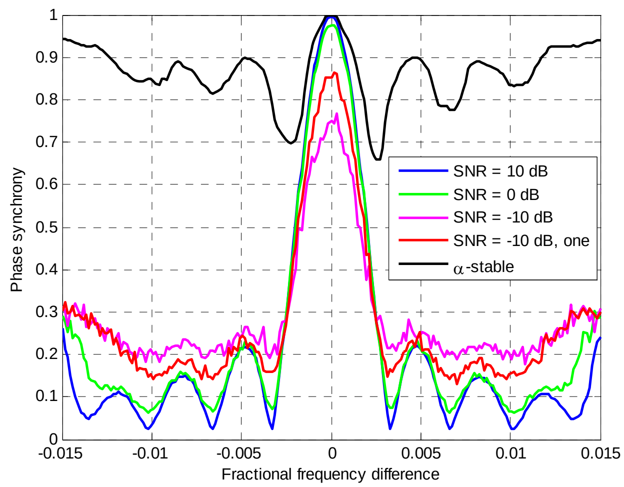

Figure 3.19: Average phase synchrony for a signal pair vs. frequency difference for different SNR; f_1 = 0.05, N_w = 300 samples, B = 0.02.

It is seen in Figure 3.19 that the increased noise power causes the dependence of phase synchrony on frequency difference to be less pronounced. However, the main lobe of the graph (when the frequency difference is relatively small) is still readily recognized. We conclude that although high intensity additive Gaussian noise affects the frequency discrimination properties of the PSP, the dependence of the phase synchrony coefficient on frequency difference is still well approximated by (3.24). Leaving one sinusoid noise-free improves frequency discrimination properties of the PSP. When sinusoids are contaminated by non-Gaussian – for instance, α-stable – noise, the frequency discrimination property of the PSP is greatly degraded. Only the shape of the graph is somewhat similar to ones when Gaussian noise was added.

We evaluate the distribution of the phase synchrony coefficient next. 10,000 phase synchrony coefficients were computed for a signal pair containing two sinusoids, with frequencies f_1 = 0.05 and f_2 = 0.052, contaminated by normal noise for SNR = 10 dB,. For the length of the analysis window N_w = 300, the expected value of the phase synchrony coefficient is approximately 0.5236. Figure 3.20 shows the estimated frequency of occurrence of phase synchrony. The Gaussian pdf computed for the estimated mean and variance – from 10,000 values of coefficients – is also plotted.

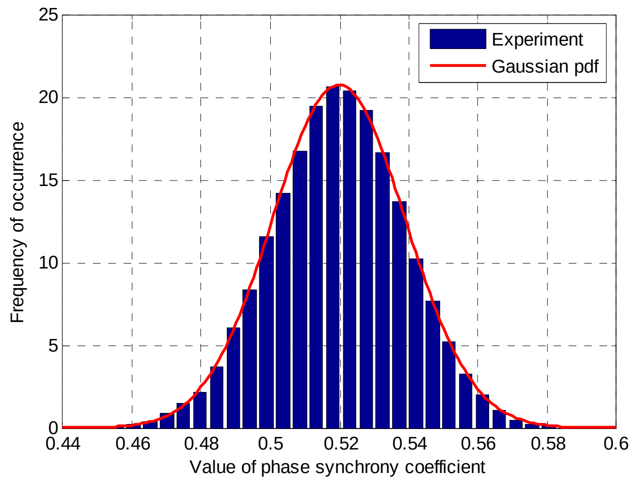

Figure 3.20: Frequency of occurrence of phase synchrony coefficient; N_w = 300, f_1 = 0.05, f_2 = 0.052, SNR = 10 dB.

We conclude from Figure 3.20 that phase synchrony (coefficient) estimates can be approximated as normally distributed when the frequency difference is relatively small.

The previously discussed results for phase synchrony coefficients were computed and averaged for independent sequences, i.e. sinusoids were contaminated by independent noise. The situation, when phase synchrony is estimated for a number of overlapping successive time windows, may be of interest. Two noisy sinusoids of length 1,000 samples were generated with f_1 = 0.05, f_2 = 0.052. Signal segments were observed and the phase synchrony was estimated over fifty successive 300 sample-long analysis windows overlapping by 290 samples (i.e. shifted by 10 samples). Figure 3.21 shows phase synchrony coefficients computed for such signal pairs for SNR = 10 dB and SNR = 0 dB. The cumulative average phase synchrony coefficients and the expected values of phase synchrony are also presented. All values are plotted vs. time instances at which the corresponding analysis time window ends.

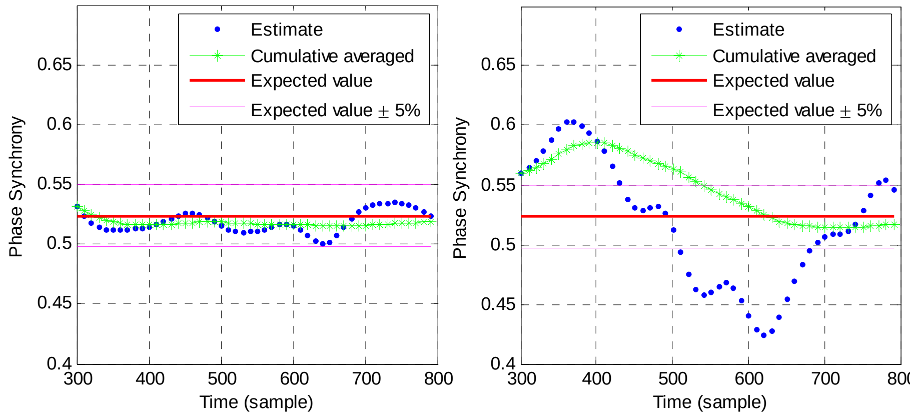

(a) (b)

Figure 3.21: Time dependence of phase synchrony for a signal pair with $f_1 = 0.05$, $f_2 = 0.052$, $N_w = 300$ samples, $B = 0.02$; (a) SNR = 10 dB and (b) SNR = 0 dB.

We see in Figure 3.21 that even when computed for dependent signal pairs, the average phase synchrony approaches its expected value relatively fast. Monte Carlo experiment showed that – for SNR of 0 dB – phase synchrony cumulatively averaged over 18 windows shifted by 10 samples (i.e. overlapping by 290 samples) is enough – on average – for the cumulative average to reach – and stay within – ±5 % the expected value. When windows were further apart, i.e. shifted by more than 10 samples, convergence occurred faster, as shown in Figure 3.22. This is expected, as the individual phase synchrony estimates are now more independent.

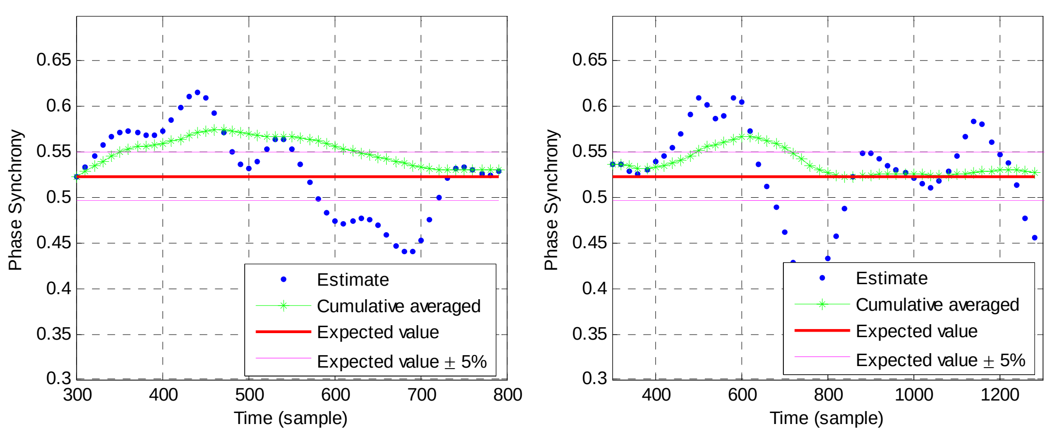

(a) (b)

Figure 3.22: Time dependence of phase synchrony for a signal pair with $f_1 = 0.05$, $f_2 = 0.052$, $N_w = 300$ samples, $B = 0.02$, SNR = 0 dB; step of (a) 10 samples and (b) 20 samples.

We suggest that the PSP may be used to estimate the frequency deviation of a sinusoidal signal contaminated by Gaussian noise relative to a noise-less standard. The phase synchrony coefficient, as evaluated by the PSP, can be compared with the expected value computed according to (3.24) for known window length and various frequency differences.

3.4 Phase synchrony analysis of EEG

In this section, we apply phase synchrony analysis to EEG records. The processor parameters will be chosen based on the previous discussions. Phase synchrony analysis is traditionally applied to discover relations in EEG between different trials, for instance, when processing event-related potentials. However, PS can be estimated within a single trial. The processing, described in the following section, corresponds to phase synchrony estimated for single-trial EEG records.

3.4.1 EEG data acquisition

Two different EEG data sets were used to test the developed processor (PSP).

One EEG data set, referred to as the "ADHD data set," was obtained from thirteen children, aged 9 to 16. Six of them were diagnosed with ADHD. None of the children had participated in neurotherapy. All participants with ADHD were reported to have had independent EEG evaluations by neurologists that showed them to be essentially free of psychopathology. All subjects were medication-free for at least 24 hours before data collection. Each child was seated comfortably in a recliner chair in a sound-attenuated room for EEG data collection. Children were shown ways to reduce muscle tension and eye movement [13].

Each experimental task was of 120 sec duration; EEG was recorded for 90 sec starting 30 sec after the beginning of task performance. Tasks included: (a) solving simple addition and subtraction problems presented in columns by marking which were correct or incorrect, and (b) reading silently to themselves an age/intellectual ability appropriate story. The children appeared to show minimal movement during data acquisition.

A Lexicor Medical Technology (Boulder, Colorado) Neurosearch-24 system (NRS-24) was employed for EEG acquisition. Using a lycra electrode cap, referential (A1, A2) recordings were obtained from 19 sites placed according to the International 10-20 system. Resistance was kept below 5000 ohms with no more than 500 ohms between neighboring electrodes. EEG was amplified using the NRS-24 (gain setting 32K in the 0.5 - 64 Hz band, with a 60 Hz notch filter), sampled at 256 Hz, and band-pass filtered from 2 to 64 Hz.

The other EEG data set, referred to as the "Condition data set", was obtained from forty strongly right-handed college students (18 men, 22 women; 17 – 21 years old, mean age of 18.87). They were recruited from 613 online survey participants who had been administered the Schizotypal Personality Questionnaire (SPQ; by Raine) [14], and smoking history and medical background questionnaires. They reported normal hearing, no known history of neurological or psychiatric problems and no prescription (except birth control) or over-the-counter drugs, alcohol or illicit drugs for at least one day before the experiment. Participants were chosen based upon scoring in the upper or lower 1/3 of the Raine's SPQ [14] (upper cutoff 25, lower cutoff 13), low schizotypy (N_p = 20: 10 smokers and 10 non-smokers; SPQ M = 3.53, SD = 3.08) and high schizotypy (N_p = 20: 10 smokers and 10 non-smokers; SPQ M = 40.05, SD = 9.47)[1]. Smokers abstained for at least four hours before the experiment.

Forty identical pairs of 1 ms 1000 Hz sinusoidal tone pips (1ms rise/fall; 70dB), with a 512 ms inter-click interval and 10 s inter-pair interval, were delivered by the Neuroscan® stimulus generation system through speakers placed 35 cm from each ear. Participants were instructed to attend to a stationary picture of a white cross on a computer monitor screen at eye level, 80 cm in front of them. EEG data was collected for two participant conditions: eyes open and eyes closed.

Continuous EEG (0.1 to 100 Hz, 500 Hz sampling rate; gain of 150) was recorded with a cap (Electrocap Inc.) at 30 electrode sites (impedance < 5 kΩ), referenced to the

[1] M and SD represent mean and standard deviation of the SPQ test scores.

nose, plus vertical (above and below left eye) and horizontal Electro-oculogram[2] (EOG) electrodes. Recording and digitization was done with Neuroscan® SynAmps amplifier and Scan® version 4.2 software [15].

3.4.2 General properties of Phase Synchrony observed on real EEG records

We present examples of phase synchrony evaluated for the EEG record collected from a healthy subject performing a reading task from the "ADHD data set." The EEG signal was sampled at the rate of 256 Hz and then processed according to (3.1) using band-pass filters with center frequency f_0 = 10 Hz and bandwidth of either 0.02 or 0.0025, i.e. 4 Hz or 0.5 Hz respectively. The length of the analysis window was 600 samples. The results for one time frame for all 19 electrode pairs are shown in Figure 3.23. Each square in Figure 3.23 corresponds to a phase synchrony coefficient evaluated for the particular pair of electrodes. Note that the diagonal elements are one since auto-synchrony of a signal pair is always identical to one.

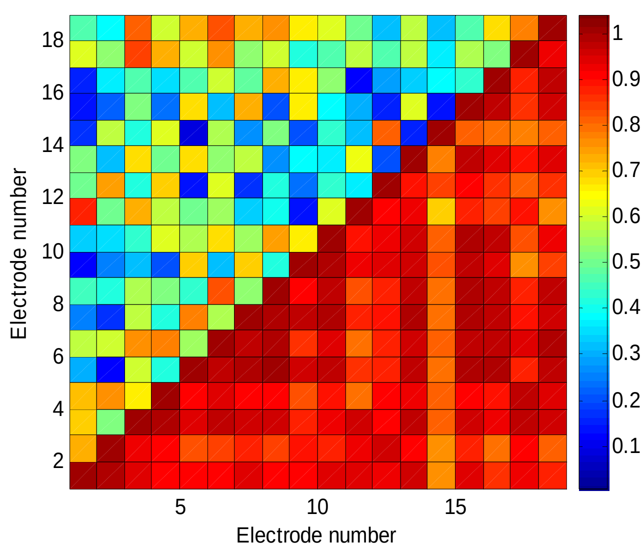

Figure 3.23: Phase synchrony between different pairs of EEG electrodes; f_0 = 10 Hz (0.039 in fractional frequency), N_w = 600 samples, bandwidth 0.02 (upper triangle) and 0.0025 (lower triangle).

[2] electrical activity associated with eye movement

The center frequency and the bandwidths of the filter were chosen to correspond to the α rhythm (8-12 Hz). As seen in Figure 3.23, a narrow bandwidth (lower triangle) tends to produce high values of phase synchrony. In our modeled results we observed that this can happen regardless of whether synchrony is actually low or high.

Figure 3.24 illustrates the importance of an appropriate choice of pass-band ripple, showing the phase difference between the EEG electrodes F_{p1} and F_3 using a Parks-McClellan FIR filter with a fixed bandwidth of 0.005 and different ripples.

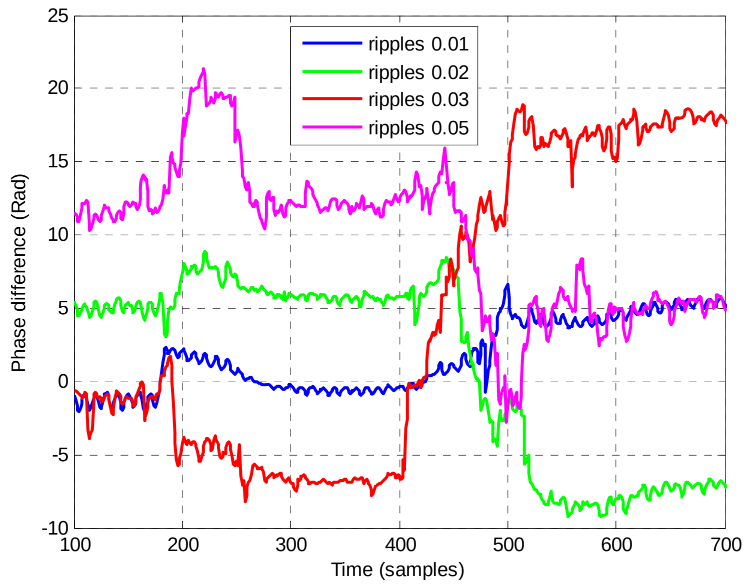

Figure 3.24: Instantaneous phase difference between F_{p1} and F_3 for various pass-band and stop-band ripples; analysis window length 600 samples, f_0 = (0.05), bandwidth 0.005; real EEG record.

Analysis of Figure 3.24 suggests that when the ripples of the band-pass filter are small, the phase difference may locally exhibit almost sinusoidal behavior, while this effect becomes less noticeable when bigger ripples are allowed. Since there are no obvious reasons for such behavior, we suggest that this result is undesirable and thus the use of bigger pass-band ripples is preferable.

To be able to discriminate between low and high synchrony, these results suggest that band-pass filters with sufficiently broad bandwidth and analysis windows that are sufficiently long need to be used. For instance, studying the EEG α rhythm (8 – 12 Hz), the center frequency of the band-pass filter would be 10 Hz and the bandwidth 0.02. Thus, as seen in Figure 3.11, to obtain a phase synchrony coefficient under 0.2 (on average) for a low synchrony signal pair, the length of the analysis window must be over 600 samples. Assuming a sampling rate of 256 Hz, we see that EEG frames longer than 2 seconds need to be processed. If less discrimination is acceptable, and a phase synchrony coefficient under 0.4 (on average) is used, the analysis frame needs to be over 240 samples long (about 1 second).

For EEG data collected from $L+1$ electrodes, $L^2/2 - L$ unique phase synchrony coefficients r_{lm}, can be estimated for all possible pairs of electrodes l and m. These coefficients computed over the N_w-sample time window, need to be interpreted. To make this interpretation more straight-forward, an appropriate method of mapping of the PS coefficients is important.

The most frequently used method to display these values of phase synchrony on the conventional electrode placement map is by drawing lines connecting two electrodes, for which phase synchrony exceeds some threshold [10], [11]. This method is schematically illustrated in Figure 3.25 for electrode F_3.

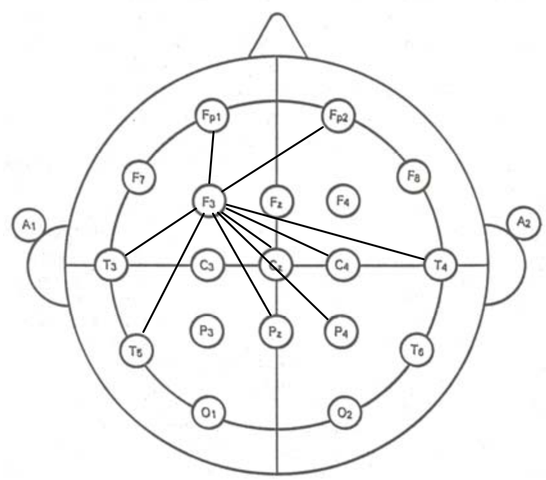

Figure 3.25: Example of mapping of phase synchrony coefficients exceeding a threshold for electrode F_3.

An advantage of this approach is its capability to qualitatively display high synchrony coefficients for particular electrode pairs. A weakness is its inability to quantitatively represent the synchronization data. The only available information about the value of the coefficient from Figure 3.25 is whether it exceeds the threshold or not. Also, keeping in mind that such mapping is usually done for all electrodes on the same plot, this method faces a challenging trade-off between complexity and completeness of representation. An increase in the threshold may lead to omitting some important data, while it would certainly simplify the map and make its interpretation more straight-forward as it is easier to track fewer crossing lines.

Another approach to mapping the synchronization data has been proposed by Allefeld and Kurths [3], [4]. The main idea was to assign oscillators to clusters in which they participate with different weights and form a multivariate synchrony coefficient for each electrode. Based on this, each oscillator contributes to the particular clusters.

The approach, employed here, can be viewed as a variation of the Allefeld and Kurths concept. All electrodes may be included into a single cluster with unitary weights. Thus, no influence of the electrode spacing comes into consideration. To take this spacing into account, individual clusters for each electrode were formed based on the distance between the analyzed electrode and all other electrodes. The oscillators can be assigned to form clusters, for instance, of local and non-local synchrony as shown in Figure 3.26.

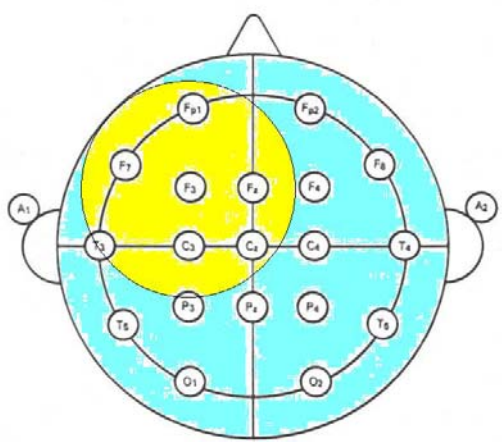

Figure 3.26: Example of two clusters assigned for the electrode F_3: local (yellow) and non-local (blue) synchrony.

Thus, the multivariate phase synchrony coefficient for the i^{th} electrode is computed as follows:

$$P_i = \frac{1}{M}\sum_{k=1}^{M} r_{ik} \tag{3.26}$$

where r_{ik} are phase synchrony coefficients between the i^{th} oscillator and the k^{th} oscillator, where k refers to one of the M other oscillators included in cluster i, i.e. the cluster associated with electrode i.

Utilizing this approach, the following steps have been performed:

1. use the data to estimate phase synchrony coefficients r_{ik} for all possible electrode pairs as in (3.1);
2. establish clusters for short range and long range synchrony for all electrodes;
3. evaluate multivariate phase synchrony coefficients P_i for all electrodes and clusters as in (3.26);
4. map the multivariate phase synchrony coefficients P_i on a topographical plot of a human brain.

An example of a result obtained from the kind of processing just described is shown in Figure 3.27. The multivariate phase synchrony coefficients for 19 electrodes have been mapped on the plot of a human brain using the Matlab routine "*eegplot*" developed by Icaro and freely distributed from the Mathworks web site http://www.mathworks.com/. The positions of the electrodes in Figure 3.27 are indicated by the black dots. The values of the coefficients are represented by colors. Dark blue corresponds to zero, dark red represents one, intermediate values are shown by other colors as indicated on the color-bar. The actual data was available only for the points on the map where the electrodes were placed. For illustrative purposes, we assume the distribution of phase synchrony coefficients to be smooth on the brain surface. Based on this, cubic interpolation was used to estimate values of the multivariate phase synchrony coefficients for the locations between the electrodes [3], [4]. The center frequency of the filter was 5.5 Hz, the bandwidth was 0.055 Hz, and the length of the analysis time window was 300 samples, as discussed above.

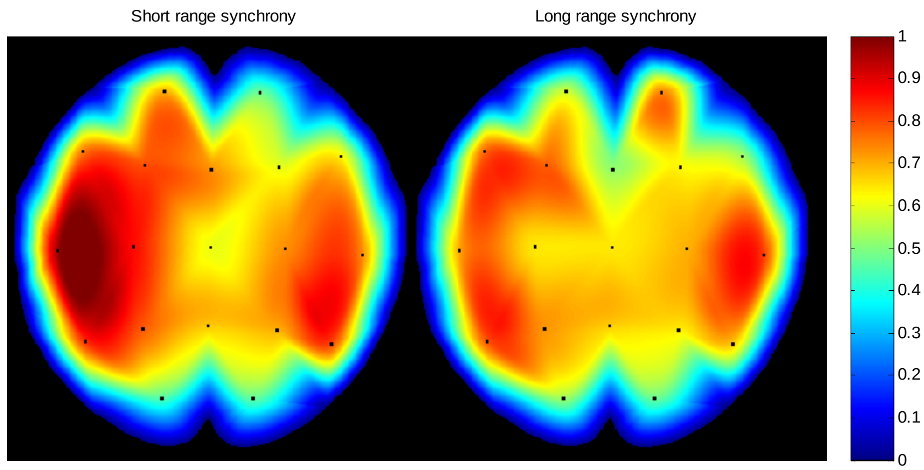

Figure 3.27: Multivariate phase synchrony coefficients mapped on a topographical plot of the human brain.

The next step in the processing could be the evaluation of a sequence of such multivariate synchrony maps computed over consecutive and overlapping time windows. This approach can provide a tool to study phase synchrony dynamics.

3.4.3 Discrimination between ADHD and non-ADHD children

The EEG data from the "ADHD data set" corresponding to "Math" and "Reading" tasks [13] was processed by the Phase Synchrony Processor (PSP), which estimates phase synchrony coefficients $r_{lm,n}$ for the pair of electrodes l and m over an N_w sample long time window as discussed in Section 3.2.

Phase synchrony was computed based on (3.1) for all individuals for the following frequency bands (rhythms): δ (0-3 Hz), θ (4-7 Hz), α (8-12 Hz), β_1 (13-20 Hz), β_2 (20-30 Hz), γ_1 (30-40 Hz), and γ_2 (40-50 Hz). To conduct the processing in the frequency band of interest, the Parks-McClellan FIR band-pass filter with a pass-band corresponding to the EEG rhythm has been employed. For instance, for the γ_1 rhythm, the pass-band was selected from 30 to 40 Hz. For all rhythms, transition bands of 2 Hz, and pass-band and stop-band ripples of 0.02 were selected. The length of the analysis time window N_w was chosen as 600 samples (approximately 2.3 seconds considering the sampling frequency f_s = 256 Hz) to decrease finite window length effects as discussed in Section 3.2.

Using l^{th} electrode as a reference, phase synchrony was estimated for the i^{th} subject and for n^{th} time interval for all other electrodes (pairs) to form a vector of individual phase synchrony $\mathbf{x}_{i,n}$, specified for the l^{th} reference electrode as follows:

$$\mathbf{x_{i,n}} = \left(r^{i}_{l1,n} \quad \ldots \quad r^{i}_{lN_e,n} \right)^t \tag{3.27}$$

where N_e represents the number of electrodes used. Note that auto phase synchrony (i.e. the phase synchrony coefficients evaluated between an electrode and itself) were not considered for processing since they always equal one.

These vectors were computed for each subject for each of N = 400 consecutive time intervals, shifted by 50 samples (i.e. overlapping by 550 samples). The estimates were averaged within two groups of participants (i.e. smokers vs. nonsmokers, high vs. low schizotypy, eyes open vs. eyes closed) to determine the vectors of average group synchrony as

$$\overline{\mathbf{x}}_{\mathbf{k}} = \frac{1}{N \cdot N_k} \sum_{i=1}^{N_k} \sum_{n=1}^{N} \mathbf{x_{i,n}} \tag{3.28}$$

where $\mathbf{x_{i,n}}$ are the vectors of individual phase synchrony used to form the k^{th} cluster (group), N is the number of time windows or frames used to evaluate phase synchrony for each subject, and N_k is the size of the k^{th} cluster. Thus, having 6 or 7 participants in a group, these vectors of average phase synchrony were computed based on either 2,400 or 2,800 individual phase synchrony vectors. The standard deviation of phase synchrony was evaluated for all electrode pairs within each group also:

$$\sigma_k = \sqrt{\frac{1}{N \cdot N_k} \sum_{i=1}^{N_k} \sum_{n=1}^{N} \left(\mathbf{x_{i,n}} - \overline{\mathbf{x}}_{\mathbf{k}} \right)^2} \tag{3.29}$$

Figure 3.28 illustrates the algorithm of evaluating average group phase synchrony from the EEG records.

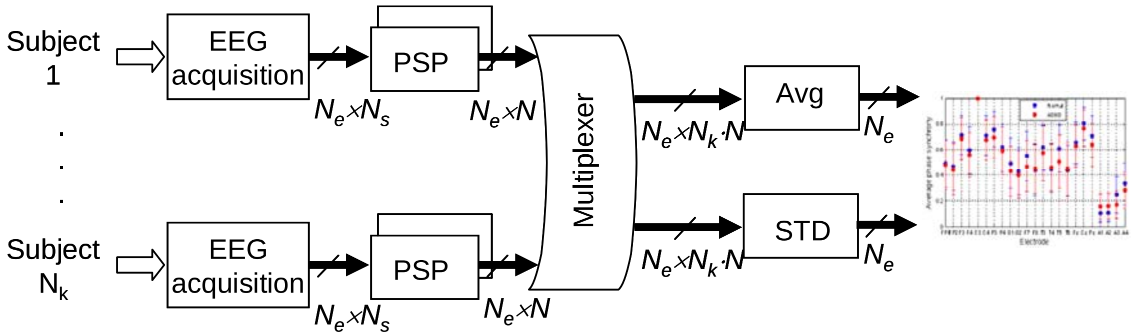

Figure 3.28: Block diagram of evaluating averaged - within group and over time - phase synchrony.

When the averaged phase synchronies were different for two groups, Euclidean and Mahalanobis distance-based classifiers [18] were used to discriminate between these groups. If no differences in average group synchrony were observed, no classification was performed. The Euclidean and Mahalanobis distances between two vectors $\mathbf{x_{i,n}}$ and $\overline{\mathbf{x}}_\mathbf{k}$ are specified as

$$d_{i,k} = \left\| \mathbf{x_{i,n}} - \overline{\mathbf{x}}_\mathbf{k} \right\|_Q = \sqrt{\left(\mathbf{x_{i,n}} - \overline{\mathbf{x}}_\mathbf{k} \right)^H \mathbf{Q_k} \left(\mathbf{x_{i,n}} - \overline{\mathbf{x}}_\mathbf{k} \right)} \tag{3.30}$$

In the case considered here, $\mathbf{x_{i,n}}$ is the vector of phase synchrony coefficients evaluated for the i^{th} subject (individual phase synchrony) specified by (3.27), and $\overline{\mathbf{x}}_k$ is the within-group average vector of phase synchrony for the k^{th} group (group phase synchrony) computed according to (3.28). Thus, (3.30) can be viewed as a measure of association of the i^{th} individual with the k^{th} group. As discrimination was performed between two groups, k takes on the values 1 and 2.

$\mathbf{Q_k}$ are weighting matrices. For the Euclidean distance, $\mathbf{Q_k}$ are identity matrices. For the weighted Euclidean distance, $\mathbf{Q_k}$ are diagonal matrices with elements equal to the inverse of the variances estimated for the k^{th} group. For the Mahalanobis distance, $\mathbf{Q_k}$ are the inverse covariance matrices [17]. For the finite data set, the inverse covariance matrices were estimated as

$$\hat{\mathbf{Q}}_\mathbf{k} = \left[\frac{1}{N_k - 1} \mathbf{X_i} \mathbf{X_i}^\mathbf{T} \right]^{-1} \tag{3.31}$$

where $\mathbf{X_i}$ is a matrix of all N times N_k column-vectors of individual phase synchronies with the means subtracted:

$$\mathbf{X_i} = \left[\mathbf{x_{1,1}} - \bar{\mathbf{x}}_\mathbf{k}, \ldots, \mathbf{x_{i,1}} - \bar{\mathbf{x}}_\mathbf{k}, \ldots \mathbf{x}_{\mathbf{N_k},\mathbf{N}} - \bar{\mathbf{x}}_\mathbf{k} \right] \quad (3.32)$$

Mahalanobis distances were evaluated according to (3.30) with weighting matrices $\hat{\mathbf{Q}}_\mathbf{k}$ evaluated according to (3.31). Euclidean, weighted Euclidean, and Mahalanobis distances were computed between vectors of individual phase synchrony $\mathbf{x_{i,n}}$ and two vectors of group synchrony $\bar{\mathbf{x}}_\mathbf{1}$ and $\bar{\mathbf{x}}_\mathbf{2}$. The vectors of individual phase synchrony $\mathbf{x_{i,n}}$ were excluded from the group synchrony vectors $\bar{\mathbf{x}}_\mathbf{1}$ and $\bar{\mathbf{x}}_\mathbf{2}$. The i^{th} individual was assigned to group one if $d_{i,1} < d_{i,2}$. Otherwise, he/she was assigned to group two.

Classifiers employing (3.30) implement a linear discriminant function [18]. It might be beneficial to employ a nonlinear – quadratic, for instance – discriminant function. Assuming normal distributions, minimum error-rate classification can be achieved when the discriminant function is designed as follows [18]:

$$g_{i,k} = -\frac{1}{2}\left(\mathbf{x_{i,n}} - \bar{\mathbf{x}}_\mathbf{k}\right)^H \hat{\mathbf{Q}}_\mathbf{k} \left(\mathbf{x_{i,n}} - \bar{\mathbf{x}}_\mathbf{k}\right) - \frac{1}{2}\ln\left|\hat{\mathbf{Q}}_\mathbf{k}^{-1}\right| + \ln\left[P(\omega_k)\right] \quad (3.33)$$

where $P(\omega_k)$ is the a-priori probability of class k. In the case considered here both classes are equally probable, and thus $P(\omega_1) = P(\omega_2) = 0.5$. The subject is therefore assigned to the group with the higher discriminant function.

The other classifier tested implements the "nearest neighbor" Vector Quantizer (VQ) as described by Namburu [19]. Instead of evaluating vectors of group synchrony, the Euclidean distance was computed between the test vector of individual synchrony and all vectors of individual synchrony assigned to the training data set. The individual was assigned to the first group if the minimum Euclidean distance was found between the vector of his/her phase synchrony and one of the training vectors belonging to the first group. Otherwise, he/she was assigned to group two.

During classification, one subject was excluded from the group and N = 400 vectors of his/her individual phase synchrony were used as $\mathbf{x_{i,n}}$ in (3.30) to test the classifier. The remaining vectors of individual phase synchrony (400 for each subject) were used to train the classifier, i.e. to form data matrices as in (3.32) and to evaluate group synchronies as in (3.28) and weighting matrices as in (3.31). The percentage of correct associations was evaluated.

We observed that phase synchrony is significantly lower for one particular non-ADHD subject than for all other non-ADHD participants, as illustrated in Figure 3.29 for θ and β_1 rhythms.

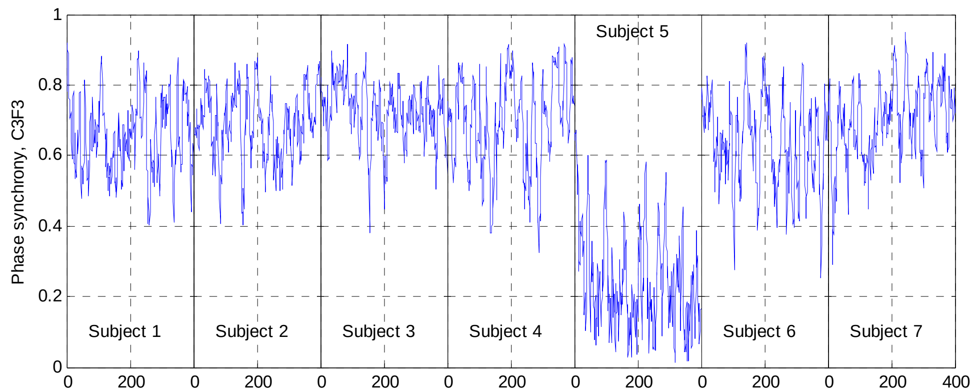

(a)

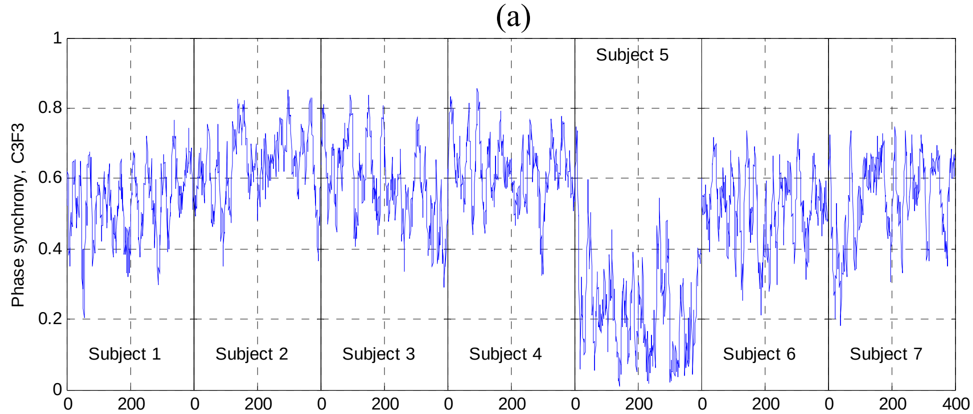

(b)

Figure 3.29: (a) θ and (b) β_1 rhythm phase synchrony between C_3 and F_3 electrodes evaluated for the "Math" task for all non-ADHD participants.

We see in Figure 3.29 that phase synchrony varies in time for each participant and between participants. However, phase synchrony is significantly different on average between Subject 5 and all other subjects forming the Non-ADHD group. Similar effects were observed for the same individual for different electrode pairs and for all assessed frequency bands. We consider phase synchrony of this subject to be inconsistent with all other subjects and therefore this participant was excluded from the processing.

Group phase synchronies $\bar{\mathbf{x}}_{\mathbf{k}}$ as averaged within each of two groups and over time according to (3.28) are presented for the δ, θ, α, β_1, β_2, γ_1, and γ_2 rhythms in Figures 3.30-3.36 for reference C_3 as explained early in this Section and specified in (3.27). The bars indicate one standard deviation ($\pm\sigma$) intervals according to (3.29).

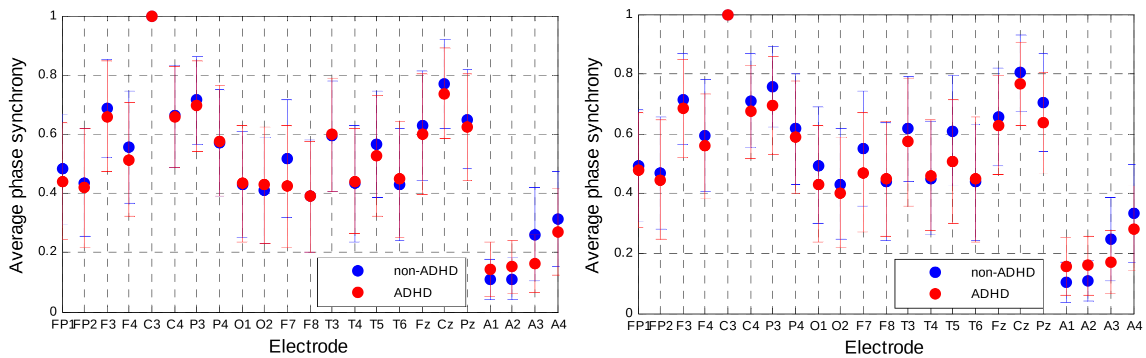

(a) (b)

Figure 3.30: Average δ rhythm (0-3 Hz) phase synchrony: (a) reading and (b) math tasks.

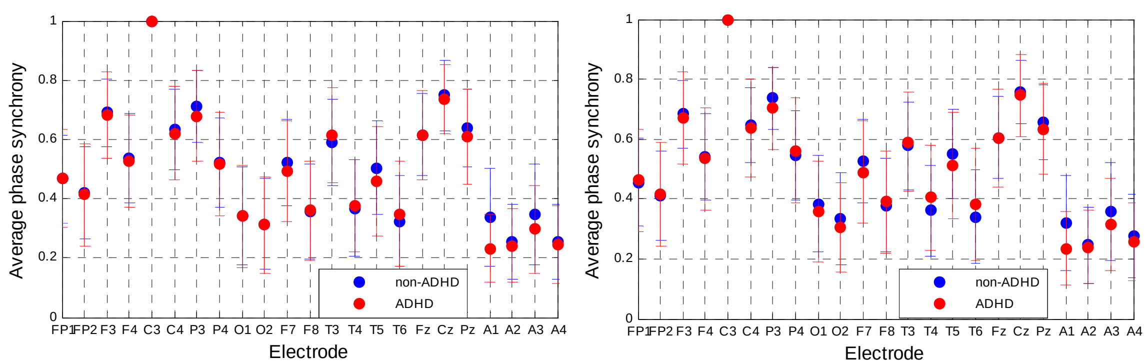

(a) (b)

Figure 3.31: Average θ rhythm (4-7 Hz) phase synchrony: (a) reading and (b) math tasks.

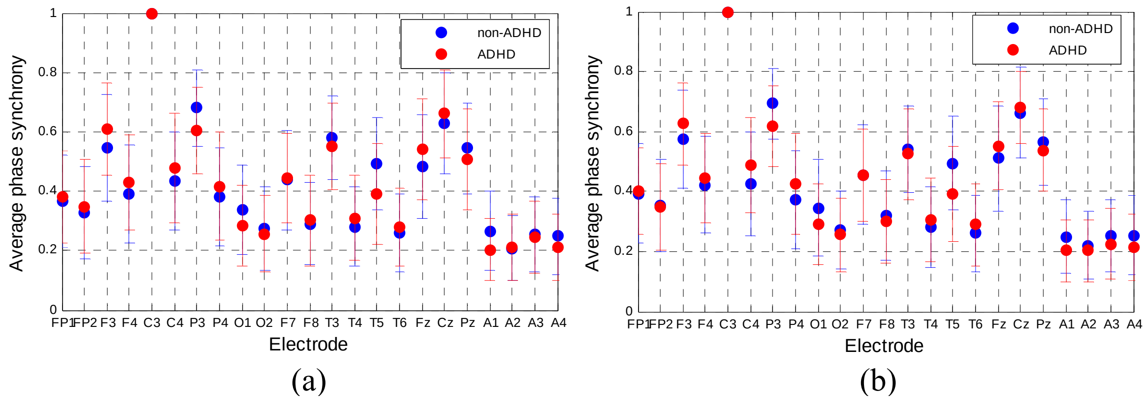

Figure 3.32: Average α rhythm (8-12 Hz) phase synchrony: (a) reading and (b) math tasks.

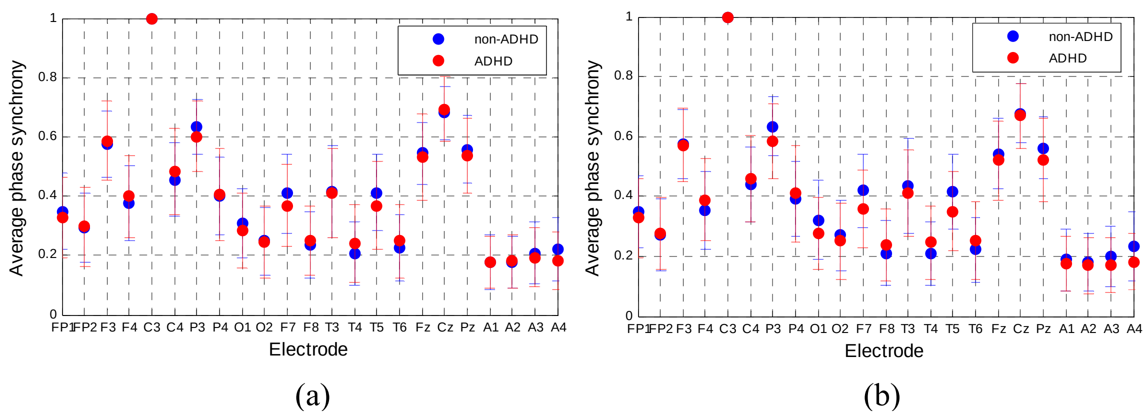

Figure 3.33: Average β_1 rhythm (13-20 Hz) phase synchrony: (a) reading and (b) math tasks.

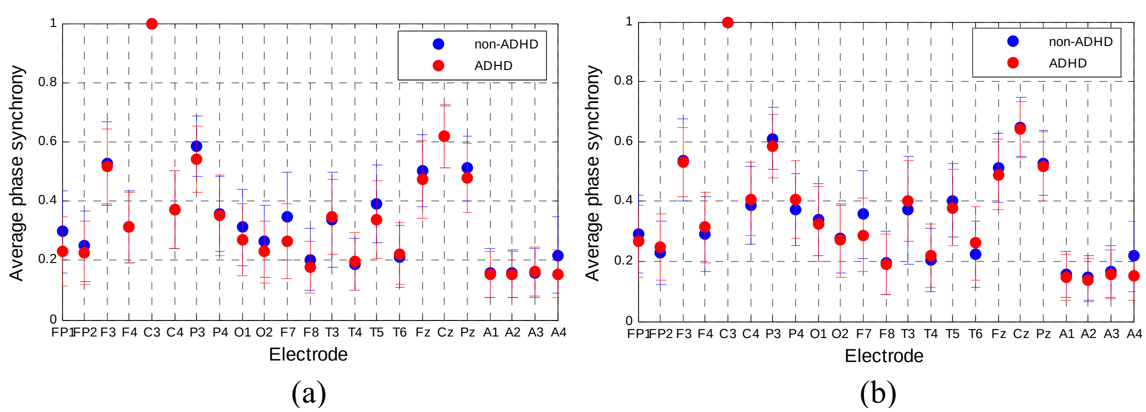

Figure 3.34: Average β_2 rhythm (20-30 Hz) phase synchrony: (a) reading and (b) math tasks.

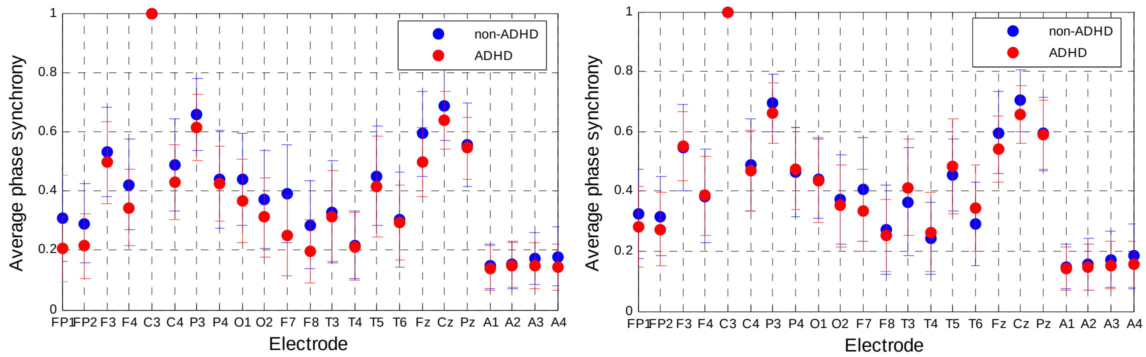

(a) (b)

Figure 3.35: Average γ_1 rhythm (30-40 Hz) phase synchrony: (a) reading and (b) math tasks.

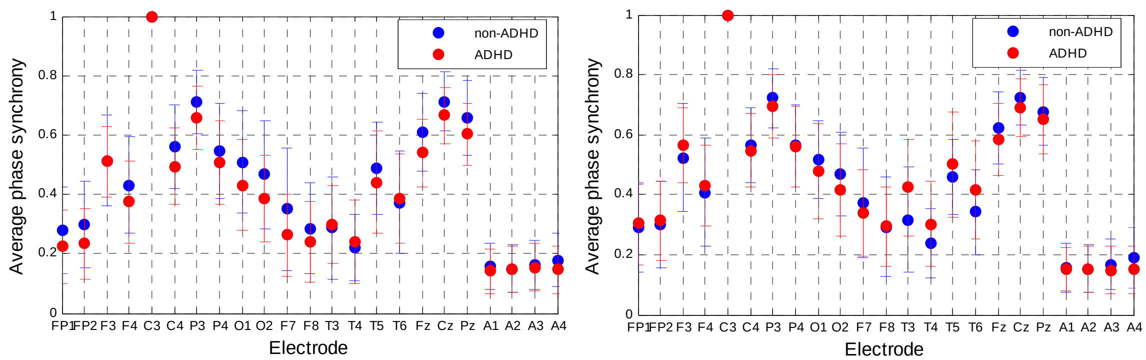

(a) (b)

Figure 3.36: Average γ_2 rhythm (40-50 Hz) phase synchrony: (a) reading and (b) math tasks.

We see in Figures 3.30-3.36 that phase synchrony is higher – on average – for non-ADHD participants than for ADHD subjects for many electrode pairs. This difference is more pronounced for particular electrode pairs in each rhythm. For instance, in the δ rhythm and the "Math" task (Figure 3.30 (b)), such an electrode pair is C_3T_5; for both β rhythms (Figure 3.34 and Figure 3.34) it is C_3F_7; and for the γ_1 rhythm (Figure 3.35) most diversity is offered by C_3F_{p1} and C_3F_7. This observation suggests using only particular electrode pairs (electrode masking), thereby offering higher discrimination power in classification. Two electrode masking algorithms were considered: "Maximum masking" when a number of electrode pairs with maximum differences in phase synchrony was used, and "Area masking" when electrode pairs forming particular areas (clusters) were used. "Maximum masking" was performed with various numbers of electrode pairs included. As an example of "Area masking," phase synchrony from the frontal lobe (i.e. for the electrode pairs C_3F_{p1}, C_3F_{p2}, C_3F_3, C_3F_4, C_3F_7, C_3F_8, and C_3C_4) were included in processing.

We also see in Figures 3.30-3.36 that the differences in average phase synchrony are more pronounced for particular rhythms and tasks.

Euclidean, weighted Euclidean, and Mahalanobis distance-based classification were implemented. Quadratic and Vector Quantizer-based classifiers were tested also. Only Euclidean distance-based classifier produced results with approximately equal error probability when tested on non-ADHD and ADHD subjects. Therefore, only the Euclidean distance-based classifier was considered. The highest performance of the classifier was observed for the "Math" task in the δ rhythm when "Maximum masking" with 9 electrode pairs was implemented and for the "Reading" task in the γ_1 rhythm with "Area masking." This observation is consistent with the results depicted in Figure 3.30 (b) and in Figure 3.35 (a), where differences between the average phase synchronies of the two groups seem to be more pronounced than for other rhythms and tasks. The corresponding percentages of correct classification are presented in Figure 3.37.

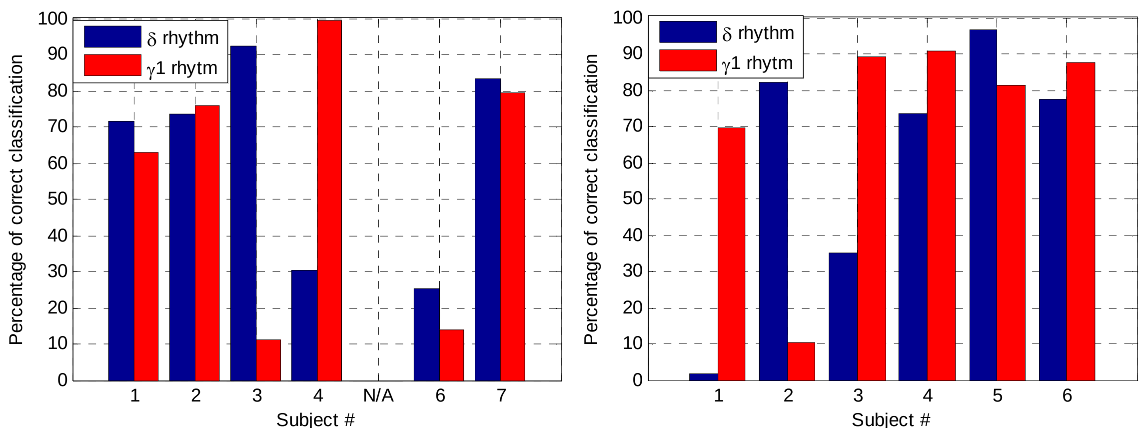

(a) (b)

Figure 3.37: Individual classification scores for Euclidean classifier using reference C_3: δ rhythm (0-3 Hz), "Math" task, "Maximum masking" with 9 electrode pairs and γ_1 rhythm (30-40 Hz), "Reading" task, frontal lobe for (a) the non-ADHD group and (b) the ADHD group.

Analyzing Figure 3.37, we can conclude that the classifier performance varies greatly for different choices of rhythm and task for some subjects. We may conclude from Figure 3.37 that, when classification was performed for the δ rhythm, The average percentage of correct classification using the δ rhythm is 62.7 % for the non-ADHD group and 61.3 %, for the ADHD group. For the γ_1 rhythm, these percentages are 57.3 % and 71.5 % for non-ADHD and ADHD participants respectively. The average percentage of correct classification, over these two rhythms and all subjects in both test groups is, 63.2 %.

We also observed that proper electrode masking can – in general – improve performance of the classifier. For instance, considering Figure 3.35 (a), we conclude that the electrode pairs placed near the frontal lobe, namely C_3F_{p1}, C_3F_{p2}, C_3F_3, C_3F_4, C_3F_7, C_3F_8, and C_3C_4, may contribute to better classification. The classification results depicted in Figure 3.38 support the latter conclusion.

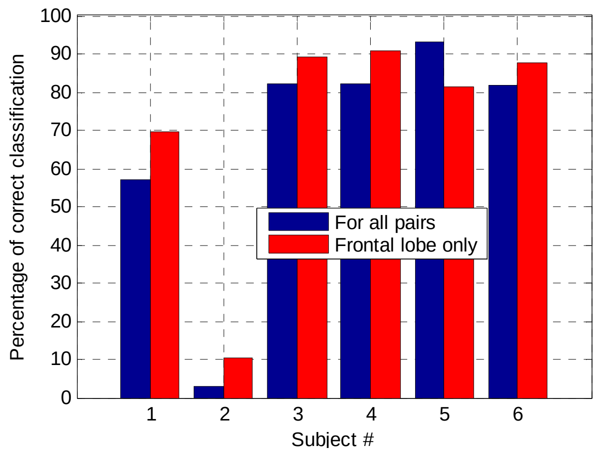

Figure 3.38: Individual classification scores for Euclidean classifier tested on ADHD participants for γ_1 rhythm (30-40 Hz) using reference C_3; "Reading" task, all available electrode pairs and the frontal lobe only.

We see in Figure 3.38 that masking (i.e. "Area masking" as depicted in Figure 3.38) – in general – tends to improve the performance of the classifier in that it increases the percentage of correct classifications. These results were observed on limited experimental data; perhaps, a bigger data sample would more conclusively show such an improvement in performance of the classifier.

Figure 3.39 shows the distribution of phase synchrony for two electrode pairs C_3F_{p1} and C_3F_8 for the γ_1 rhythm "Reading" task for all participants considered.

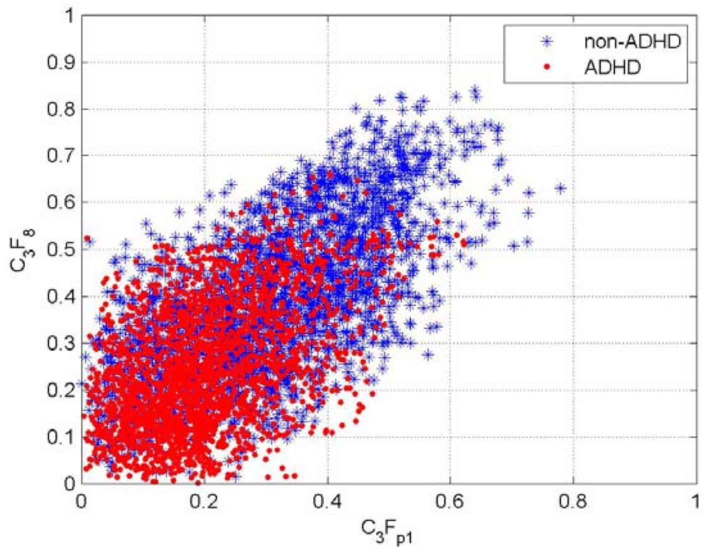

Figure 3.39: Phase synchrony for electrode pairs C_3F_{p1} and C_3F_8 for the γ_1 rhythm “Reading”.

We see in Figure 3.39 that values of phase synchrony form two overlapping clusters for two groups of participants. We can estimate that the centroid of the blue – non-ADHD – cluster is located at approximately 0.4 when the centroid of the red – ADHD – cluster is considerably lower, between 0.2 and 0.3. Figure 3.40 illustrates the situation when two of the ADHD subjects (Subject 1 in Figure 3.40 (a) and Subject 2 in Figure 3.40 (b)) were taken out of the ADHD group and their individual phase synchronies indicated in a different color.

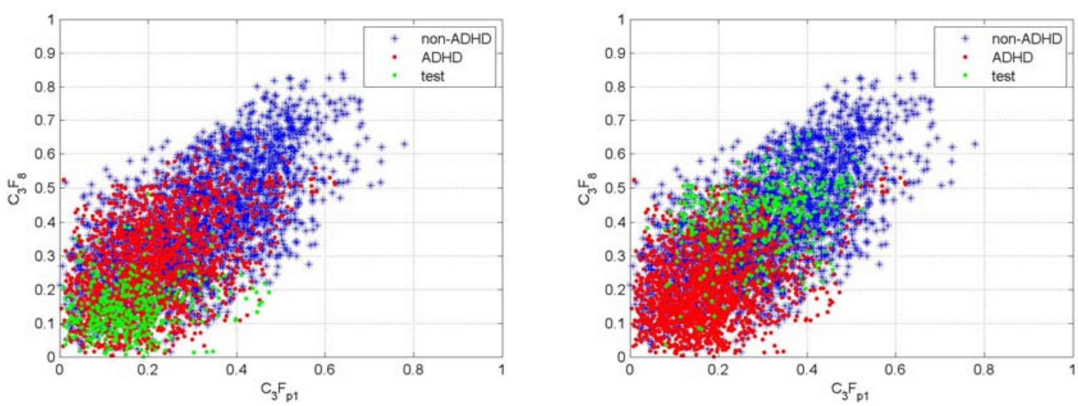

Figure 3.40: Phase synchrony for electrode pairs C_3F_{p1} and C_3F_8 for the γ_1 rhythm “Reading”: two groups and (a) ADHD Subject 1; (a) ADHD Subject 2.

Visual inspection of Figure 3.40 (a) shows that the majority of phase synchrony values for Subject 1 are closer to the centroid of the ADHD cluster. This subject was classified to the correct (ADHD) group most of the time as Figure 3.37 (b) illustrates. However, phase synchrony for Subject 2 (Figure 3.40 (b)) is closer to the centroid of the non-ADHD cluster. As Figure 3.37 (b) indicates, Subject 2 was assigned to the incorrect (non-ADHD) group most of the time.

It is possible – in general – to distinguish between children with and without attention deficit disorder on the basis of phase synchrony computed from their EEG while they are performing attention intensive tasks. For many electrode pairs, phase synchrony was observed to be higher on average for non-ADHD subjects than for ADHD children. Euclidean distance-based classification, performed on phase synchrony, may help – with careful choice of rhythm, task, and appropriate selection of electrode pairs to be processed – to assign a subject accurately to a non-ADHD or ADHD group.

3.4.4 Discrimination between smokers and nonsmokers, schizotypy, and the experimental conditions of eyes closed and eyes open

In this experiment, the EEG data from the "Condition data set" described in Section 3.4.1 was processed by the Phase Synchrony Processor (PSP) as discussed in Section 3.2. Classifications were performed N = 500 times (for N = 500 overlapping time windows). The percentage of correct associations was evaluated.

The phase synchrony was computed according to (3.1) for different electrode pairs. Based on a growing body of evidence that γ_1 rhythm phase synchrony is playing an important role in cognitive processes [1], [10], [20] and differences between γ_1 rhythm phase synchrony of ADHD and non-ADHD individuals discussed in Section 3.4.3, γ_1 rhythm (i.e. 30-40 Hz) phase synchrony was assessed in this experiment. Therefore, the Parks-McClellan FIR band-pass filter with a pass-band from 30 to 40 Hz, transition bands of 2 Hz, and pass-band and stop-band ripples of 0.02 was used. The length of the analysis time window N_w was chosen as 600 samples (1.2 seconds for the sampling frequency f_s = 500 Hz) to decrease finite window length effects as discussed in Section 3.2.

The individual phase synchrony vectors $\mathbf{x_{i,n}}$ were formed as in (3.27) for different *n* and different subjects *i* and averaged within the two groups and over time. Vectors of average phase synchrony $\mathbf{\bar{x}_1}$ and $\mathbf{\bar{x}_2}$ were compared between different groups: high vs. low schizotypy (HiS/LoS), smokers vs. nonsmokers (Sm/nSm), and two experimental conditions (eyes open/closed). Each group contains 10 subjects. The group phase synchrony and variances were compared for different groups. For particular reference electrodes, the Euclidean, Mahalanobis distance-based, quadratic, and VQ classifiers were implemented as discussed in Section 3.4.3.

A. Smokers vs. nonsmokers

This experiment was conducted for the eyes closed condition. No significant differences were observed in group phase synchrony between smokers and nonsmokers for the LoS and mixed (LoS ans HiS) groups. However, for the HiS groups, the average phase synchrony was higher for nonsmokers for all electrode pairs. The comparison – for the C_3 electrode used as reference – is shown in Figure 3.41 for LoS (a) and HiS (b) groups. Each dot represents a value of group phase synchrony $\mathbf{\bar{x}_k}$ evaluated according to (3.28) and the bars denote the one standard deviation (i.e.±σ) intervals as specified by (3.29).

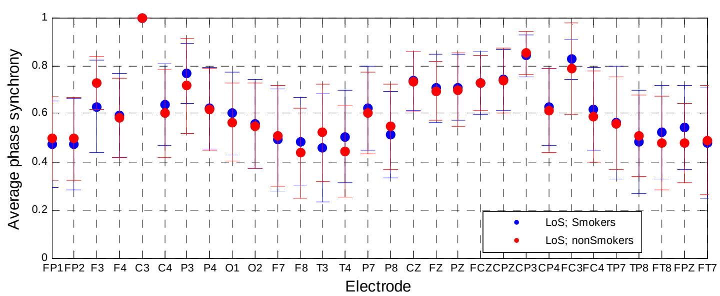

(a)

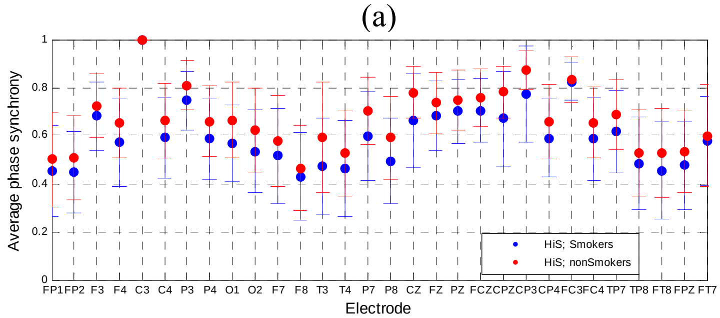

(b)

Figure 3.41: Average γ_1 rhythm phase synchrony using reference C_3 for (a) LoS and (b) HiS groups.

We see in Figure 3.41 (b) that the average phase synchrony is consistently, i.e. for all electrode pairs, higher for HiS nonsmokers than for HiS smokers. Similar results were observed when other electrodes were used as the reference. Next, Euclidean, Mahalanobis distance-based, quadratic, and VQ classification was performed for HiS smokers and HiS non-smokers for C_3 used as the reference electrode. The percentages of correct classification for the Euclidean classifier are shown in Figure 3.42.

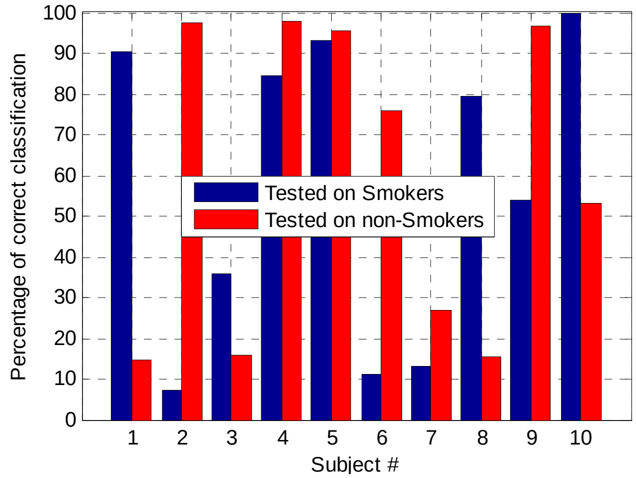

Figure 3.42: Percentages of correct classification of the Euclidean classifier for HiS smokers vs. HiS non-smokers using reference C_3; tested on smokers and nonsmokers.

As shown in Figure 3.42, average percentages of correct classification are 56.3 % and 58.4 % for the groups of smokers and non-smokers respectively. We conclude that – for the present data – no reliable classification between HiS smokers and HiS non-smokers is observed.

B. High vs. low schizotypy

In this experiment, differences were assessed in γ_1 rhythm phase synchrony between the two schizotypy groups. Phase synchrony was computed for the eyes closed condition and averaged within the two groups, i.e. with high and low schizotypy. Figure 3.43 illustrates group phase synchrony and their standard deviations evaluated for the smoking and non-smoking groups. The bars represent one standard deviation.

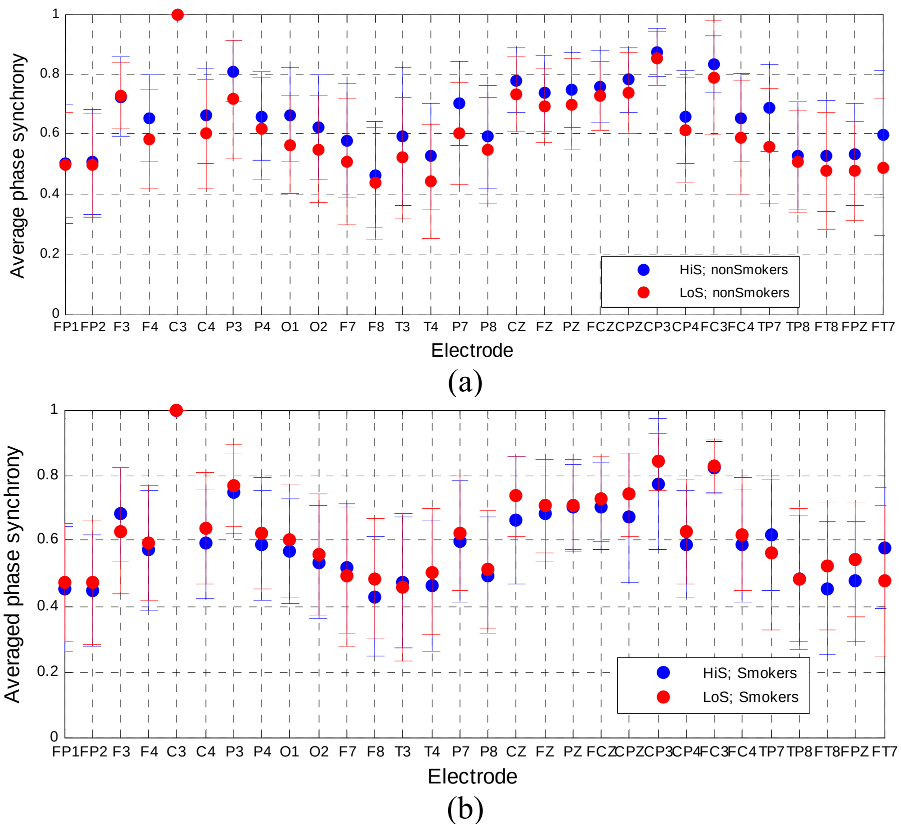

Figure 3.43: Average γ_1 rhythm phase synchrony using reference C_3 for (a) non-smokers, (b) smokers.

Figure 3.43 (a) suggests that γ_1 rhythm phase synchrony is higher on average for high schizotypy non-smokers than for low schizotypy non-smokers for most electrode pairs. The effect of average phase synchrony being different for HiS smokers and LoS smokers is less pronounced (Figure 3.43 (b)). However, this difference is significantly smaller than one standard deviation and neither Euclidean, weighted Euclidean, or Mahalanobis distance-based classifiers, nor quadratic or VQ classifiers, produced reliable results as illustrated in Figure 3.44 for the Euclidean classifier.

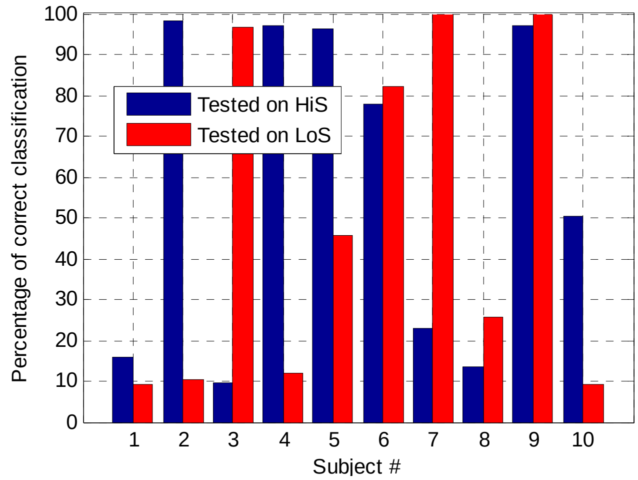

Figure 3.44: Percentages of correct classification of the Euclidean classifier for HiS non-smokers vs. LoS non-smokers using reference C_3; tested on HiS and LoS.

As seen in Figure 3.44, average percentages of correct classification are 57.8 % and 49 % for the HiS and LoS groups respectively. We conclude that – for the present data – no reliable classification between HiS non-smokers and LoS non-smokers is achieved.

C. Conditions of eyes open vs. eyes closed

All previously seen results were obtained for the eyes closed condition. Next, γ_1 rhythm group phase synchrony was computed for the two experimental conditions of eyes closed and eyes open. The comparison has been conducted within high and low schizotypy groups. The phase synchrony was higher on average for the eyes closed condition than for the eyes open condition, as seen in Figure 3.45.

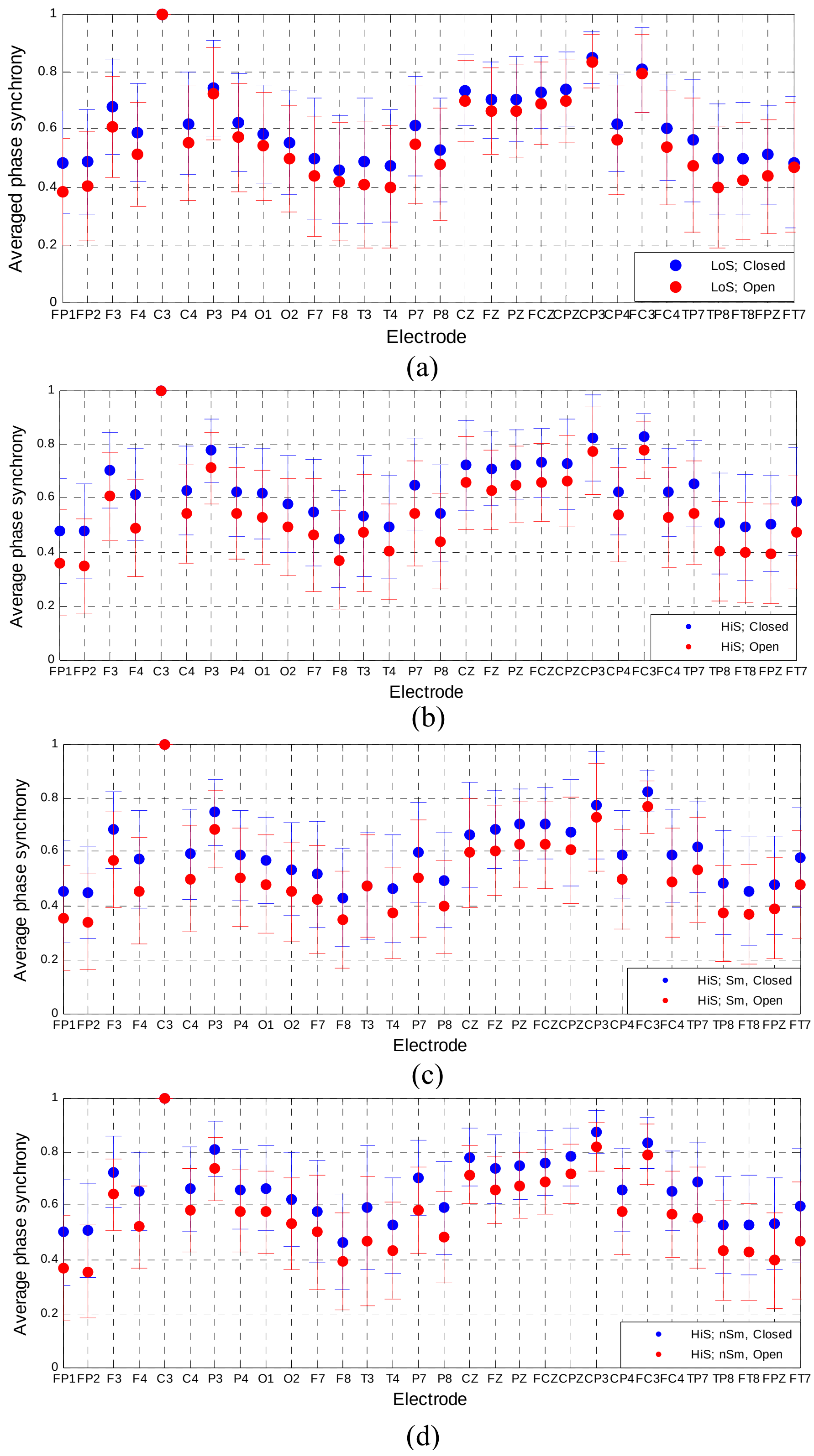

Figure 3.45: Average γ_1 rhythm phase synchrony using reference C_3: (a) all LoS subjects, (b) all HiS subjects, (c) smokers only, (d) nonsmokers only.

It is seen in Figure 3.45 that the effect of γ_1 rhythm phase synchrony being higher on average for the eyes closed condition than for the eyes open conditions is more pronounced when observed on a HiS non-smoking group. Euclidean, variance-weighted Euclidean, covariance-weighted (i.e. Mahalanobis), quadratic, and VQ classification were performed for HiS groups. However, none of these classifiers contributed to reliable classification results as illustrated in Figure 3.46 for the Euclidean and Mahalanobis classifiers.

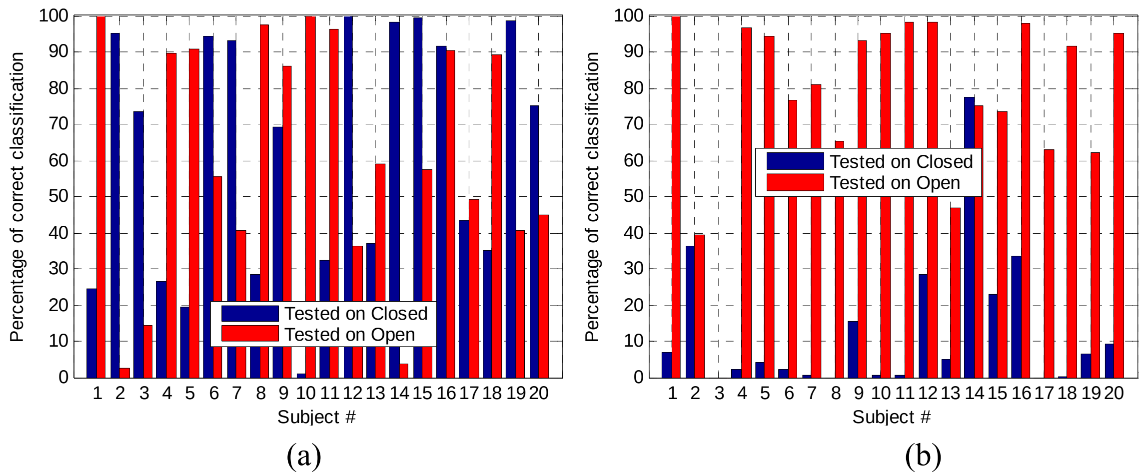

Figure 3.46: Percentages of correct classification of (a) the Euclidean and (b) the Mahalanobis classifiers for HiS subjects for Eyes closed vs. Eyes open conditions using reference C_3.

We see in Figure 3.46 (a) that, average percentages of correct classification for Euclidean classifier are 61.6 % and 61.9 % for the eyes closed and the eyes open conditions. The classification results depicted in Figure 3.46 (b) suggest that the Mahalanobis classifier produces biased results in the case considered here since the percentage of correct classification – 12.7 % for the eyes closed and 77.2 % for the eyes open condition – depends greatly on the subject conditions used to test classifier. Similar but less pronounced trends (i.e. biased toward one of the group classification results) were observed for the weighted Euclidean and quadratic classifiers.

Weighted Euclidean, Mahalanobis, and quadratic classifiers were designed assuming Gaussian data [18]. We consider the frequency of occurrence of phase synchrony values for different subject conditions (i.e. eyes open and eyes closed) and for the C_3F_3 and C_3F_3 electrode pairs as shown in Figure 3.47.

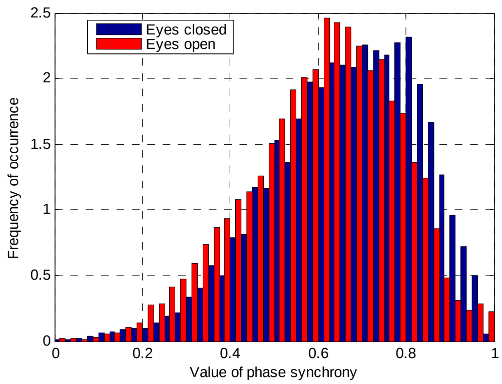

(a)

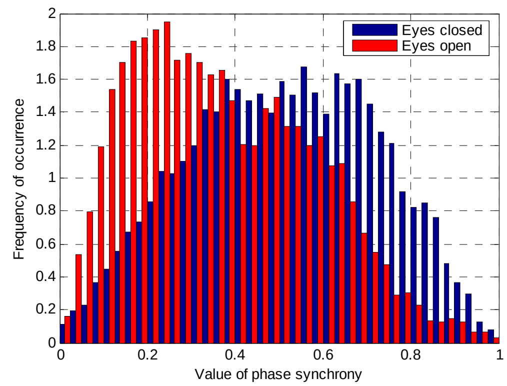

(b)

Figure 3.47: Frequency of occurrence of γ_1 rhythm phase synchrony for two experiment conditions computed for (a) C_3F_3 and (b) C_3F_{p1} electrode pairs.

We may conclude from Figure 3.47 that values of phase synchrony exhibit different distributions when computed for the different participant conditions of eyes open vs. eyes closed. This difference in distribution is more or less pronounced for different electrode pairs. Namely, the distributions differ greatly for the C_3F_{p1} electrode pair, as depicted in Figure 3.47(b). Another important observation is that the distribution of phase synchrony values is, in general, non-Gaussian. As a consequence, classification results provided by weighted Euclidean, Mahalanobis, and quadratic classifiers may – for the data being classified – not be accurate. Also, from this perspective, the previously shown estimates of phase synchrony variance do not offer enough information to make a decision regarding the difference between groups.

We observed that phase synchrony is consistently higher for the majority of subjects when evaluated for the eyes closed condition. However, average phase synchrony differs considerably from subject to subject. Therefore, none of the implemented classifiers provided accurate classification results for the majority of participants when individual synchrony was compared to the two group synchronies, as previously described.

Next, instead of comparing individual phase synchrony with two group synchronies as averaged over different participants, individual phase synchrony was compared with two average (over time) synchronies evaluated for the same subject. For each individual, phase synchrony was computed for 500 time intervals, shifted by 50 samples (i.e. overlapping by 550 samples) as before, for the eyes closed condition and for the eyes open condition. First 100 or 300 successive estimates of individual phase synchrony were used to train the classifier, i.e. to compute two average synchronies as in (3.28) for all classifiers except VQ, since the latter does not require average synchronies. The rest of the individual phase synchronies computed for the same subject (either 400 or 200 vectors) was used to test it. It was found to be beneficial to apply "Maximum masking" as was discussed in Section 3.4.3. Five, ten, or fifteen electrode pairs with the highest difference between average synchronies were selected for processing.

We observed that performance of the weighted Euclidean, Mahalanobis distance-based, and quadratic classifiers depends greatly on the subject conditions used to test them. Namely, the performances were significantly higher when these classifiers were tested on the eyes closed conditions. Electrode masking – with a small number of electrodes used – makes this difference less pronounced. Therefore, we conclude that weighted Euclidean, Mahalanobis distance-based, and quadratic classifiers produce – in our case – biased classification results and we therefore exclude them from further consideration. Euclidean and VQ classifiers provide – in general – equal probability of correct classification and equal error probabilities for both participant conditions.

Using 100 vectors of individual synchrony for training (short training data); the highest average percentages of correct classification of 77.95 % and 78.76 % for the eyes closed and eyes open condition respectively were observed for the VQ classifier when electrode masking with 10 electrode pairs was implemented. When more training data was available (i.e. 300 vectors), the average performance of 81.2 % of correct classification was exhibited by the Euclidean classifier when "Maximum masking" with 5 electrode pairs was used.

Figure 3.48 shows the percentages of correct classifications of the VQ classifier for short training data with 10 electrode pairs used in testing. Subjects 1 through 20 are HiS, while subjects 21 through 40 are LoS.

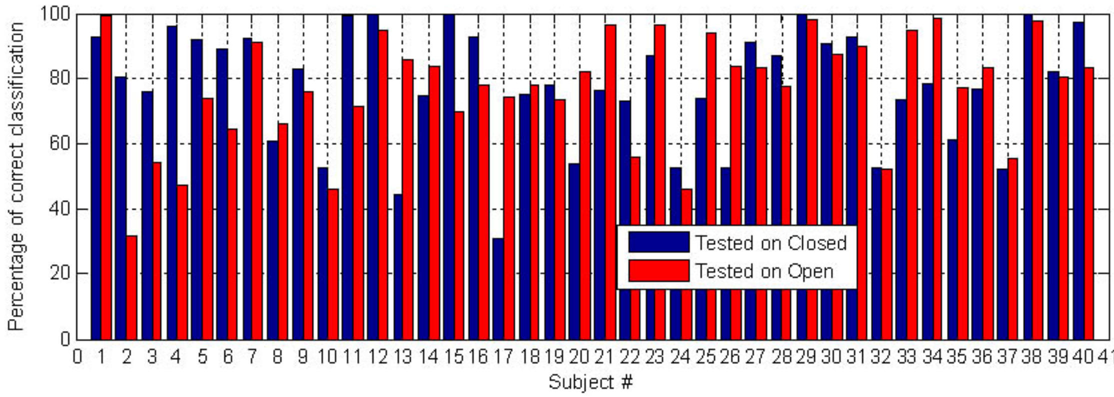

Figure 3.48: Percentages of correct classification with the VQ classifier when using 10 electrode pairs for eyes closed vs. eyes open conditions using reference C_3; tested on eyes closed and eyes open.

We see in Figure 3.48 that the percentage of correct classification for each individual may vary significantly when the classifier is tested on the eyes closed or eyes open conditions. The average percentages of correct classification are 77.95 % and 78.76 % for the eyes closed and eyes open condition respectively. The averaged over two experimental groups percentage of correct classification is 78.36 %. The performance of classifiers is generally higher when more training data is available.

Figure 3.49 shows the γ_1 rhythm phase synchrony distribution for the electrode pairs C_3F_{p1} and C_3F_3, for the eyes open and eyes closed conditions, for Subject 1.

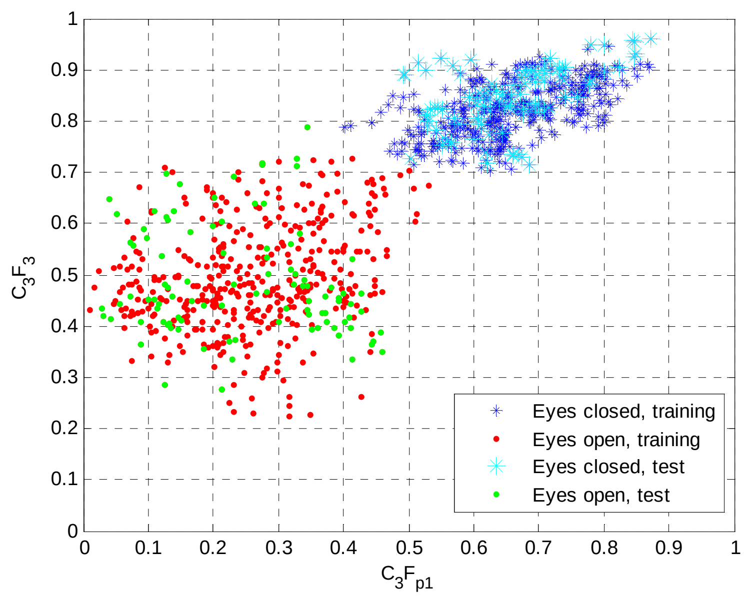

Figure 3.49: Phase synchrony for electrode pairs C_3F_{p1} and C_3F_3 for the γ_1 rhythm.

We see in Figure 3.49 that phase synchrony computed for two different subject conditions forms two distinct clusters.

We conclude that the average γ_1 rhythm phase synchrony is generally different for high schizotypy smokers and nonsmokers; for individuals with high and low schizotypy, and for eyes closed and eyes open experimental conditions. The Euclidean and VQ classifiers may be implemented to discriminate between the eyes open and eyes closed conditions with fairly high percentage of correct classification. The latter could be used, for instance, for vigilance monitoring.

3.5 References

[1] J.-P. Lachaux, E. Rodrigues, J. Martinerie, and F. J. Varela, "Measuring phase synchrony in brain signals," *Human Brain Mapping* #8, 1999, pp. 194-208.

[2] F. Mormann, K. Lehnertz, P. David, C. E. Elger, "Mean phase coherence as a measure for phase synchronization and its application to the EEG of epilepsy patients," *Physica D*, #144, 2000, pp. 358-369.

[3] C. Allefeld and J. Kurths, "Multivariate phase synchronization analysis of EEG data," *IEICE Transactions Fundamentals*, vol. E86-A, #9 September, 2003, pp. 2218-2221.

[4] C. Allefeld and J. Kurths, "An approach to multivariate phase synchronization analysis and its application to event-related potentials," *International Journal of Bifurcation and Chaos*, vol. 14, #2, 2004, pp. 417-426.

[5] I. N. Bronshtein and K. A. Semendjaev, *Mathematical handbook for engineers.* Franklin, Budapest, 1964, in Russian.

[6] A. Papoulis and S. Unnikrishna Pillai, *Probability, random variables, and stochastic processes.* McGraw-Hill, New York, 2002, 4th Edition.

[7] G. Tcheslavski and A. A. (Louis) Beex, "Properties and parameter selection for phase synchrony processing of EEG signals," *Proceedings of the Second IASTED International Multi-Conference Signal and Image Processing (ACIT-SIP)*, June 20-24, 2005, Novosibirsk, Russia, pp. 164-169.

[8] S. K. Mitra, *Digital signal processing: a computer-based approach.* – 2nd ed. McGraw-Hill Series in Electrical and Computer Engineering, 2001.

[9] A. V. Oppenheim and R. W. Schafer, *Discrete-time signal processing.* Prentice Hall signal processing series, New Jersey, 1989.

[10] K. M. Spencer, P. G. Nestor, M. A. Niznikiewicz, D. F. Salisbury, M. E. Shenton, and R. W. McCarley, "Abnormal neural synchrony in schizophrenia," *The Journal of Neuroscience*, August 13, 2003, #23 (19), pp. 7407-7411.

[11] W. H. R. Miltner, C. Braun, M. Arnold, H. Witte, and E. Taubs, "Coherence of gamma-band EEG activity as a basis for associative learning," *Letters to Nature*, vol. 397 (04), February 1999, pp. 434-436.

[12] J. P. Nolan, "Numerical calculation of stable densities and distribution functions," *Communicational Statistics – Stochastic models*, 13 (4), 1997, pp. 759-774.

[13] H. Crawford and M. Barabasz, "Quantitative EEG magnitudes in children with and without attention deficit disorder during neurological screening and cognitive tasks," *Child Study Journal*, vol. 26 #1, 1996, pp. 71-86.

[14] A. Raine, "The schizotypal Personality Questionnaire (SPQ): A measure of schizotypal personality based on DSM-III-R criteria," *Schizophrenia Bulletin*, vol. 17, 1991, pp. 555-564.

[15] L. Wan, *P50 Sensory Gating: Impact of High vs. Low Schizotypy Personality and Smoking Status, Master's Thesis,* Virginia Tech, Blacksburg, Sept. 2004.

[16] C. Tallon-Baudry, O. Bertrand, and C. Fischer, "Oscillatory synchrony between human extrastriate areas during visual short-term memory maintenance," *The Journal of Neuroscience*, vol. 21 (20), RC177, 2001, pp. 1-5.

[17] R. Wohlford, E. Wrench, Jr., and B. Landell, "A comparison of four techniques for automatic speaker recognition," *ICASSP-80*, 1980, pp. 908-911.

[18] R. O. Duda and P. E. Hart, *Pattern Classification and scene analysis*, John Wiley & Sons, 1973.

[19] V. Namburu, *Speech coder using line spectral frequencies of cascaded second order predictors, PhD dissertation,* Virginia Tech, Blacksburg, Nov. 2001.

[20] J. Bhattacharya and H. Petsche, "Enhanced phase synchrony in the electroencephalograph γ band for musicians while listening to music," *Physical Review E*, vol. 64(1), 2001, pp. 012902-1 – 012902-4.

Chapter 4

Model-based coherence function: proposed estimator

In this Chapter we select a model for a pair of EEG electrodes, develop and test the algorithm estimating the parameters of such a model, and process real EEG records using the proposed model.

4.1 Model of a pair of EEG electrodes

Autoregressive (AR), moving average (MA), and autoregressive moving average (ARMA) processes can be modeled as the output signal of a linear time invariant filter with the corresponding transfer function driven by white noise [1].

While modeling cross spectra or the cross-correlation between two stochastic processes x_n and y_n, the model represented in Figure 4.1 is traditionally assumed.

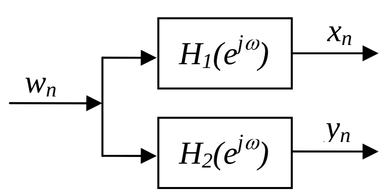

Figure 4.1: Block diagram of a simple linear model.

The processes studied here are modeled as the output sequences of two linear time invariant filters, with frequency responses $H_1(e^{j\omega})$ and $H_2(e^{j\omega})$ respectively, both excited by the same normally distributed white noise process w_n with zero-mean and unit variance $\sigma_w^2 = 1$.

Based on this model, we can write the following expressions for the auto and cross spectra:

$$
\begin{aligned}
S_{xx}(e^{j\omega t}) &= H_1(e^{j\omega t}) \cdot H_1^*(e^{j\omega t}) \cdot \sigma_w^2 \\
S_{yy}(e^{j\omega t}) &= H_2(e^{j\omega t}) \cdot H_2^*(e^{j\omega t}) \cdot \sigma_w^2 \\
S_{xy}(e^{j\omega t}) &= H_1(e^{j\omega t}) \cdot H_2^*(e^{j\omega t}) \cdot \sigma_w^2
\end{aligned}
\tag{4.1}
$$

Since the variance of the input noise $\sigma_w^2 = 1$, and assuming that the noise is a wide sense stationary process and filter parameters are not changing over time, (4.1) can be simplified as follows:

$$
\begin{aligned}
S_{xx}(e^{j\omega}) &= H_1(e^{j\omega}) \cdot H_1^*(e^{j\omega}) \\
S_{yy}(e^{j\omega}) &= H_2(e^{j\omega}) \cdot H_2^*(e^{j\omega}) \\
S_{xy}(e^{j\omega}) &= H_1(e^{j\omega}) \cdot H_2^*(e^{j\omega})
\end{aligned}
\tag{4.2}
$$

Consider the magnitude squared coherence function:

$$
\begin{aligned}
\Gamma^2(e^{j\omega}) &= \frac{\left|S_{xy}(e^{j\omega})\right|^2}{S_{xx}(e^{j\omega}) \cdot S_{yy}(e^{j\omega})} \\
&= \frac{H_1(e^{j\omega}) \cdot H_2^*(e^{j\omega}) \cdot H_1^*(e^{j\omega}) \cdot H_2(e^{j\omega})}{H_1(e^{j\omega}) \cdot H_1^*(e^{j\omega}) \cdot H_2(e^{j\omega}) \cdot H_2^*(e^{j\omega})} \equiv 1
\end{aligned}
\tag{4.3}
$$

As we see, the magnitude squared coherence is one for all frequencies while employing the model depicted in Figure 4.1. The unit coherence between the processes x_n and y_n is destroyed by additional independent noise (or signal) injections. The block diagram of the modified linear model is shown in Figure 4.2.

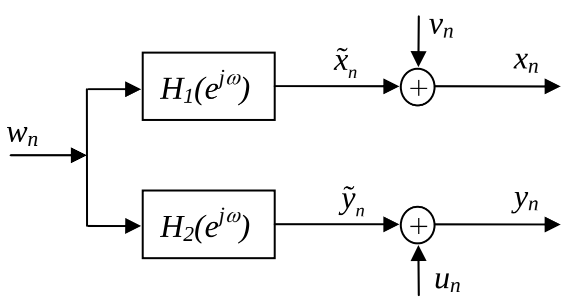

Figure 4.2: Block diagram of the modified linear model.

Filters $H_1(e^{j\omega})$ and $H_2(e^{j\omega})$ are assumed to be linear and time invariant and all input noise sequences w_n, v_n and u_n are statistically independent, zero mean, normally distributed processes. We represent the sequences x_n and y_n as sums of the signal components $\tilde{x}_n$ and $\tilde{y}_n$ and the white noise sequences v_n and u_n respectively. The noise sequences can be pre-multiplied by noise variances σ_v^2 and σ_u^2 to account for different signal to noise ratios (SNR). In other words, both sequences x_n and y_n originate from the same source and are contaminated by independent Gaussian noise.

Based on the new model, the auto- and cross spectra are specified as follows:

$$\begin{aligned} S_{xx}(e^{j\omega}) &= H_1(e^{j\omega}) \cdot H_1^*(e^{j\omega}) + \sigma_v^2 \\ S_{yy}(e^{j\omega}) &= H_2(e^{j\omega}) \cdot H_2^*(e^{j\omega}) + \sigma_u^2 \\ S_{xy}(e^{j\omega}) &= H_1(e^{j\omega}) \cdot H_2^*(e^{j\omega}) \end{aligned} \tag{4.4}$$

The magnitude squared (MS) coherence is then

$$\Gamma^2(e^{j\omega}) = \frac{H_1(e^{j\omega}) \cdot H_2^*(e^{j\omega}) \cdot H_1^*(e^{j\omega}) \cdot H_2(e^{j\omega})}{\left(H_1(e^{j\omega}) \cdot H_1^*(e^{j\omega}) + \sigma_v^2\right) \cdot \left(H_2(e^{j\omega}) \cdot H_2^*(e^{j\omega}) + \sigma_u^2\right)} \tag{4.5}$$

It is seen now that the coherence function converges to unity only when the power of both noise sources vanishes. In this case, the model is equivalent to the one depicted in Figure 4.1.

In conclusion, it is important to keep in mind that the developed model may be applied only for short EEG records due to the non-stationary nature of the EEG as mentioned in Section 1.5. We will assume a sampling rate of 256 Hz and 100 ms as the length of the locally stationary frames [2], [3]. Therefore, the model parameters must be estimated based on observed signal (EEG) frames, whose length does not exceed 25 samples.

4.2 Method for model parameter estimation

The problem of evaluating the model parameters in the presence of white additive background noise has been widely discussed [4], [5], and [6]. It can be shown [4] that the power spectral density (PSD) of the output of an AR(*p)* filter $A(e^{j\omega})$ driven by white noise with variance σ^2 and corrupted by another white noise with variance σ_{noise}^2 is given as

$$P(e^{j\omega}) = \frac{\sigma^2}{\left|A(e^{j\omega})\right|^2} + \sigma_{noise}^2 \tag{4.6}$$

Rewriting the last expression for the x_n sequence depicted in Figure 4.2, and assuming the order p of the AR model, we obtain

$$P_x(e^{j\omega}) = \frac{\sigma_w^2}{\left|\sum_{k=0}^{p} a_k e^{-jk\omega}\right|^2} + \sigma_v^2\,, \quad a_0 \equiv 1 \tag{4.7}$$

or

$$P_x(e^{j\omega}) = \frac{\sigma_w^2 + \sigma_v^2 \left|\sum_{k=0}^{p} a_k e^{-jk\omega}\right|^2}{\left|\sum_{k=0}^{p} a_k e^{-jk\omega}\right|^2}\,, \quad a_0 \equiv 1 \tag{4.8}$$

One can recognize that the true model for (4.8) is ARMA(p,p) rather than AR(p) [4]. Based on this, some suboptimal approaches can be applied to evaluate the AR parameters of the model (4.8) along with the variance of the driving noise σ_w^2 and the variance of the measurement noise σ_v^2. The procedure for AR parameter estimation will be discussed in detail later.

Once the AR parameters are evaluated, the noise variances can be estimated by the least squares estimator proposed by Parzen [4], [7]. He has shown that solving (4.7) in a least-squares sense – with AR parameters replaced by their estimates and the true PSD replaced by its DFT estimate – leads to

$$\begin{bmatrix} 1 & \sum_{k=0}^{p} \left|\hat{a}_k\right|^2 \\ \sum_{k=0}^{p} \left|\hat{a}_k\right|^2 & \sum_{k=0}^{2p} \left|\hat{a}_k \otimes \hat{a}_k\right|^2 \end{bmatrix} \begin{bmatrix} \hat{\sigma}_w^2 \\ \hat{\sigma}_v^2 \end{bmatrix} = \begin{bmatrix} \frac{1}{N-p} \sum_{n=p}^{N-1} \left|x_n \otimes \hat{a}_n\right|^2 \\ \frac{1}{N-2p} \sum_{n=2p}^{N-1} \left|x_n \otimes \hat{a}_n \otimes \hat{a}_n\right|^2 \end{bmatrix} \tag{4.9}$$

where $\hat{a}_k$ are the estimates of the AR parameters, p indicates the system order, N is the length of the modeled frame x_n, and $\otimes$ represents linear convolution.

To estimate the AR parameters, the least squares modified Yule-Walker equation (LSMYWE) estimator [4] was used. This estimator is among the suboptimal solutions mentioned above for parameter estimation in the presence of measurement noise [4] and can be described as

$$\hat{\mathbf{a}} = -\left(\hat{\mathbf{R}}^{\mathbf{H}}\hat{\mathbf{R}}^{\mathbf{H}}\right)^{-1} \hat{\mathbf{R}}^{\mathbf{H}}\hat{\mathbf{r}} \tag{4.10}$$

where

$$\hat{\mathbf{R}} = \begin{bmatrix} \hat{r}_{xx,q} & \hat{r}_{xx,q-1} & \cdots & \hat{r}_{xx,q-p+1} \\ \hat{r}_{xx,q+1} & \hat{r}_{xx,q} & \cdots & \hat{r}_{xx,q-p+2} \\ \vdots & \vdots & \vdots & \vdots \\ \hat{r}_{xx,M-1} & \hat{r}_{xx,M-2} & \cdots & \hat{r}_{xx,M-p} \end{bmatrix} \tag{4.11}$$

$$\hat{\mathbf{r}} = \begin{bmatrix} \hat{r}_{xx,q+1} & \hat{r}_{xx,q+2} & \cdots & \hat{r}_{xx,M} \end{bmatrix}^T$$

Here $\hat{r}_{xx,n}$ represents the n^{th} element of the autocorrelation estimate of the sequence x_n, p and q are the orders of the AR and MA portions of the model respectively, and M is the number of equations used to determine the system in (4.10). Since the orders of the AR and MA portions of the model in (4.8) are the same, i.e. $p = q$, we can rewrite (4.11) as follows:

$$\hat{\mathbf{R}} = \begin{bmatrix} \hat{r}_{xx,p} & \hat{r}_{xx,p-1} & \cdots & \hat{r}_{xx,1} \\ \hat{r}_{xx,p+1} & \hat{r}_{xx,p} & \cdots & \hat{r}_{xx,2} \\ \vdots & \vdots & \vdots & \vdots \\ \hat{r}_{xx,M-1} & \hat{r}_{xx,M-2} & \cdots & \hat{r}_{xx,M-p} \end{bmatrix} \tag{4.12}$$

$$\hat{\mathbf{r}} = \begin{bmatrix} \hat{r}_{xx,p+1} & \hat{r}_{xx,p+2} & \cdots & \hat{r}_{xx,M} \end{bmatrix}^T$$

Note that the system (4.10) is determined when $M = 2p$. Thus, when solving (4.10), at least $2p$ equations must be used.

The quality of the AR estimates may be increased by applying a filter matched with the AR(p) process [4]. In this case the signal (the AR(p) process) is enhanced relative to the noise by means of the filter, with a frequency response magnitude specified as follows [5], [6], and [8]:

$$\left|H_m(e^{j\omega})\right| = \frac{\hat{P}_x(e^{j\omega})}{\hat{P}_x(e^{j\omega}) + \hat{\sigma}_v^2} \tag{4.13}$$

where $\hat{P}_x(e^{j\omega})$ is a PSD computed according to (4.7) or (4.8) when the true AR parameters are replaced by their estimates.

The estimation procedure is again applied to the enhanced signal. Filtering followed by parameter estimation may be performed iteratively.

Another way to improve the quality of the AR(p) parameter and noise variance estimates is by averaging these estimates over a number of signal frames [9]. The AR coefficients are estimated for each frame and then averaged over all frames.

To develop and test a suboptimal approach to AR parameter estimation, an AR(p) process was generated and degraded by additive white noise, according to Figure 4.2, and the estimation and enhancement procedures described above were implemented. According to Palaniappan and colleagues, the EEG can be successfully modeled as an AR process of third order [10]. Based on this, sequences $\tilde{x}_n$ and $\tilde{y}_n$ were generated as AR(3) processes with the following AR filter coefficients:

$$\mathbf{a} = [1 \quad -1.3 \quad 1.26 \quad -0.56]$$

$$\mathbf{c} = [1 \quad -1.76 \quad 1.41 \quad -0.43] \tag{4.14}$$

where **a** represents the AR coefficients of the filter $H_1(e^{j\omega})$ and **c** corresponds to the filter $H_2(e^{j\omega})$ as specified in Figure 4.2. The variance of the driving noise σ_w^2 was chosen as 1. The poles corresponding to the selected coefficients **a** and **c** are:

Poles of a:	**Poles of** c:
$\mathbf{p_{a,1} = 0.3158 + 0.8591i}$	$\mathbf{p_{c,1} = 0.5779 + 0.6146i}$
$\mathbf{p_{a,2} = 0.3158 - 0.8591i}$	$\mathbf{p_{c,2} = 0.5779 - 0.6146i}$
$\mathbf{p_{a,3} = 0.6684}$	$\mathbf{p_{c,3} = 0.6042}$

The corresponding pole-zero diagrams are shown in Figure 4.3.

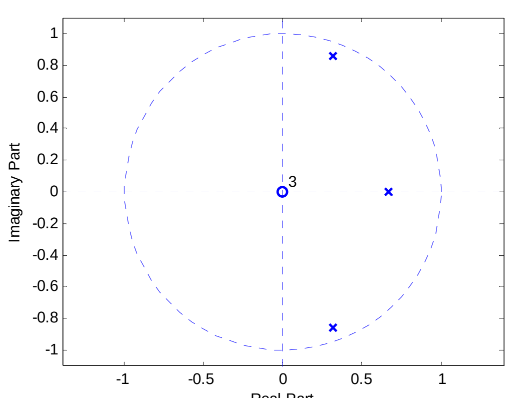

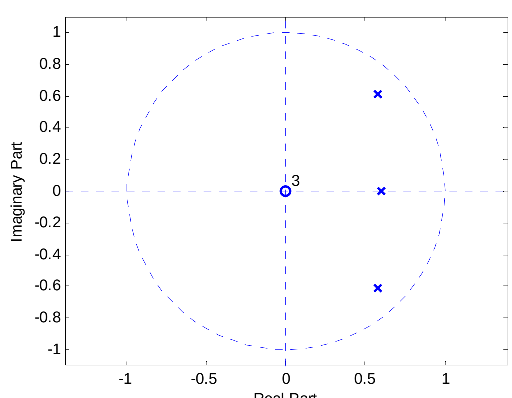

Figure 4.3: Pole-zero diagrams of filters (a) H_1 and (b) H_2.

In Figure 4.3 the zeros are indicated by o's and the poles are represented by x's. The frequency responses of the AR filters can be computed as follows [1]:

$$H_1(e^{j\omega}) = \frac{\sigma_w}{\sum_{k=0}^{3} a_k e^{-jk\omega}} \tag{4.15}$$

$$H_2(e^{j\omega}) = \frac{\sigma_w}{\sum_{k=0}^{3} c_k e^{-jk\omega}} \tag{4.16}$$

The frequency responses, computed for the AR parameters (4.14) according to (4.15) and (4.16), are illustrated in Figure 4.4.

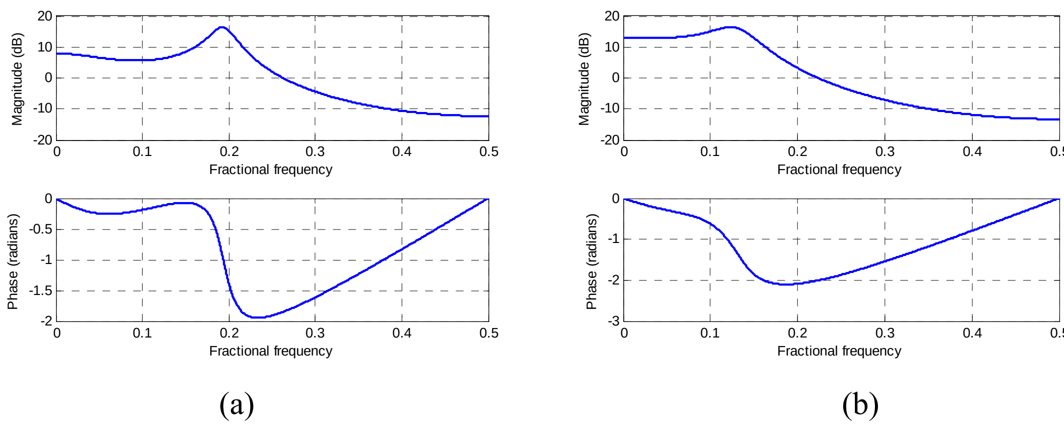

Figure 4.4: Frequency responses of filters (a) H_1 and (b) H_2.

When modeling the test signals, the driving noise w_n, was generated as a Gaussian sequence with zero mean and unit variance. The additive noise sequences v_n and u_n were also Gaussian processes, with zero mean and variances corresponding to the signal to noise ratio (SNR). The SNR was assumed to be in the range of 3 to 10 dB. This assumption is based on studies of Schlögl and colleagues [11] and beim Graben [12]. The variance of the noise additive to the x_n sequence was selected based on the following definition of SNR [4]:

$$\eta = \frac{P}{\sigma_v^2} \tag{4.17}$$

where P, the signal power, can be evaluated as

$$P = \frac{\sigma_w^2}{1 - p_{a,1} \cdot p_{a,2}} \tag{4.18}$$

Here $p_{a,1}$ and $p_{a,2}$ represent the complex conjugate roots of the polynomial **a** (poles of the frequency response $H_1(e^{j\omega})$).

Finally, combining the last two equations and considering SNR in dB, we obtain the following expression for the variance of the additive noise:

$$\sigma_v^2 = \frac{\sigma_w^2}{10^{\frac{SNR}{10}} \left(1 - p_{a,1} \cdot p_{a,2}\right)} \tag{4.19}$$

For the sequence y_n, the variance of the additive noise σ_u^2 can be found analogously. The true PSDs of the noise-free and the white noise contaminated AR sequences, computed according to (4.8), are shown in Figure 4.5. The corresponding SNRs are shown in the legend.

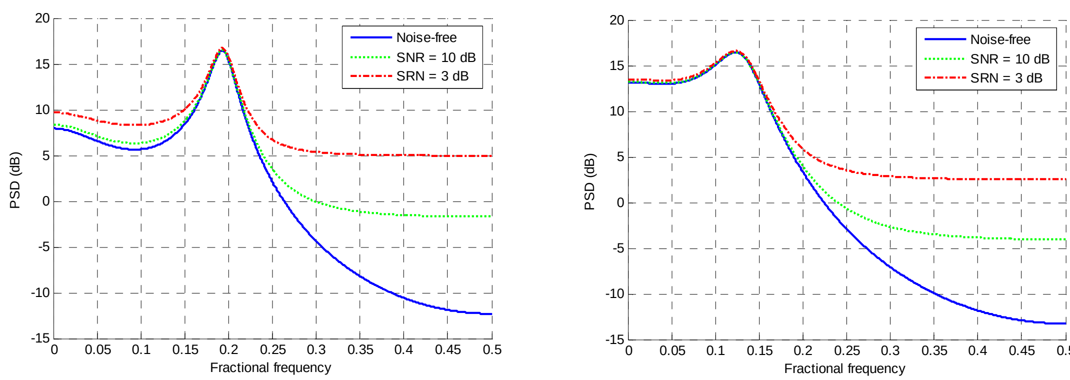

(a) (b)

Figure 4.5: True Power Spectral Densities (PSDs) of the simulated sequences (a) x_n and (b) y_n.

It is seen in Figure 4.5 that the additive white noise leads to less pronounced peaks of the PSD. However, we observe that the additive noise – at the indicated SNR – has a minor effect on the auto-PSDs around their peaks.

Considering (4.4), we can conclude that additive noise does not affect the cross-PSD since the cross-PSD only depends on the frequency responses $H_1(e^{j\omega})$ and $H_2(e^{j\omega})$, which are not affected by additive noise. The true cross-PSD – for the case considered here – is shown in Figure 4.6.

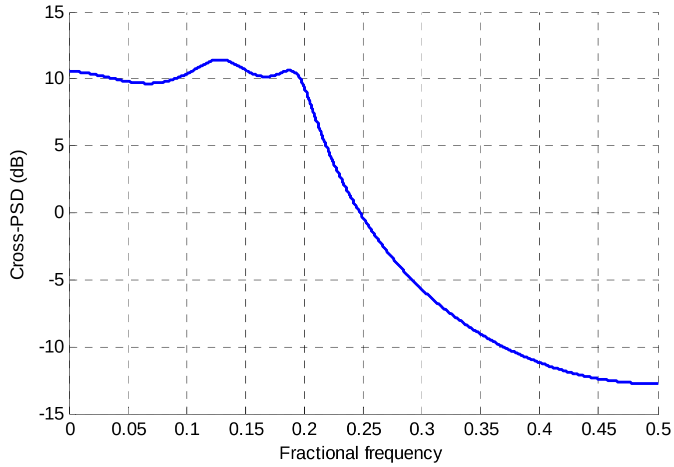

Figure 4.6: True cross-PSD.

The corresponding true MS coherence function for the AR(3) parameters given in (4.14) is presented in Figure 4.7 for different SNRs. The same SNR was assumed for sequences x_n and y_n.

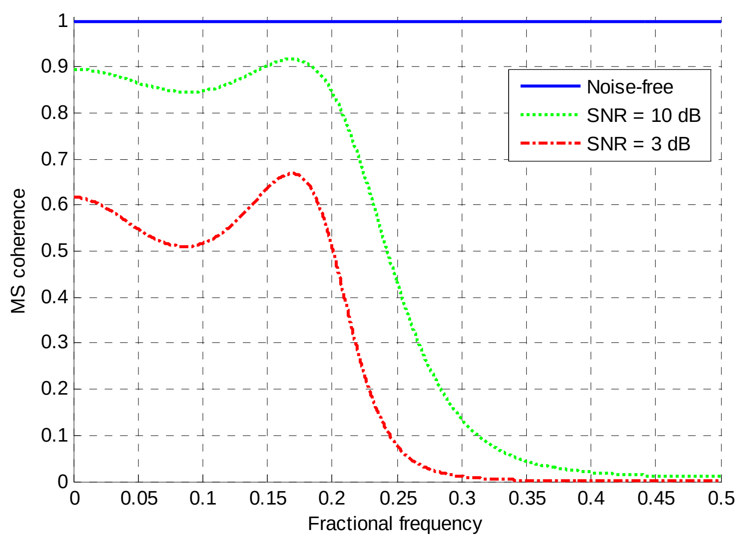

Figure 4.7: True MS coherence.

We see in Figure 4.7 that in the noise-free case the coherence equals one. This result is consistent with our findings in Section 4.1. Additive noise destroys coherence, and increased variance of the additive noise leads to a decrease in the coherence function.

To evaluate the MS coherence function according to (4.5), we need to estimate the AR(p) parameters of two filters, the variance of the driving noise and the variances of two additive noises. The AR filter frequency responses can then be estimated according to (4.15) and (4.16) with the true AR coefficients replaced by their estimates.

The previously described LSMYW estimator was implemented in Matlab together with Parzens' estimator for the noise variance. The methods, discussed previously to enhance the signal as in (4.13) and for AR parameter averaging, were tested also.

To evaluate the quality of the LSMYW estimator, the AR parameters were estimated for M = 100 signal records generated according to the diagram in Figure 4.2, with statistically independent noise. The m^{th} PSD estimate $P_{x,n,m}$ was evaluated for the m^{th} set of parameter estimates and compared to the true PSD computed according to (4.8). The *MAE* – the mean absolute error, i.e. the mean of the absolute difference between the m^{th} spectrum estimate $\hat{P}_{x,n,m}$ and the true spectrum S_{xx} – was used as a measure of the quality of the estimator, and evaluated as follows:

$$E = \frac{1}{M}\sum_{m=1}^{M}\left[\frac{1}{N}\sum_{n=1}^{N}\left|\hat{P}_{x,n,m} - S_{xx,n}\right|\right] \tag{4.20}$$

where n represents the n^{th} (frequency) sample of the corresponding sequence of length N.

The absolute bias and the standard deviation of the AR parameter estimates and noise variances – averaged over M trials – were evaluated also.

4.3 Model parameter estimation results

In this section we present numerical results of the estimation of the model AR parameters and the variances of the driving and additive noise sequences as described in Section 4.2. We observed that some estimates lead to an unstable AR system, i.e. the auto-PSD corresponding to the obtained estimates contains spikes greatly exceeding the true PSD. Empirically, when the maximum value of the auto-PSD exceeded 100, such a PSD was considered a numerically unstable solution. The probability of unstable solutions is illustrated in Figure 4.8 for different additive noise variances and unbiased and biased correlation estimates. The standard deviation of the additive noise is reported in the legend.

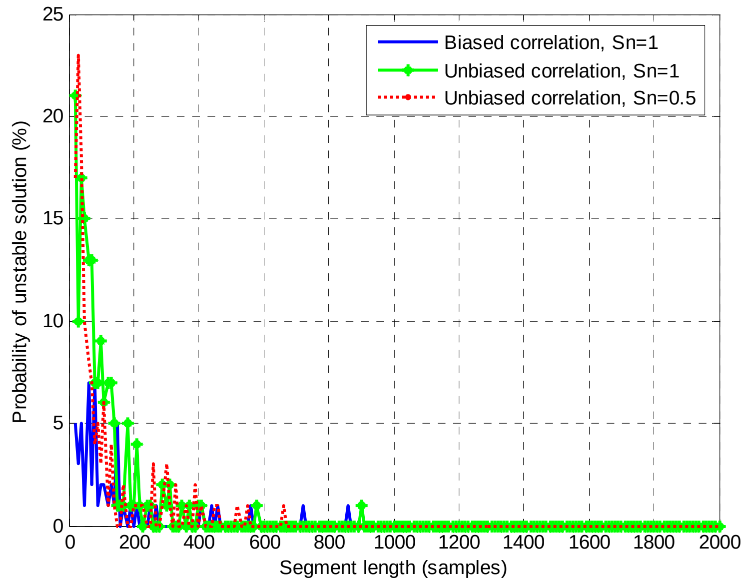

Figure 4.8: Probability of unstable AR auto-spectrum solutions (POUS).

As seen in Figure 4.8, the probability of getting an unstable solution is considerably higher when short segments are analyzed and when the unbiased ACF estimator is used. However, the power of the additive noise (in the assessed range) does not seem to affect the probability of getting an unstable spectral estimate.

Kay suggests [4] using the unbiased ACF estimator since then the average equation error is zero. Therefore, the unbiased correlation estimator was used later and unstable solutions were discarded.

One factor that greatly affects the performance of the estimator is *M*, the number of equations used to solve the Yule-Walker system in (4.10). The mean absolute error (MAE) of the auto-PSD estimation as specified by (4.20) is presented in Figure 4.9 for different *M*, as shown in the legend.

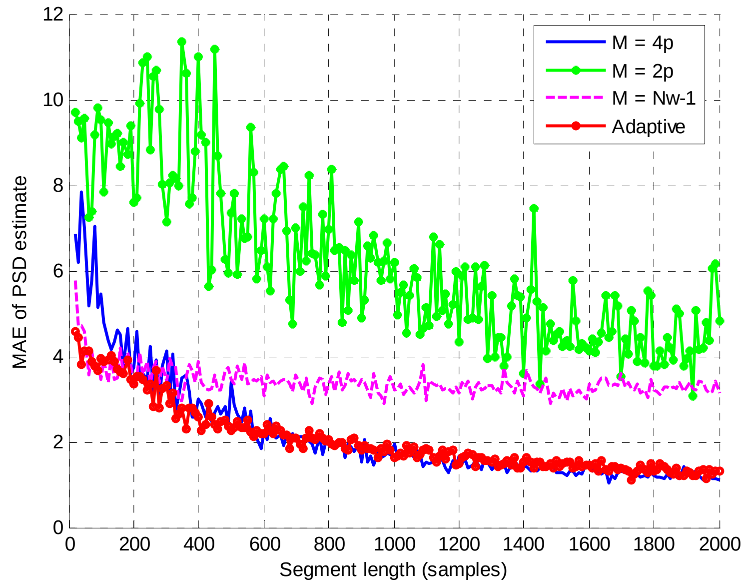

Figure 4.9: MAE of auto-PSD estimate for different number of equations M; $\sigma_v = 1$.

As previously discussed, the minimum number of equations necessary to determine the system in (4.10) is $M = 2p$, where p is the assumed order of the AR system. The maximum number of equations is $M = N_w$-1. We see in Figure 4.9 that the estimator exhibits the worst performance when the minimum number of equations is used. Doubling M leads to a considerable decrease in MAE. Utilizing the maximum number of equations can be beneficial when the segment length is short. Based on these observations, the number of equations M was selected as the maximum when the segment length did not exceed 60 and as $6p$ otherwise.

To improve the quality of the developed estimator, we consider AR parameter averaging and the signal enhancement technique, as described in Section 4.2.

4.3.1 Effect of parameter averaging

We implement a modification of the AR parameter estimates proposed by Beex and Rahman [9]. Namely, signal frames used to obtain estimates are overlapping in this study, while no overlapping was implemented in [9]. AR parameters and noise variances were estimated for signals at two SNRs, namely, 10 dB and 3 dB. Assuming that all estimates are normally distributed, the bias and standard deviation of the parameter estimates – averaged over 100 trials – were used as measures of quality.

Figure 4.10 represents the average bias of the driving and additive noise power estimates according to (4.9), for different SNRs, with and without averaging, and for various lengths of the analyzed segments. When averaging was implemented, three signal frames of length of 0.8 of the length of the corresponding segment were formed via windowing. The frames were overlapping by 80 % of their length. AR parameters and noise powers were estimated for each frame and then averaged over all frames.

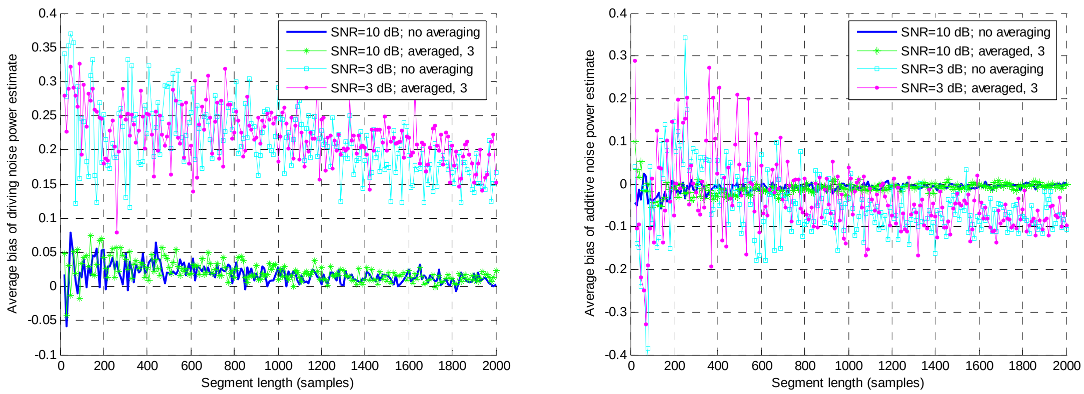

(a) (b)

Figure 4.10: Average bias of power estimates of (a) driving and (b) additive noise.

We see in Figure 4.10 (a) that additive noise leads to biased results for the power of the driving noise estimation. Averaging does not affect this bias. As seen in Figure 4.10 (b), the power of the additive noise can be estimated without considerable bias on average. The average bias is less when SNR is higher. Averaging the estimates does not offer improvements in terms of bias.

We verify next the previously stated assumption regarding the normal distribution of the power estimates. 10,000 estimates of the additive noise powers were obtained when the standard deviation of the additive noise was $\sigma_n = 0.5$. The histogram of additive noise power estimates is shown in Figure 4.11 together with the corresponding Gaussian curve computed as

$$f_G(x) = \frac{1}{\sigma\sqrt{2\pi}} e^{-\frac{(x-\mu)^2}{2\sigma^2}} \tag{4.21}$$

where μ and σ are the sample mean and sample standard deviation found from those same estimates.

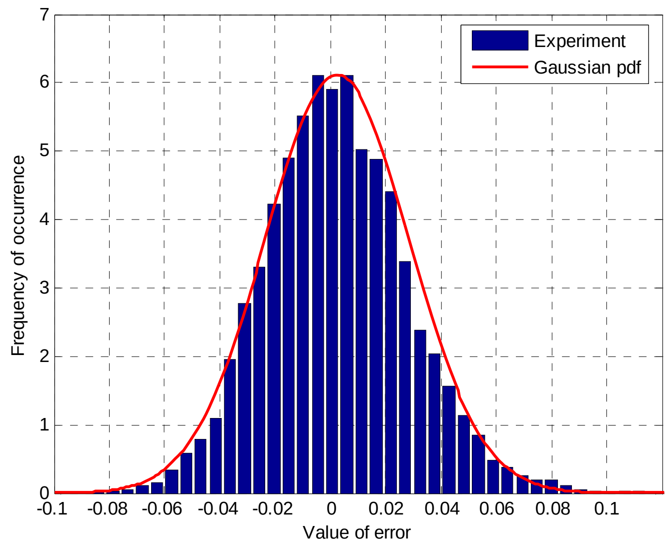

Figure 4.11: Normalized frequency of occurrence of error of the additive noise power estimate, $\sigma_v = 0.5$; 10,000 trials.

From Figure 4.11 we conclude that the estimates may be reasonably considered as being normally distributed.

We consider next the bias of the AR(3) parameter estimation, as illustrated in Figure 4.12. The corresponding SNR are indicated in the legend.

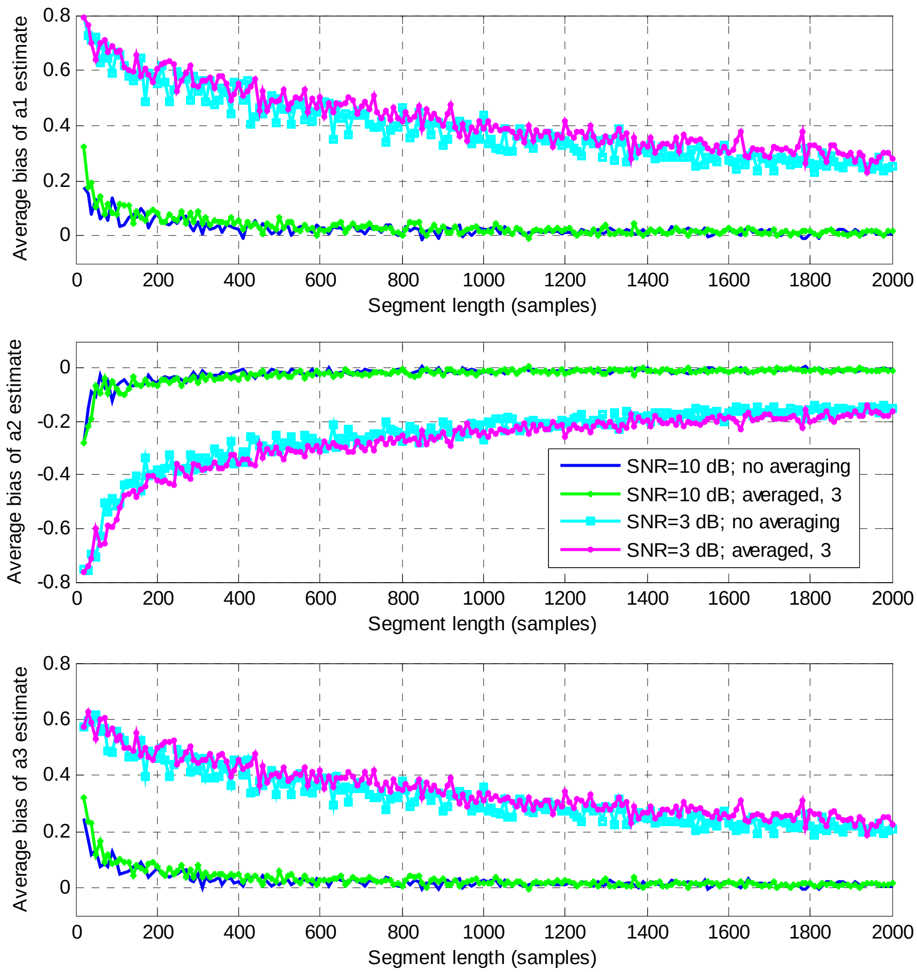

Figure 4.12: Average bias of autoregressive, i.e. AR(3), parameter estimates.

It is seen in Figure 4.12 that the AR(3) parameter estimates, in the presence of noise, are subject to bias. Averaging does not lead to a decrease in this bias.

We consider the influence of averaging on the standard deviation of additive and driving noise power estimates. Figure 4.13 shows the standard deviation of the driving and additive noise power estimates.

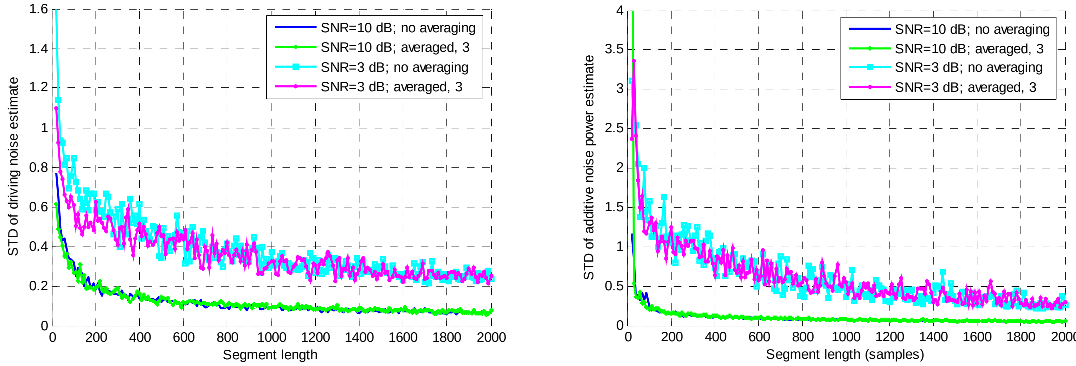

(a) (b)

Figure 4.13: Standard deviation of the (a) driving and (b) additive noise power estimates.

We see in Figure 4.13 (a) that averaging may – especially in low SNR cases and when segment length is small – lead to a decrease in the standard deviation of the driving noise power estimate. The additive noise power estimate, as seen in Figure 4.13 (b) is subject to a higher standard deviation. Averaging of frame-based estimates does not seem to improve them.

Figure 4.14 illustrates similar results for the standard deviation of the autoregressive parameter estimates.

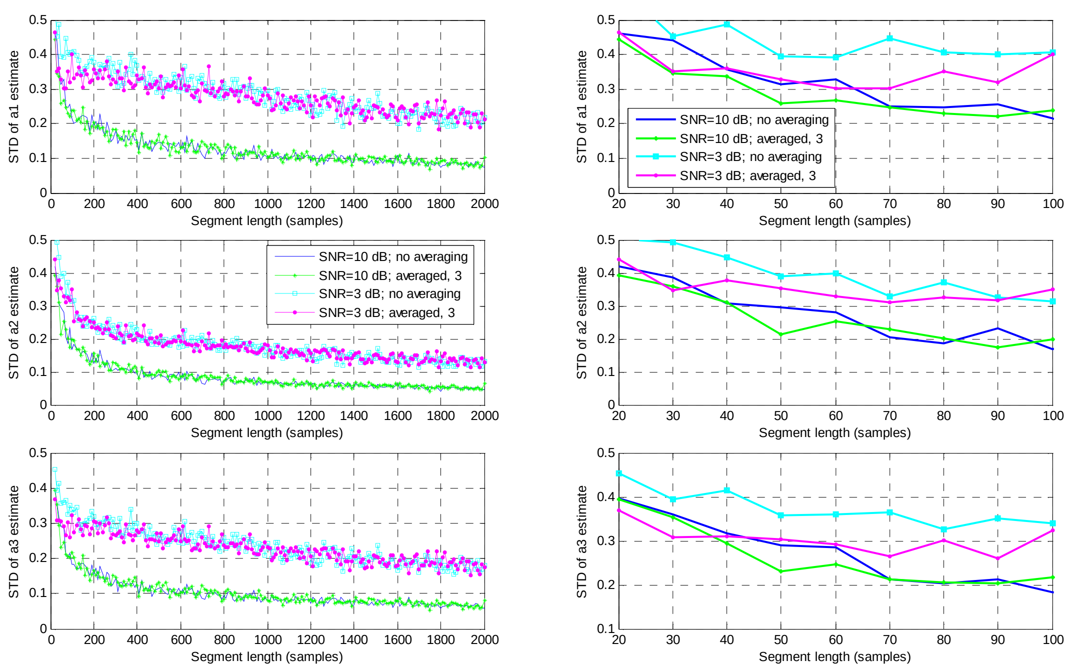

(a) (b)

Figure 4.14: Standard deviation of the autoregressive parameter estimates (a) and its magnified version (b).

It is seen in Figure 4.14 that averaging of the autoregressive parameters leads to a decrease in the standard deviation of these estimates when the frame length is small.

We conclude that averaging of parameter estimates may – especially in low SNR cases and when segment length is small – lead to improved estimates, i.e. decreased standard deviation. Since we are interested in the processing of short sequences with low SNR, it is worth implementing averaging of AR parameter estimates obtained for a number of overlapping frames of the modeled sequence.

4.3.2 Effect of signal enhancement

The same SNRs, namely 10 dB and 3 dB, were simulated. Signal enhancement by the matched filtering specified in (4.13) was implemented for one to ten iterations followed by AR(3) parameter estimation as described in Section 4.2. The powers of the driving and additive noise were estimated only once since the implemented enhancement technique decreases noise and therefore skews these estimates.

Figure 4.15 shows the average bias of the AR(3) parameter estimates when SNR = 3 dB. The results are plotted for a control case (no signal enhancement) and for 1, 2, 5, and 10 iterations of enhancement as indicated in the legend.

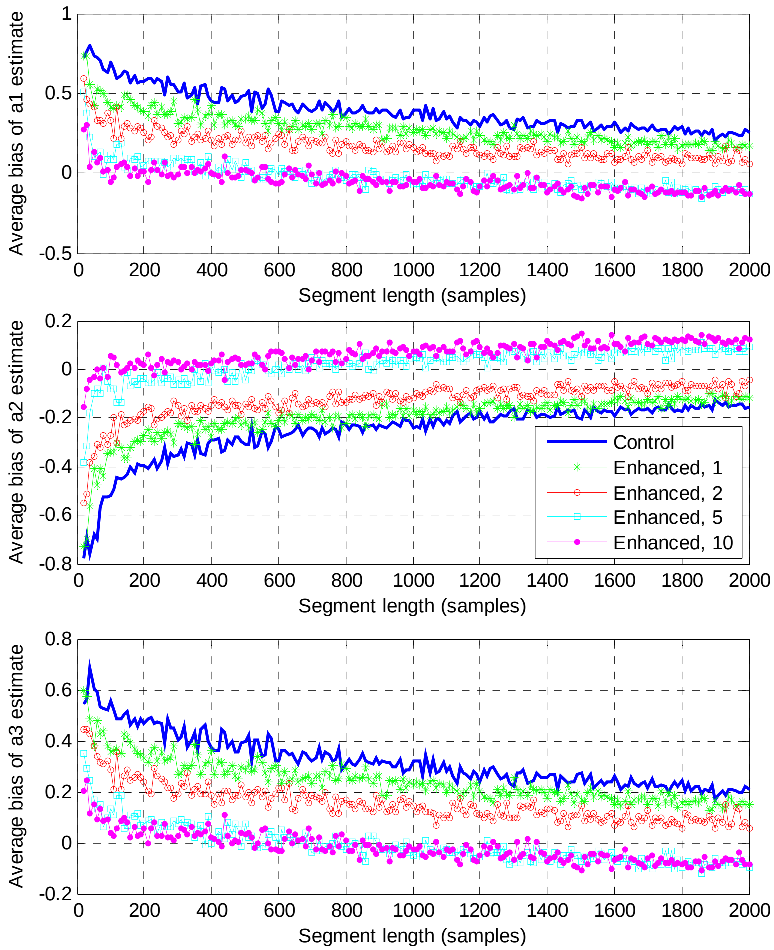

Figure 4.15: Average bias of AR(3) coefficient estimates, SNR = 3 dB.

As seen in Figure 4.15, the signal enhancement procedure, as described in Section 4.2, may – especially when short segments with low SNR are analyzed – lead to a decrease in the bias of the AR parameter estimates.

Figure 4.16 depicts the average bias of the AR(3) parameter estimates when SNR = 10 dB.

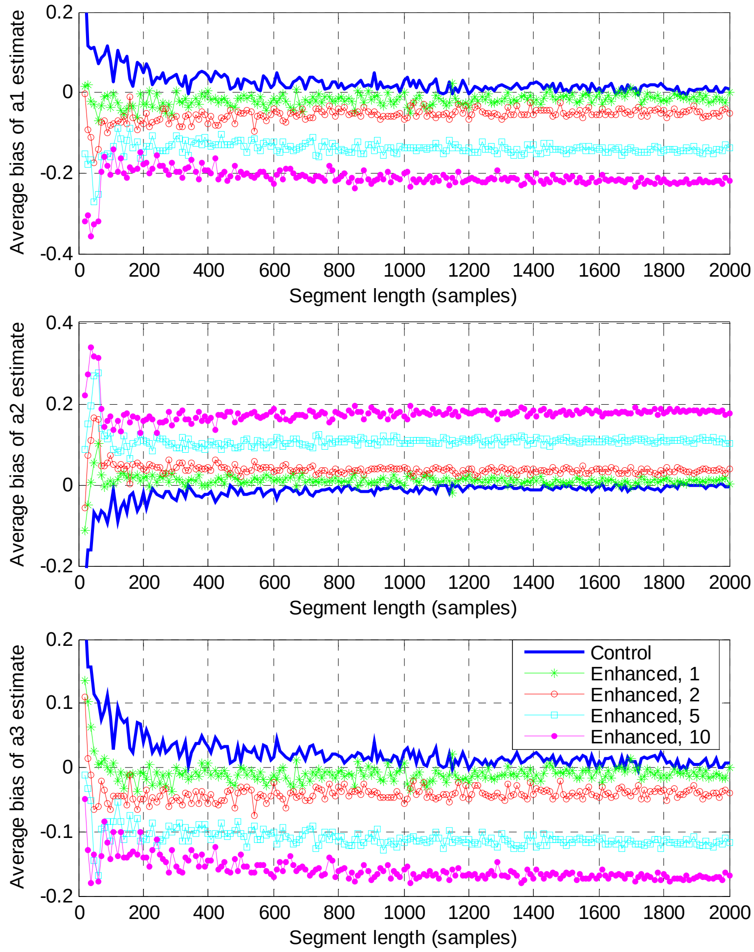

Figure 4.16: Average bias of AR(3) coefficient estimates, SNR = 10 dB.

We can conclude that in high SNR cases the matched filtering signal enhancement technique considered here may introduce additional bias as seen in Figure 4.16. For an SNR of 10 dB, the most desirable results are seen when only one iteration of the enhancement procedure is implemented.

Figure 4.17 illustrates the corresponding results for the standard deviation of the AR(3) parameter estimates.

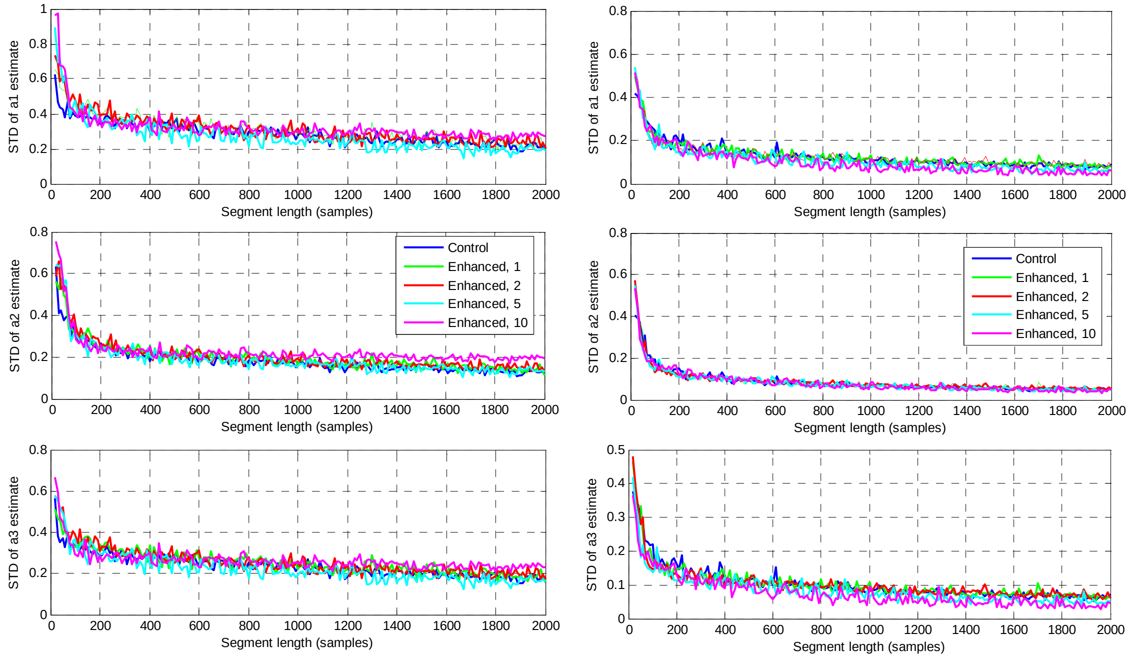

Figure 4.17: Standard deviation of AR(3) parameter estimates for (a) SNR = 3 dB and (b) SNR = 10 dB.

We see from Figure 4.17 that in high SNR cases the matched filtering signal enhancement procedure does not offer any improvement in terms of the standard deviation of the AR parameter estimates.

We conclude that the signal enhancement technique may improve the AR estimates by decreasing their average bias, when SNR is low and frame length is short.

4.3.3 MS coherence estimates

The MS coherence estimates were evaluated according to (4.4) based on the AR(3) parameter and noise power estimates as discussed in Section 4.2.

Figure 4.18 represents the true MS coherence and five independent estimates for a segment length N_w=100 and SNR = 10 dB (a) and SNR = 3 dB (b).

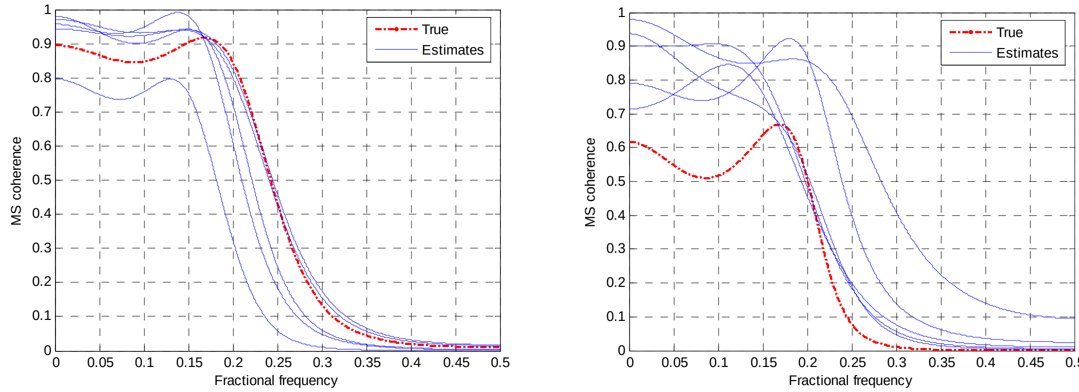

(a) (b)

Figure 4.18: True MS coherence and its estimates for N_w = 100, and SNR = 10 dB (a) and SNR = 3 dB (b).

It is seen in Figure 4.18 that the coherence estimates are more consistent with the true coherence when SNR is high. Next, we present MS coherence estimates for shorter segments, i.e. $N_w = 25$.

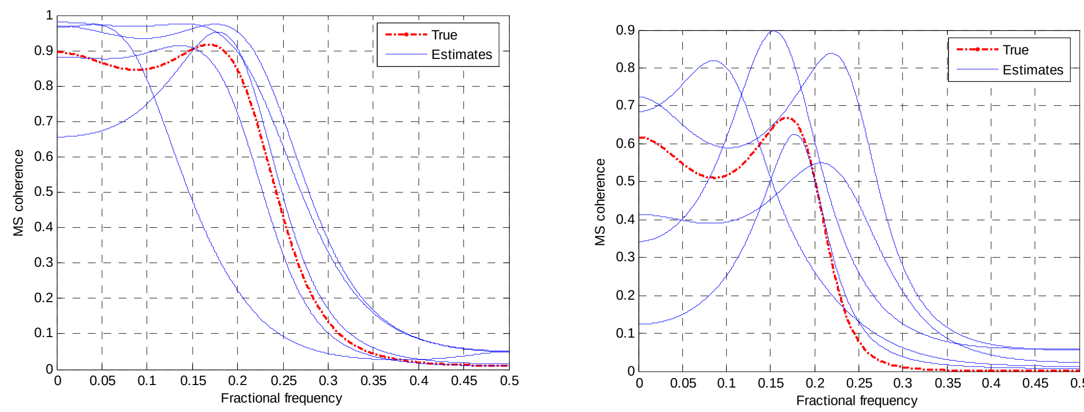

(a) (b)

Figure 4.19: True MS coherence and its estimates for N_w = 25, and SNR = 10 dB (a) and SNR = 3 dB (b).

Comparing Figures 4.18 and 4.19, we conclude that when short segments are analyzed and SNR is low, a higher discrepancy between the true MS coherence and its estimate results. This conclusion agrees with the previously seen result that short segments and low SNR contributed to a higher variance of the estimated noise powers and AR parameters.

The mean absolute error (MAE) computed according to (4.20) and the standard deviation of the MS coherence estimates are shown in Figure 4.20. For each segment length, the MS coherence was estimated for 100 independent segments. One iteration of signal enhancement is implemented together with averaging of the AR parameter estimates over 3 frames.

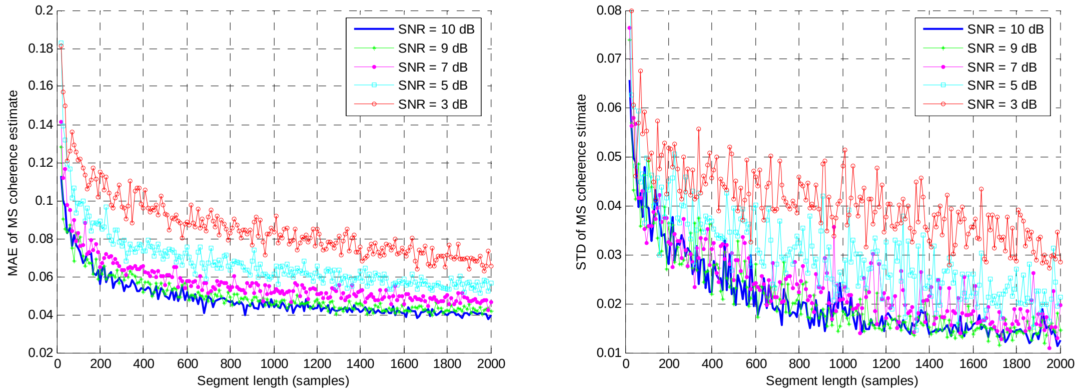

(a) (b)

Figure 4.20: MAE (a) and standard deviation (b) of MS coherence estimate.

We see in Figure 4.20 that both MAE and standard deviation of the MS coherence estimate decrease when the length of the analyzed frames increases. A lower SNR yields a higher bias and a higher standard deviation in the MS coherence estimates.

We also compare the MAE and the standard deviation of the MS coherence estimates obtained with and without the matched filtering signal enhancement. The corresponding results are illustrated in Figure 4.21.

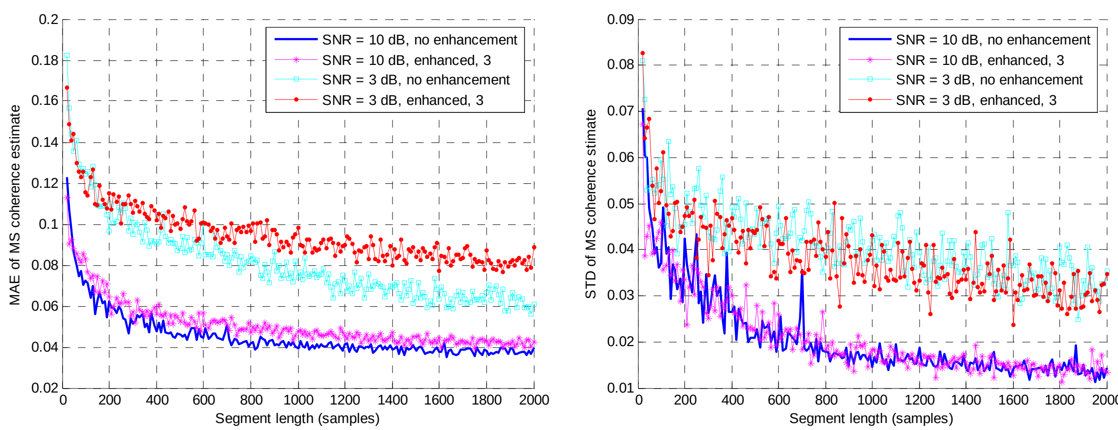

(a) (b)

Figure 4.21: Effect of signal enhancement on (a) MAE and (b) standard deviation of MS coherence estimate.

We see in Figure 4.21 (a) that signal enhancement leads to an increased bias in the coherence estimates for low SNR cases when segment length exceeds approximately 200. In the high SNR cases (SNR = 10 dB), the bias in the MS coherence estimate is higher while signal enhancement was implemented, when the segment length exceeds approximately 50 samples. It is seen in Figure 4.21 (b) that the signal enhancement does not affect the standard deviation of the MS coherence estimates in the high SNR case. In the low SNR case, the standard deviation exhibits a minor decrease when signal enhancement was implemented.

Since we are particularly interested in the processing of short segments, namely fewer than 50 samples, signal enhancement can be considered beneficial.

For illustrative purposes, we show in Figure 4.22 averaged MS coherence estimates based on 100 independent trials, for SNR of 10 dB and 3 dB. The corresponding true MS coherences are also shown.

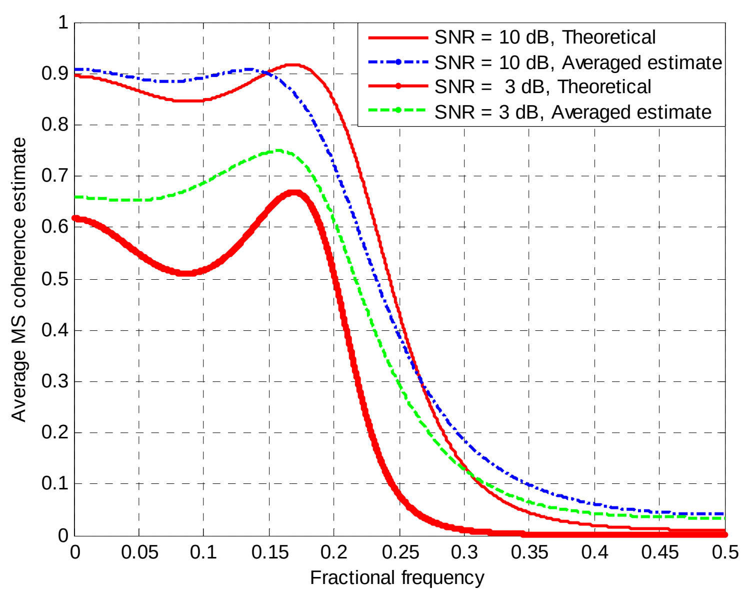

Figure 4.22: MS coherence estimate, averaged over 100 trials, and true MS coherence.

We see in Figure 4.22 that the MS coherence estimates are biased. This bias is more pronounced for low SNR. However, the general behavior of the estimates is consistent with the true coherence.

4.4 Application to EEG

In this section, the previously developed MS coherence estimator is tested on real EEG records from the "ADHD EEG data set" described in Section 3.4.1.

4.4.1 AR model order selection

When developing the model, we assumed its order p = 3 as suggested [10] by Palaniappan et al. In this subsection we verify that this assumption is reasonably valid by employing as order estimators the Akaike Information Criterion (AIC) and the Minimum Description Length (MDL) criterion [13], which are computed as follows:

$$\hat{p}_{AIC} = \arg\left\{\min_{k=[0,1\ldots P]}\left(\ln\hat{\sigma}_k{}^2 + \frac{2k}{N}\right)\right\} \tag{4.22}$$

$$\hat{p}_{MDL} = \arg\left\{\min_{k=[0,1\ldots P]}\left(\ln\hat{\sigma}_k{}^2 + \frac{k}{N}\ln N\right)\right\} \tag{4.23}$$

where $\hat{\sigma}_k{}^2$ is the maximum likelihood estimate of the driving noise variance for the AR(k) model, N is the length of the modeled sequence, and P represents the maximum allowed model order.

The AR parameters and the driving noise variance were estimated via the Yule-Walker method (Matlab function *aryule*). The values of AIC and MDL, evaluated as in (4.22) and (4.23) for a number of randomly selected EEG frames of length 25 samples, collected from randomly selected subjects, are presented in Figure 4.23.

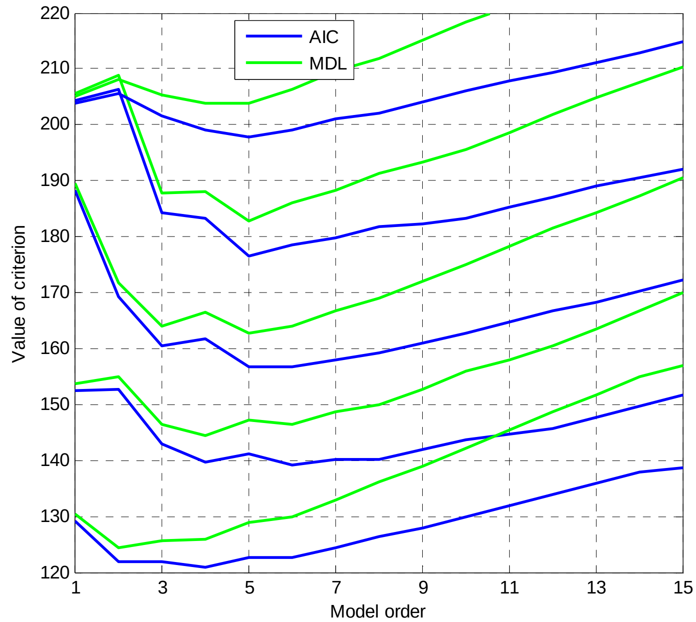

Figure 4.23: Values of the Akaike Information Criterion and the Minimum Description Length criterion evaluated for randomly selected 25 sample segments of EEG from randomly selected electrodes.

Figure 4.24 illustrates order estimates of AIC and MDL obtained for 100 randomly selected 25 sample EEG segments recorded from different individuals.

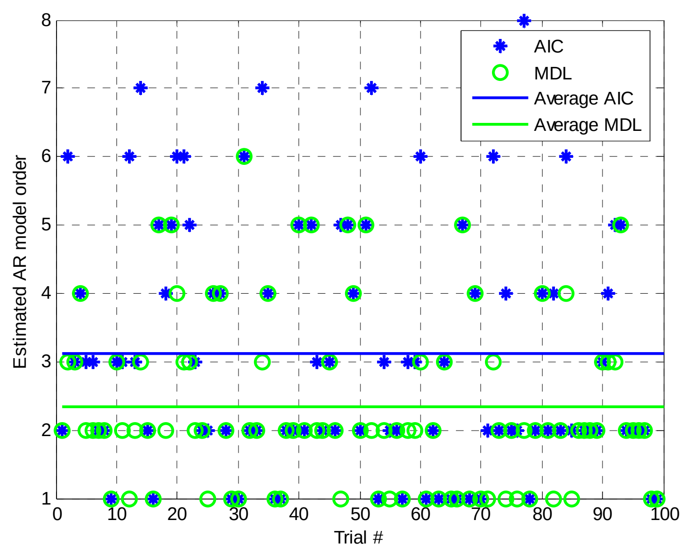

Figure 4.24: AR model order estimates for 100 randomly selected 25 sample segments of EEG via Akaike Information Criterion and Minimum Description Length criterion.

We see in Figure 4.24 that the AR order estimates according to the AIC and MDL criteria generally do not exceed 7. The average AIC and MDL order estimates are also shown in Figure 4.24.

Based on the estimation results presented in Figure 4.24 we conclude that EEG processes can be reasonably modeled as AR(3) processes.

4.4.2 Discrimination between ADHD and non-ADHD children

The EEG data used has been pre-filtered by a band-pass filter with a pass-band of 2 to 64 Hz as mentioned in Section 3.41. We observed that this operation caused the coherence estimate to be consistently low for frequencies higher than approximately 80 Hz and close to one for frequencies lower than approximately 40 Hz for all tested subjects (ADHD and non-ADHD) as shown in Figure 4.25. The MS coherence estimates were obtained for 25 sample segments of EEG with the model order p = 3 as discussed in Section 4.4.1.

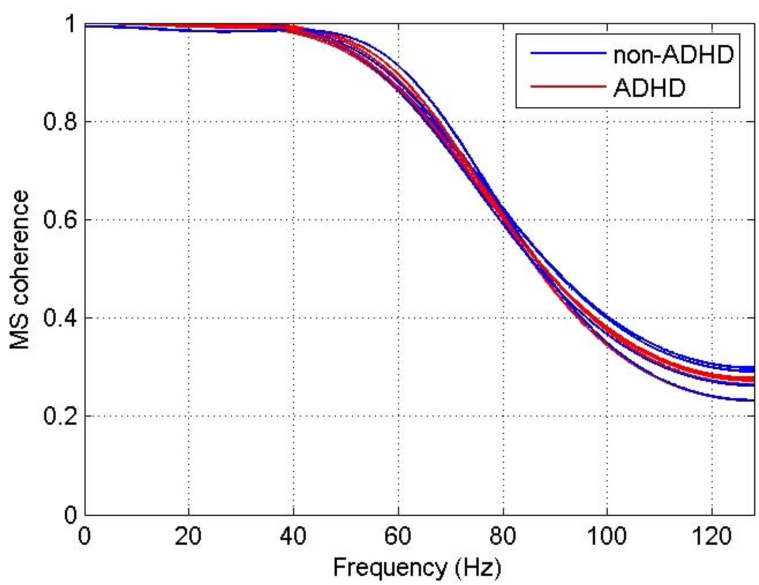

Figure 4.25: MS coherence estimates between the electrodes F_{p1}-F_3 for EEG sequences pre-filtered from 2 to 64 Hz, f_s = 256 Hz, N = 25.

We suggest that the effect seen in Figure 4.25 (i.e. MS coherence being low for high frequencies and high for low frequencies for all tested subjects) is due to the pre-filtering operation and, therefore, these results are non-informative. To eliminate non-informative results and to exclude the frequency content attenuated by the pre-filtering, the data can be re-sampled at a lower sampling frequency. Namely, to conduct processing for the frequency band from 0 to 64 Hz as considered here, we can use a new sampling frequency of 128 Hz.

To conduct analysis for the lower frequency band, an anti-aliasing low-pass filter with the frequency band of interest can be used followed by resampling of the EEG data. According to the results reported in Section 3.4.3, δ rhythm phase synchrony is different on average for ADD and non-ADHD participants. Based on this observation and on the report of Barabasz, Crawford, and Barabasz [14], suggesting different θ (i.e. 4 – 6 Hz) for ADHD and non-ADHD subjects, the EEG data was filtered using a Kaiser window-based FIR approximation to a low-pass filter with cut-off frequency f_c = 10 Hz, which exceeds the θ rhythm; a transition band of 2 Hz, and a stop-band attenuation of at least 50 dB. The length of the filter was N_f = 234; its frequency response is presented in Figure 4.26.

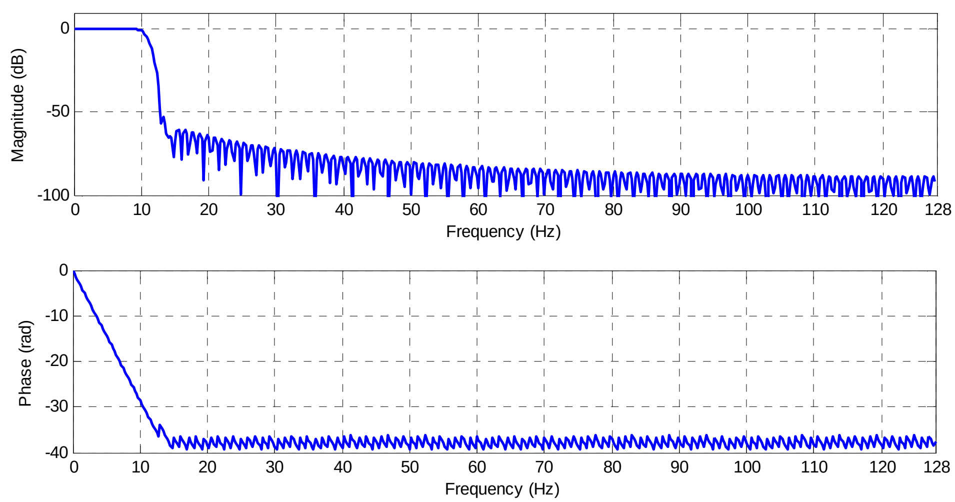

Figure 4.26: Magnitude and phase of frequency response of the Kaiser window-based FIR low-pass filter.

Time delays due to filtering were accounted for by discarding the first and last $\left\lfloor {}^{N_f}\!/_2 \right\rfloor$ time samples. After pre-filtering, the EEG data was resampled at the sampling frequency of $f_{s,new} = 2f_c$ = 20 Hz. EEG segments of length N = 20 samples (1 second) were processed. We note that processing of such long EEG segments generally violates the local stationarity conditions for the EEG.

The MS coherence was estimated for electrode pairs of interest and for a particular task (i.e. “Reading” or “Math” as described in Section 3.4.1) for each segment (time window) for all participants. To accomplish this and form EEG segments, the low-pass filtered EEG data was first resampled to the new sampling frequency $f_{s,new}$ and then windowed by a rectangular window of length N.

The time window was shifted by one sample and MS coherence was estimated again. Thus, MS coherence was estimated over time as illustrated in Figure 4.27.

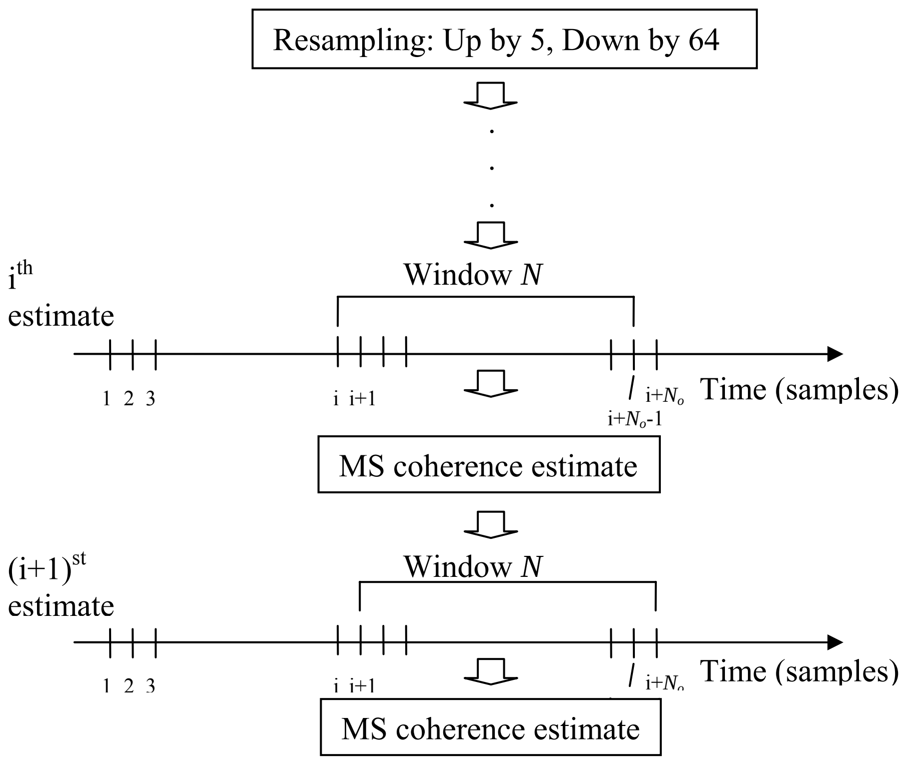

Figure 4.27: Resampling/windowing algorithm.

Before conducting the experiment aimed at distinguishing between individuals with ADHD and non-ADHD subjects, we verified the previously used assumption regarding the SNR of the EEG being between 3 and 10 dB [11], [12]. SNR was evaluated based on (4.19) as follows:

$$SNR = 10\log_{10}\left(\frac{\hat{\sigma}_w^2}{\hat{\sigma}_v^2\left(1 - p_{\hat{a},1}p_{\hat{a},2}\right)}\right) \tag{4.24}$$

where $\hat{\sigma}_w^2$ and $\hat{\sigma}_v^2$ are power estimates for the driving and additive noises, and $p_{\hat{a},1}$ and $p_{\hat{a},2}$ represent the two complex conjugate roots of the AR estimates of the **a** polynomial.

The SNR estimates obtained for a number of randomly selected 20 sample EEG segments collected from randomly chosen subjects, low-pass filtered at 10 Hz and re-sampled at 20 Hz, are presented in Figure 4.28.

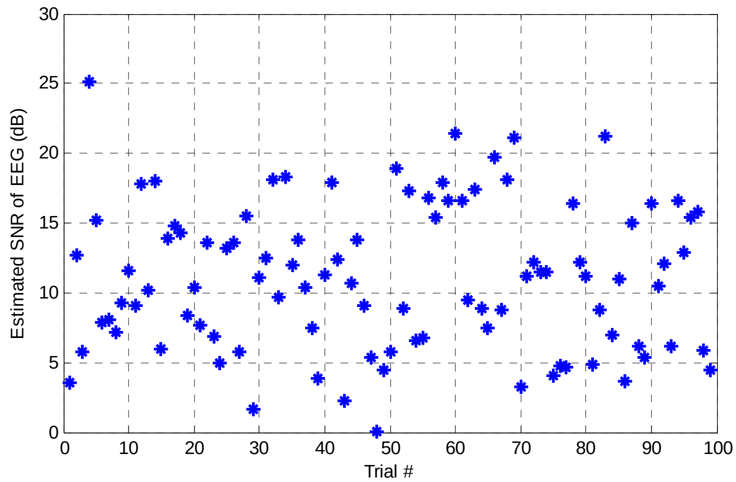

Figure 4.28: SNR estimates of EEG, $N = 20$, $f_s = 20$ Hz.

We see in Figure 4.28 that the EEG SNR estimates vary over a wide range. The average SNR (i.e. power estimates averaged and then converted to dB) for the estimates presented in Figure 4.28 was 11.1 dB. Based on this result and the findings in Section 4.3.2, one iteration of matched filtering signal enhancement is used for the processing of the EEG data.

For the discrimination experiment, the subjects were arbitrarily divided into six pairs; each pair contained one non-ADHD and one ADHD participant. The MS coherence estimates were compared for the non-ADHD and the ADHD individual within each pair. Examples of the MS coherence estimates between electrodes F_{p1} and F_3, obtained at randomly chosen times for two pairs of participants for the "Math" task, are shown in Figure 4.29.

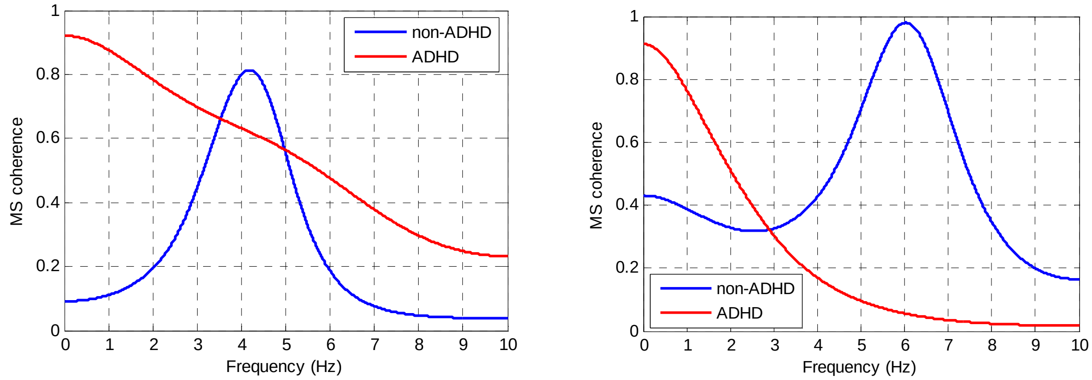

Figure 4.29: Examples of estimated MS coherence between electrodes F_{p1}-F_3 for two pairs of non-ADHD and ADHD individuals as observed over 1 sec.

We see in Figure 4.29 that – for two participant pairs shown – MS coherence is considerably higher at very low frequencies (i.e. below 1 Hz) for the ADHD subject than for the non-ADHD individual. We also see that the θ rhythm MS coherence (approximately 4 – 6 Hz) is higher (more specifically, it forms a peak) for a non-ADHD subject than for an ADHD individual.

MS coherence estimates for both non-ADHD and ADHD participants were observed over time and found to be changing significantly over time and between subjects. However, the general trends depicted in Figure 4.29 were consistent over time as Figure 4.30 illustrates. MS coherence was estimated for all participants for shifted in time 20 sample-long (1 second) windows. The value of coherence is represented by the color bar.

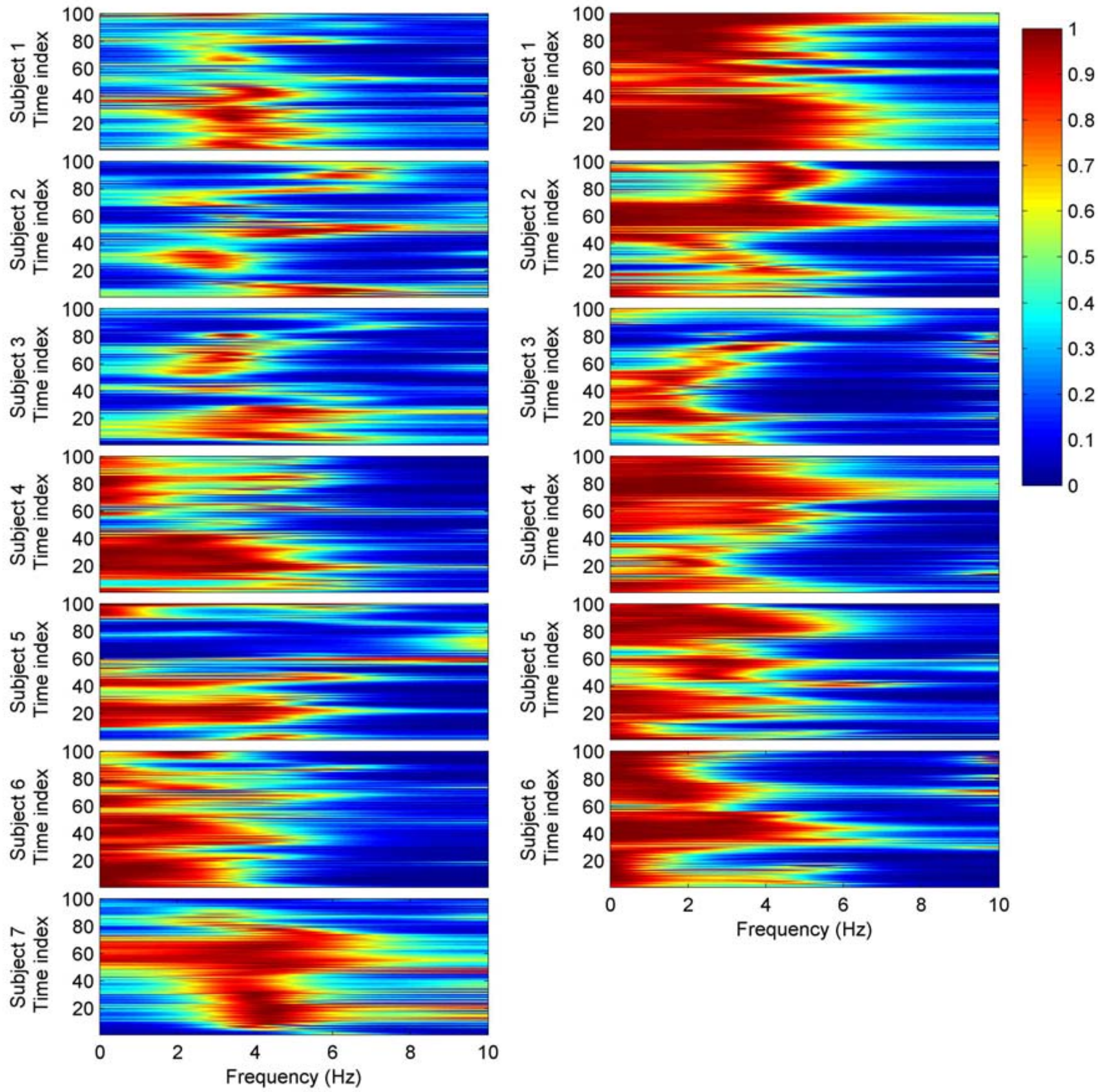

(a) (b)

Figure 4.30: MS coherence estimated over time and (a) for all non-ADHD participants, (b) for ADHD subjects as observed over 1 sec intervals.

As Figure 4.30 indicates, the previously observed differences between coherence of non-ADHD and ADHD participants – MS coherence being considerably higher at very low frequencies (i.e. below 1 Hz) for the ADHD subject than for the non-ADHD individual and the θ rhythm MS coherence (approximately 4 - 6 Hz) being higher (more specifically, it forms a peak) for a non-ADHD subject than for an ADHD individual – can be clearly seen on four out of seven non-ADHD participants and on all ADHD subjects.

Comparing the results presented in Figure 4.30 with the phase synchrony-based classification discussed in Section 3.4.3, we note that one of the three non-ADHD subjects, whose coherence estimate is inconsistent with the rest of the non-ADHD group, "Subject 5", was excluded from the phase synchrony processing as discussed in Section 3.4.3. Two other subjects, "Subject 4" and "Subject 6", exhibit low percentages of correct classification in the δ rhythm as depicted in Figure 3.37 (a).

Higher rhythms were also tested but no obvious differences between MS coherence of non-ADHD and ADHD individuals were found.

We point out two major observations.

1. MS coherence is generally higher for non-ADHD individuals than for ADHD participants when computed for the EEG collected from the frontal lobe for θ *rhythm* (approximately 4 – 7 Hz). This observation is consistent with the report of Barabasz, Crawford, and Barabasz [14], who reported "more desynchronized" low θ (i.e. 4 – 6 Hz) in ADHD.
2. MS coherence is consistently higher for ADHD subjects than for non-ADHD individuals when computed for the EEG collected from the frontal lobe for very low frequencies (i.e. below 1 Hz).

These effects are more pronounced when MS coherence is computed for the frontal lobe. No significant difference was observed between right and left hemispheres. Also, the observed differences between the MS coherences of non-ADHD and ADHD individuals are more pronounced for the "Math" task then for the "Reading" task. It is important to observe MS coherence as computed repeatedly for a series of overlapping time intervals (windows) since MS coherence is changing over time.

Our observation of MS coherence being different in δ rhythm between non-ADHD and ADHD participants is in agreement with the results reported in Section 3.4.3, where δ rhythm phase synchrony was found to be different between non-ADHD and ADHD individuals.

However, we emphasize that MS coherence and phase synchrony are two completely different measures. While MS coherence is based on the signal power in a particular frequency band, phase synchrony indicates whether two sequences are at the same frequency. In other words, high phase synchrony in the specific frequency band does not imply high MS coherence in the same band and vice versa.

4.5 References

[1] M. H. Hayes, *Statistical digital signal processing and modeling*, John Wiley & Sons, Inc., 1996.

[2] B. Schack and W. Krause, "Dynamic power and coherence analysis of ultra short-term cognitive processes – a methodical study," *Brain topography*, vol. 8, #2, 1995, pp. 127-136.

[3] P. B. Colditz, C. J. Burke, and P. Celka, "Digital processing of EEG signals," *IEEE Engineering in Medicine and Biology*, September/October 2001, pp. 21-22.

[4] S. M. Kay, *Modern Spectral Estimation. Theory and Application*, Prentice-Hall Signal Processing Series, 1988.

[5] J. S. Lim and A. V. Oppenheim, "All-pole modeling of degraded speech," *IEEE Transactions on Acoustics, Speech, and Signal Processing*, vol. ASSP-26, #3, June 1978, pp. 197-210.

[6] J. S. Lim and A. V. Oppenheim, "Enhancement and bandwidth compression of noisy speech," *Proceedings of the IEEE*, vol. 67, #12, December 1979, pp. 1586-1604.

[7] E. Parzen, "An approach to time series analysis," *The Annals of Mathematical Statistics,* vol. 32, #4, December 1961, pp. 951-989.

[8] M. R. Sambur, " A preprocessing filter for enhancing LPC analysis /synthesis of noisy speech," Acoustics, Speech, and Signal Processing, IEEE International Conference on ICASSP '79, vol. #4, April 1979, pp. 971-974.

[9] A. A. (Louis) Beex and M. A. Rahman, "On averaging Burg spectral estimators for segments," *IEEE Transactions on Acoustics, Speech and Signal Processing*, vol. ASSP-34, #6, December 1986, pp. 1473-1484.

[10] R. Palaniappan, P. Raveevdran, S. Nishida, and N. Saiwaki, "Autoregressive spectral analysis and model order selection criteria for EEG signals," *2000 Tencon Proceedings: Intelligent Systems and Technologies for the New Millennium,* Malaysia, Vol. II, September 2000, pp. II-126 – II-129.

[11] A. Schlögl, M. Slater, G. Pfurtscheller, “Presence research and EEG,” *Proceedings of International Conference,* Oct. 2002, Portugal.

[12] P. beim Graben, “Estimating and improving the signal-to-noise ratio of time series by symbolic dynamics,” *Physical Review E,* vol. 64, Oct. 2001, pp. 051104-1 – 051104-15.

[13] P. M. Djuric and S. M. Kay, “Order selection of autoregressive models,” *IEEE Transactions on Signal Processing*, vol. 40, # 22, Nov. 1992, pp. 2829-2833.

[14] A. Barabasz, H. Crawford, and M. Barabasz, “EEG topographic map differences in attention deficit disordered and non-ADHD children: Moderating effects from focused active alert instructions during reading, math and listening tasks,” *Presented at the 33rd Annual Meeting of the Society for Psychophysiological Research*, Rottach-Egem, Germany, October, 27-31, 1993.

Chapter 5

Conclusions and Future Research

A Phase Synchrony Processor (PSP) is proposed and the influence of its parameters on the reliability of phase synchrony estimates is explored on the basis of known signals. Our study shows that to decrease bias in phase synchrony estimates, the processor parameters need to be selected judiciously. Namely, the bias in phase synchrony estimates can be minimized by applying long analysis windows or frames and by the use of wide-band filtering.

The value of the phase synchrony (coefficient), as evaluated by the PSP, is also affected by the difference in frequency of the two input signals. The phase synchrony value is robust to additive Gaussian noise, and the frequency difference in the PSP input components can be characterized by the absolute value of the periodic (Dirichlet) sinc function.

Application of phase synchrony processing to EEG suggests that it is possible to distinguish between children with and without attention deficit disorder on the basis of phase synchrony computed from the EEG recorded while performing attention intensive tasks. For many electrode pairs, δ rhythm and γ_1 rhythm phase synchronies were observed to be higher on average for non-ADHD subjects than for ADHD subjects. Euclidean distance-based classification, performed on phase synchrony, may help – with a careful choice of rhythm, task, and appropriate selection of electrode pairs to be processed – in assigning a subject accurately to a non-ADHD or ADHD group. Using phase synchrony-based Euclidean classification in the δ and γ_1 rhythms to decide between ADHD and non-ADHD subjects, an average of 66.3 percent of correct classification was found.

On average, γ_1 rhythm phase synchrony differs between high schizotypy smokers and high schizotypy nonsmokers, between high and low schizotypy individuals, and between the experimental conditions of eyes open and eyes closed. Euclidean distance-based classifiers yield 78 percent correct classification in discriminating between the eyes open and eyes closed conditions.

A new coherence estimator is developed, for the specific aim of analyzing short frames degraded by Gaussian noise. This parametric coherence estimator is targeted for processing locally stationary EEG segments. We confirmed the plausibility that short EEG segments can be modeled as AR(3) processes. We also found that – for the EEG data used – SNR is approximately 11-12 dB.

Application of the parametric coherence estimator to EEG records suggests that MS coherence is generally higher for non-ADHD individuals than for ADHD participants when evaluated for the θ rhythm of EEG. Also, MS coherence is consistently higher for ADHD subjects than for non-ADHD individuals when computed for the lower end of the δ rhythm (i.e. below 1 Hz). These effects are more pronounced when MS coherence is computed between EEG records acquired from the frontal lobe and for participants performing attention intensive tasks (i.e. "Reading" or "Math"). By visual inspection, four out of seven non-ADHD subjects and all six ADHD participants can readily be assigned to the correct group.

The above observations suggest that coherence and phase synchrony can serve as important concepts in neuro-studies. Application of phase synchrony processing and parametric MS coherence estimation for the analysis of EEG for individuals diagnosed with various disorders such as epilepsy, seizures, schizophrenia, and sleep disorders could be worthwhile. An interesting open issue is whether coherence and phase synchrony can be used to evaluate the extent and/or existence of head injuries, tumors, infections, degenerative diseases, and metabolic disturbances that affect the brain. It remains an open issue as to whether automatic classification between non-ADHD and ADHD individuals based on MS coherence estimated from EEG can be done with high accuracy. While our initial results in this direction are encouraging, it would require a much larger database to build a better classifier. A successful classifier would be useful for a quick preliminary – and inexpensive, relative to interviews and MRI – diagnosis of attention disorders.

Appendix A

Frequency bands corresponding to EEG rhythms

EEG rhythm	**Frequency band (Hz)**
δ (delta)	0 – 4
θ (theta)	4 – 7
α or μ (alpha or mu)	8 – 12
β_1 (beta one)	13 – 20
β_2 (beta two)	20 – 30
γ_1 (gamma one)	30 – 40
γ_2 (gamma two)	40 – 50
σ (sigma – sleep spindle)	12 – 14

Vita

Gleb V. Tcheslavski received his Bachelor of Science and Master of Science degrees in Electronic Engineering in June 1997 from Bauman Moscow State Technical University in Moscow, Russia. After his graduation, he worked as a Research Scientist and Teaching Assistant at Bauman Moscow State Technical University and as Head of the Information Division at the State Reserve Committee in Russia. In January 2001 he entered Virginia Tech to pursue the PhD degree in Electrical Engineering. His research interests are in the areas of Digital Signal Processing, Biomedical Signal Processing, Image Processing, and Radar Applications.